MEDNARODNA PODIPLOMSKA ŠOLA JOŽEFA STEFANA
JOŽEF STEFAN INTERNATIONAL POSTGRADUATE SCHOOL

ASWATHY VASUDEVAN

ATMOSPHERIC PRESSURE PLASMA JET DEPOSITION OF NANOPARTICLES AND ITS APPLICATIONS

DOCTORAL DISSERTATION

LJUBLJANA, AUGUST 2022

ATMOSPHERIC PRESSURE PLASMA JET DEPOSITION OF NANOPARTICLES AND ITS APPLICATIONS

Aswathy Vasudevan

Doctoral Dissertation
Jožef Stefan International Postgraduate School
Ljubljana, Slovenia

Supervisor: Prof. Dr. Aleksander Zidanšek**,** Jožef Stefan International Postgraduate School and Jožef Stefan Institute, Ljubljana, Slovenia
Co-Supervisor: Prof. Dr. Uroš Cvelbar, Jožef Stefan International Postgraduate School and Jožef Stefan Institute, Ljubljana, Slovenia

Evaluation Board:
Prof.Dr. Slavko Bernik, Chair, IPS and Jožef Stefan Institute, Ljubljana (Head of the Commission)
Prof. Dr. Eva Kovačević, Member, Université d'Orléans, France
Dr. Anton Nikiforov, Member, Gent University, Belgium

MEDNARODNA PODIPLOMSKA ŠOLA JOŽEFA STEFANA
JOŽEF STEFAN INTERNATIONAL POSTGRADUATE SCHOOL

Aswathy Vasudevan

ATMOSPHERIC PRESSURE PLASMA JET DEPOSITION OF NANOPARTICLES AND ITS APPLICATIONS

Doctoral Dissertation

NANOS NANODELCEV S PLAZEMSKIM CURKOM PRI ATMOSFERSKEM TLAKU IN NJEGOVA UPOROBA

Doktorska disertacija

Supervisor: Prof. Dr. Aleksander Zidanšek

Co-Supervisor: Prof. Dr. Uroš Cvelbar

Ljubljana, Slovenia, August 2022

In loving memory of my Dad

&

To my family and friends

Acknowledgments

First, I would like to thank Prof. Dr. Aleksander Zidanšek and Prof. Dr. Uroš Cvelbar for giving me an opportunity to accomplish my PhD at Jožef Stefan Institute. I am so grateful for their constant support and guidance during the past 5 years. Most of all, their inspiring and friendly attitude and suggestions made me to pursue the PhD journey, which was tough for me. I honestly appreciate the effort and kind nature towards me while I was struggling to move forward. I would also like to thank Prof. Dr. Sabu Thomas (Vice-Chancellor, Mahatma Gandhi University, India) for introducing me to the research endeavors. Secondly, I want to thank my F6 colleagues, Andrea, Neelakandan, Petra and Martin for being supportive all the time during PhD. I want to thank Dr. Gregor Filipič, especially for the huge support and suggestions regarding work and science since day one at F6, and Dr. Vasyl Shvalya for his assistance during my PhD. I would like to thank Dr. Janez Zavašnik for his kind heart and generous behaviour for someone needing help and for his unforgettable stories during the coffee breaks and all. I must thank Urška Kisovec for all the nice things she has done as department staff and as a kindhearted individual. I am grateful to have everyone else; Jaka Olenik, Damjan Vengust, Marko Žumer, Martina Modic, Nataša Hojnik, Vicenc Nemanič, as my colleagues in F6 department. I would also like to express my gratitude to everyone I have met during this period and grateful to the opportunity to work with them and learn new things day by day.

I would like to express my sincere gratitude to the Jožef Stefan International Postgraduate School and Department of Gaseous Electronics, Jožef Stefan Institute. I am also thankful for the scholarship provided by AD FUTURA (Public Scholarship, Development, Disability and Maintenance Fund of the Republic of Slovenia). In addition, I also acknowledge PEGASUS (Plasma Enabled and Graphene Allowed Synthesis of Unique Nano-structures), funded by the European Union's Horizon research and innovation program for the financial support.

I have to say a big thanks to my best friend Snehamol Mathew, for being there for me in all the situations; good and bad; well, that is what friends are for. However, she helped me a lot to go through the hardest times in my life. It is the best thing to have someone who understands all the difficulties of work as of life. My family; my mother Prasanna, sister Dhanya, brother in law Satheesh and their kids (Mukundakrishnan, Subhadra and Bhavasundar); they were there for me in all difficulties, cheering me up. Moreover, my father, Vasudevan, who left us in January 2021, the one who was more excited to see me, graduating with a doctorate. Finally, I owe special gratitude to my parents-in-law and

parents for their love, continuous and unconditional support during my long stay abroad. Most importantly, I would like express appreciation to my husband Sharon for his support, encouragement, patience and unwavering love.

Abstract

Atmospheric pressure non-equilibrium plasma jets in material processing have received substantial attention in the past two decades and are still in the developing stage with a growing interest in material synthesis and surface processing. The main opportunities of these techniques are their potential cost reductions in apparatus and handling. Because of their distinctive operations, atmospheric pressure plasma jets (APPJ) are easier to handle and maintain. In addition to these advantages, plasma jets provide exclusive nanomaterial synthesis and processing possibilities, placing the substrate outside the boundaries. Subsequently, the integration into existing production lines of nanomaterials is expected to be much easier. However, great exertions are needed to optimize the process since many factors can affect it. For example, the chemical species and atmospheric conditions can affect the propagation of the plasma stream originating from the device to the open space and towards the substrate.

This work aims to fabricate a fast and reliable synthesis method for high on-demand nanoparticles, specifically plasmonically active nanoparticles for sensing applications. This work would contribute to the solution of complications in existing synthesis procedures like toxic chemical procedures used for gold nanoparticle synthesis. Atmospheric pressure plasma-driven reduction does not need any reducing agents or surfactants, with which the purification of the product would be an extra step. It could also be a promising technique for a fast, reliable, and cost-effective preparation of metal nanoparticles. It can be directly used for biological applications since the procedure is entirely non-toxic. The atmospheric pressure plasma jets can reduce the metal salts instantaneously, and thereby synthesis and depositions of metal nanoparticles happen in a single step, wherein the conventional non-toxic biological procedure would take hours or even days to complete the synthesis. In the application part, work is focused on the easy and economical synthesis of plasmonically active nanoparticles, which could be used for sensing applications in bio-nanotechnology. To achieve the set goals, this research was focused mainly on noble metal nanoparticle synthesis, such as gold, which is widely used in different fields of applications. Before that, an appropriate plasma system was successfully built with a single electrode APPJ which allows plasma-vapor interactions that lead to the reduction of the metal salts.

However, quantitative assessment of the synthesis process by plasma-vapor interactions is complex. The results support the proposed hypothesis that the atmospheric pressure plasma jet mediates the reduction of water-soluble salts of the noble metals via plasma-vapor interactions and can replace conventional, time-consuming synthesis techniques. So synthesized nanoparticles are plasmonically active and can be used for advanced electronics or sensing applications, including bacterial DNA detection applications.

The main aim of this work is to utilize plasma jets for the reduction and deposition of metal nanoparticles, thus simplifying the complex steps in existing conventional methods.

Povzetek

Neravnovesni plazemski curki pri atmosferskem tlaku pri obdelavi materialov so bili v zadnjih dveh desetletjih deležni precejšnje pozornosti in so še vedno v fazi razvoja ter naraščajočega zanimanja za sintezo materialov in obdelavo površin. Glavna priložnost teh tehnik je potencialno znižanje stroškov opreme in procesov. Plazemski curki pod atmosferskim tlakom (APPJ) so zaradi posebnega delovanja lažji za rokovanje in vzdrževanje. Poleg teh prednosti nudijo plazemski curki ekskluzivne možnosti pri sintezi in obdelavi nanomaterialov, pri čemer substrat postavljajo izven meja. Pričakuje se, da bo integracija v obstoječe proizvodne linije nanomaterialov veliko lažja. Za optimizacijo procesa so potrebni veliki napori, saj lahko nanj vpliva veliko dejavnikov. Na primer, kemične substance in atmosferski pogoji lahko vplivajo na širjenje toka plazme iz naprave v odprt prostor in proti substratu.

Namen dela je razviti metodo za hitro in zanesljivo sintezo nanodelcev, po katerih je veliko povpraševanje, posebej za plazmonično aktivne nanodelce za senzorske aplikacije. To delo bi prispevalo k rešitvi zapletov v obstoječih postopkih sinteze, kot so toksični kemični postopki, ki se uporabljajo za sintezo zlatih nanodelcev. Redukcija s plazmo pri atmosferskem tlaku ne potrebuje redukcijskih sredstev ali površinsko aktivnih snovi, s katerimi bi bilo čiščenje produkta dodaten korak. To je tudi obetajoča tehnika za hitro, zanesljivo in stroškovno učinkovito pripravo kovinskih nanodelcev. Drugo dejstvo je, da se lahko neposredno uporablja za biološke aplikacije, saj je postopek popolnoma nestrupen. Plazemski curki pod atmosferskim tlakom lahko v trenutku reducirajo kovinske soli in tako pride do sinteze in odlaganja kovinskih nanodelcev v enem samem koraku, pri čemer bi konvencionalni nestrupeni biološki postopek trajal ure ali celo dneve za dokončanje sinteze. V aplikativnem delu je delo osredotočeno na enostavno in ekonomično sintezo plazmonično aktivnih nanodelcev, ki bi jih lahko uporabili za senzorske aplikacije v bionanotehnologiji. Da bi dosegli zastavljene cilje, so bile te raziskave osredotočene predvsem na sintezo nanodelcev plemenitih kovin, kot je zlato, ki je zelo razširjeno na različnih področjih uporabe. Pred tem je bil uspešno zgrajen ustrezen plazemski sistem z enoelektrodnim curkom plazme z atmosferskim tlakom, ki omogoča interakcije med plazmo in paro, kar vodi do redukcije kovinskih soli.

Vendar pa je kvantitativna ocena procesa sinteze z interakcijami med plazmo in paro težka. Rezultati podpirajo predlagano hipotezo, da plazemski curek pri atmosferskem tlaku posreduje pri redukciji vodotopnih soli plemenitih kovin prek interakcij med plazmo in paro ter lahko nadomesti običajne, dolgotrajne tehnike sinteze. Tako sintetizirani nanodelci so plazmonično aktivni in se lahko uporabljajo za napredne elektronske aplikacije ali zaznavanja v aplikacijah za odkrivanje bakterijske DNK.

Najpomembnejši cilj tega dela je uporaba plazemskih curkov za redukcijo in nanašanje kovinskih nanodelcev, kar olajša zapletene korake pri sedanjih običajnih metodah.

Contents

List of Figures

Abbreviations

AC	...	Alternating Current
APPJ	...	Atmospheric Pressure Plasma Jet
BID	...	Barrier Ionization Discharge
DBD	...	Dielectric Barrier Discharges
DC	...	Direct Current
DEA	...	Dissociative Electron Attachment
DNA	...	Deoxyribonucleic Acid
EDS	...	Energy-Dispersive X-ray Spectroscopy
PCA	...	Principal Component Analysis
RF	...	Radio Frequency
SEM	...	Scanning Electron Microscopy
SERS	...	Surface-Enhanced Raman Spectroscopy
TEM	...	Transmission Electron Microscopy
TMO	...	Transition Metal Oxides

xx

Chapter 1

An introduction to atmospheric pressure plasma jets in nanomaterial fabrication

1.1 Introduction

The advancement of atmospheric pressure plasma technologies has significantly increased in the past few years, focusing on their wide range of applications in material processing and synthesis, medicine and fuel reforming, etc. The possibility of non-equilibrium reactions occurring in atmospheric pressure plasmas encouraged interest in the advancement of nanomaterial processing. These advancements using atmospheric pressure plasmas are low-cost and easy to implement compared to other plasma processes like low-pressure plasmas. Low-pressure plasmas necessitate high-cost reactor maintenance, whereas the atmospheric pressure reactions are cheaper and easier to implement in an industrial environment and in laboratory use [1]. Especially for nanomaterial synthesis and modification, atmospheric pressure plasmas can offer precision synthesis and enhanced functional modifications [2][3]. Because of their small size, atmospheric pressure plasmas are also capable of locally etching and sputtering substrates and films and are also able to create microscale patterns [4][5][6]. Plasma jets and their manipulations, like micro jets and micro sprays have also proved their ability to deposit thin films and coatings [7][8][9][10].

The salient trait of atmospheric pressure and other microplasmas is the presence of significant populations of high-energy electrons having energies like 10 eV or higher. These electrons initiate and participate in the non-thermal dissociation of molecular entities in gases and vapors to produce high concentrations of reactive radical species [11]. The electron-induced dissociations can be employed as an alternative to various chemical reactions directing material synthesis from gas or vapor precursors, particularly for the synthesis of nanoscale materials. Because of the limitations of the current conventional top-down methods, nanomaterials are recommended to be prepared from the bottom-up by dissociating the molecular precursors and nucleation of the atomic constituents. Plasma-induced processes have also been serving as an alternative to wet chemical methods, which

are well known for bottom-up nanomaterial synthesis. Plasma methods were characterized for compatibility and high purity. Their non-specific chemistry paves the possibility of synthesizing a wide range of nanomaterials, including noble metals, transition metals, and metal oxides, group II–VI, III-V and IV semiconductors, and insulators such as polymers. In addition, low-temperature non-equilibrium plasmas create an exceptional environment for nanomaterial synthesis as the plasma limits the agglomeration, which enables the formation of crystalline materials, and the assembly and functionalization of materials. In comparison with low-pressure plasmas, the advantages of atmospheric pressure plasma synthesis are:

a) Intense chemistry: the mechanism of nucleation and growth in plasma involves gas phase collisions between radicals. These collisions are drastically increased at high pressures, creating highly favorable conditions for particle formation. Plasmas operating at atmospheric pressures contain a high density of radical particle nucleation from radical polymerization, which is very efficient compared to low-pressure plasma pathways.

b) Residence time and continuous flow: Nanoparticle synthesis in batch-type processes, like low-pressure plasmas, because of the long residence times, particles nucleate, grow, and eventually agglomerate. In plasma jets, vapor precursors flow into the plasma volume, followed by nucleation and quenching of the growth and rapid flow-out of the reactor volume. The residence time can be varied to tune the particle size with minimal agglomeration.

c) Plasma reactor geometry: A significant concern in nanoparticle growth is controlling the residence time distribution (RTD). Since the residence time will have a characteristic distribution, it will mostly end up in non-uniform particle nucleation and growth. To control the RTD, we need to reduce the reactor volume; like in microscale reactors, which have short residence times in a range of milli- to microseconds, they can produce uniform nanomaterials since the temperature and concentration variations are minimized and the residence time is narrowed. Apart from this microreactor, geometries are considered to reduce precursor consumption and lower the safety risks.

d) Self-assembly: Nanoparticles can acquire charge and interact with each other with Coulombic and van der Waals forces in the plasma environment to form self-organized structures. Atmospheric pressure plasmas also showed similar behavior resulting in nanoparticle self-organization. This points to an exciting possibility of the formation of ordered nanostructures by atmospheric pressure plasma-based processes.

For these reasons, microplasma, in particular, atmospheric pressure plasma jets (APPJs), are expected to have significant control over the synthesis and applications of nanomaterials. This chapter summarizes the recent progress in plasma nanoscience, focusing on future directions of nanomaterial synthesis. We explore some fundamental

challenges facing nanomaterial synthesis that must be addressed and solved by plasma chemistry.

1.2 Trends and Directions in the Fabrication of Nanomaterials Using APPJs

In the past few decades, nanomaterials have received significant attention due to their characteristics considering their bulk counterparts: their extremely small size and high surface area contribute to the surface-enhanced properties. Besides the applications in electronic applications, they are also valuable for biomedical applications like drug delivery, bioimaging and cancer therapy [12][13][14]. However, due to their toxicity, these nanomaterials can be dangerous to living organisms. Namely, the conventional chemical approaches to the synthesis of nanomaterials use toxic chemicals as reductants or oxidants, which is necessary for the formation and stabilization of nanoparticles. Therefore, an alternative, non-toxic synthesis approach is crucial for developing nanotechnology in biomedical applications. For a "green" synthesis method for nanomaterials, plasma technology is now gaining consideration because of its distinctive properties in solid, liquid, and gas phase synthesis approaches [15][16]. This work focuses on advancing non-thermal atmospheric pressure plasmas and their role in synthesizing nanomaterials for a wide range of applications.

Physical plasmas are ionized gases formed by the dissociation of gas molecules with electrical energy, and they generally contain high-energy electrons, ions, excited species, neutral species, etc. These plasmas can be produced at low pressures as well as at atmospheric pressure [17]. Low-pressure plasmas are generated inside a vacuum chamber known as thermal or quasi-equilibrium low-temperature plasma [18]. At atmospheric pressures, plasmas could be ignited by ionizing the gas in the ambient environment, and no expensive vacuum is needed. Atmospheric pressure plasmas are also known as non-equilibrium or low-temperature plasma [19]. The electron temperature in atmospheric pressure plasma is higher than the ions and other gas species. Low-temperature atmospheric pressure plasmas like dielectric barrier discharges (DBD) or plasma jets can be used to treat or synthesize nanomaterials [20]. The reactive species generated in the ambient environment modify the surface properties of materials. Much research has been done in this field to design and perform high-quality synthesis and applications of nanomaterials [21][22][23]. A typical atmospheric plasma jet consists of a high voltage source connected to an electrode separated by a dielectric material, typically a glass tube. Plasma can be ignited with a consistent flow of an inert gas (He, Ar, etc.) which is in contact with the electrode and initiate the ionization of the gas, hence the plasma. The short-lived reactive species are carried towards a region where they come in contact with material [24][25]. Since the temperature of the plasma generated is close to room temperature, it can be used to synthesize nanomaterials or modify material surfaces.

There are many possibilities for atmospheric pressure plasma to have a direct/indirect influence on the synthesis of nanomaterials. This effect is more prominent when plasma interacts with the vapor phase, containing nanomaterials/precursors for nanomaterial synthesis. In an aqueous medium, plasma can generate H_2O_2, one of the most stable

reactive species and mediates the reduction of precursors like metal salts to give metal nanoparticles [26][27]. This easy and reliable reduction procedure in plasma can be used to synthesize nanoparticles of noble metals like Au, Ag, Pt, and Pd, which possess high demand in bulk as well as nanomaterial [28][29][30][31]. Moreover, nanometer-sized noble metal particles demonstrate unique properties, including the surface plasmon resonance phenomenon.

Plasma-based systems are also being considered as cost-efficient method for high-speed production of metal oxide nanoparticles. These metal oxide nanoparticles are relevant subject among researchers in biomedical fields because of its applications in biomedical sensing, drug delivery and biomedicine [32][33]. Many studies have been done in the synthesis of encapsulated nanoparticles of metal oxides as well. Up to date, plasma-assisted synthesis of metal oxides nanoparticles of Fe, Co, Ni, Cu, Zn etc. were successfully established and studied [23][24][25][26][27]. However, the formation of metal oxide nanoparticles in atmospheric pressure plasma by plasma-liquid interactions is a simple process because of the presence of strong oxidizing species in plasma, especially for transition metals, even though controlling the oxidation states of the transition metals is challenging.

1.3 Atmospheric Pressure Plasma Devices for Specific Applications

Atmospheric pressure plasmas are widely used for specific applications because of their practicability and simplicity, like in the surface treatment of a variety of materials, treatment of living cells or even material synthesis. The advantage of using atmospheric pressure plasmas is the ease of access to the materials. Depending on the purpose, the plasmas can be modified and enhanced accordingly. Modifying the power, source or modification of the electrodes will enable special geometries and interactions with the materials. In relation to the plasma geometries and connected types of discharges, atmospheric pressure plasmas can be classified as follows in subchapters.

1.3.1 Dielectric Barrier Discharges

Dielectric barrier discharges (DBD) are also known as “atmospheric-pressure-glow” discharges [34][35][36]. A schematic of this source is shown in Figure 1.1. They usually consist of two metal electrodes one of which at least is coated with a dielectric material layer. The gap in between the electrodes would be several millimeters with an applied voltage of around 20 kV.

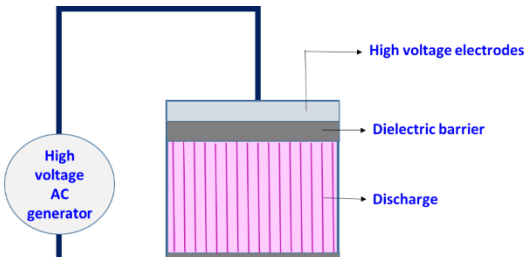

Figure 1.1: Typical construction of a DBD device wherein one of the two electrodes is covered with a dielectric barrier material. The lines between the dielectric and the electrode are representative of the discharge filaments.

The plasma is generated through a sequence of micro arcs randomly distributed in space and time and would last for 10-100 ns. The diameter of these plasma streamers is believed to be around 100 µm, and the separation between them could be around 2 cm [34][36].

This type of plasma is very commonly used for various material processing procedures like plasma-assisted chemical vapor deposition, polymer synthesis by a chemical vapor deposition process, surface treatment of metals, deposition of metal oxide films on the surface etc. [37][38][39]. However, one of the main drawbacks of these processes is that plasma is not uniform and hence the deposition is irregular and cannot be used for smooth and uniform depositions. Dielectric barrier discharges are very efficient in industrial applications and well-proven ozone generators in environmental engineering (used for waste-water treatments, paper bleaching, cleaning etc.) [39]. They are also used in gas chromatography techniques as a barrier ionization discharge detector (BID). The detector uses high-energy photons of the plasma (He plasma) to ionize the molecules of the samples. Since practically all substances (except neon and helium themselves) have a lower ionization potential, this detector can be described as universal.

1.3.2 Radio Frequency Plasma Jets

Radio frequency (RF) high voltage is one of the most frequently used methods for the excitation and sustentation of plasmas. A large number of RF-driven plasma jets have been designed and utilized in many fields through the years. Low-temperature atmospheric-pressure radio frequency (RF) plasmas offer an interesting alternative to conventional low-pressure discharges and are being explored for a wide range of applications. The plasma density that can be achieved in these discharges is limited by the loss of plasma uniformity with increasing input power. Although at low power, uniform glow-like discharges suitable for practical applications can be generated, atmospheric pressure discharges are very susceptible to constrict radially. This transition is very rapid because of the negative differential impedance of the plasma, which eventually turns the plasma into a high-temperature arc. An ability to control the operation of the plasma in this negative differential impedance region allows for the stabilization of the discharge,

extending the glow-like operation regime. Such stabilization can be achieved by using a current-controlled power supply or by introducing dielectric barriers in the discharge.

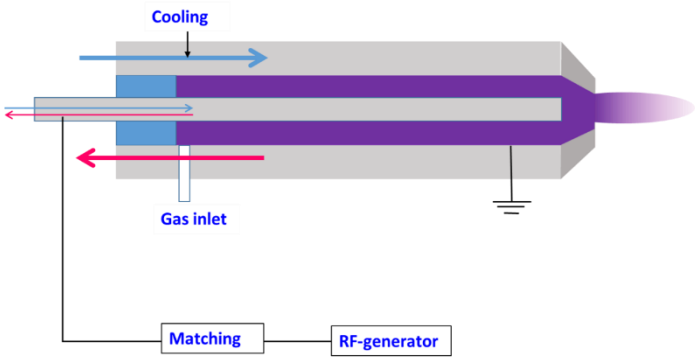

Figure 1.2: Typical set-up of a radio-frequency atmospheric pressure plasma jet.

Another issue is, as the RF frequency increases, the electron temperature decreases due to the reduction of driving voltage. This results in a decrease in excitation and ionization. At the same time, the electric field in the bulk plasma increases, leading to enhanced heating of the bulk electrons. Despite the increase in electron temperature (and absorbed power) in the bulk plasma as frequency increases, the electron temperature is too low for electrons in the bulk to contribute significantly to the excitation of the background gas. The net result of the reduction of the electron temperature and the increase in the bulk is an overall increase in the electron power consumption and a decrease in the excitation/ionization of the neutral gas. This strong dependence of the electron temperature on the driving RF frequency could be exploited to tailor the plasma chemistry for a given application.

1.3.3 APPJs

Plasma jets are improved designs of DBD. In plasma jets, the plasma plum is extended at a long distance from the discharge region, which enables remote treatment of samples and surfaces. There are a lot of research work has been done on designing different plasma jets for various applications such as biomedical applications (skin treatments, cancer therapy, blood coagulation etc.), agricultural applications (sterilization of vegetables, sterilization of seeds, increasing the germination rate of seeds), and material processing like synthesis and processing of films and coatings, surface modification etc.

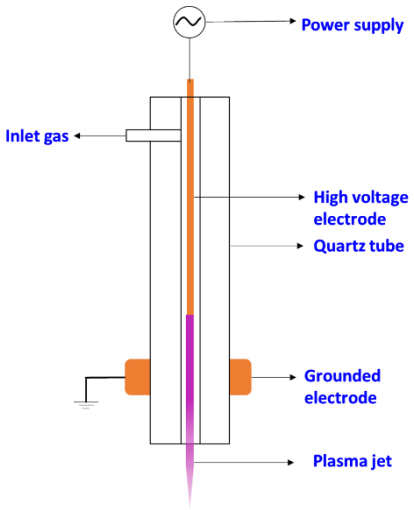

Figure 1.3: Schematic representation of the atmospheric pressure plasma jet configuration.

The atmospheric pressure plasma jet operates in a configuration using RF/AC high voltage power supply and produces a stable, uniform glow discharge from the tip of the metallic electrode and the length of the discharge can be extended with respect to the power and the position of the grounded electrode. However, the operation is restricted to a feedstock gas consisting predominantly of a rare gas with only a small admixture of molecular gas.

1.3.4 Application of APPJs for the Synthesis and Modification of Materials

Currently available modification and deposition methods use gas discharges working at low pressures. Usually, the reaction temperature would not rise much because the chemical reactions are initiated by charged particles inside the plasma. However, the low-pressure techniques require proper vacuum equipment. On the other hand, processes at atmospheric pressure are less hectic and more favorable in way similar results from the existing methods can be accomplished. APPJs open a new era to plasma-assisted synthesis methods at atmospheric pressure itself. These plasm discharges have numerous transient micro discharges in parallel, and these micro discharges are statistically distributed on the substrate surface. This property of atmospheric pressure plasma can be used in synthesis and deposition of a number of materials like polymeric films on glass surfaces or in the modification of material surface. However, the parameters affecting the deposition or surface modifications can vary according to the atmospheric conditions, materials, substrates etc. Besides, further improvements to the deposition/modification process are easy to implement in non-equilibrium atmospheric pressure plasma processes.

Widespread utilization of microplasma for nanomaterials synthesis will depend on the ability to scale up current processes to industrial-level manufacturing and/or fabricate

well-defined materials that are not capable of being produced by other methods. Prior research has demonstrated that there is commercial potential for microplasma-based systems in areas like thin film deposition of nanostructured coatings, nanocomposite films and self-organized structures and preparation of well-defined 'freestanding' nanostructures (e.g. nanoparticles, nanotubes) as powders or colloidal dispersions. In either case, there are several issues that must be considered including the quality of as-grown material in terms of homogeneity and structure, throughput (i.e. production rate), process cost and process safety. The quality of as-grown material depends on the desired application—for example, in some cases; the size of the nanomaterial may be important and must be precisely controlled whereas in others, the composition is critical. Microplasmas are capable of producing a wide range of materials with well-defined structures and under various conditions, which could make them flexible for different applications. The throughput of material is currently a challenge since most previous studies are lab-scale and only require small amounts of material (e.g. nanograms); however, microplasmas can be operated in parallel to increase the production rate of nanomaterials. However, they are more relevant and easier techniques in many applications lately. Several applications can be found associated with APPJs, like modification, surface funtionalizations, depositions etc.; a few are mentioned below.

a) Surface modification by APPJ in material science: Plasma treatments are widely used to modify the surface of various materials, such as polymers and metals. The purposes can vary widely from surface cleaning to improvement of hydrophilic or hydrophobic nature (in particular, the hydrophilic character of some materials can be enhanced by argon plasma treatment.) or surface activation [11][12][13][14]. APPJs are very effective in material processing especially suitable for materials, which are sensitive to heat (thermal damage). Among these applications, the treatment of polymer surfaces should be emphasized. Polymers usually have low surface energy, which causes poor adhesion. In such cases, APPJs can be used to activate the surface and thereby the surface adhesion [15]. Along with the treatment of polymers, APPJs can also be used in the treatment of metals and semiconductors; to be specific in the treatment of titanium surfaces to improve growth and cell adhesion [16]. APPJ treatments can also be used to treat silicon surfaces to create grid patterns; grid patterns of the extracellular matrix could be developed with low-temperature atmospheric pressure plasma [17]. Etching of fused silica is also found successful by APPJ using an Ar/CF_4 gas mixture, which leads to the formations of a number of nanometer-sized pits [18]. Furthermore, photoresists could also be etched by APPJs working with Ar/Air mixtures [19].

b) Deposition of coating/nanomaterials by APPJ: Compared with the surface treatments, there are more twists and turns in the deposition by means of APPJs. First, an additional precursor is required for depositions, usually in the vapor state. Metal-organics, silicon organics or various inorganic solutions are commonly used precursors for the deposition of coatings and nanomaterials, in some of which the additional energy coming from the combustion of organic liquids can be utilized for the deposition process. In APPJ-mediated depositions, liquid precursors are

typically atomized or vaporized in order to transfer to the working volume of the APPJ setup. There are some cases that use liquid precursors directly injected into the plasma systems, which are more complicated [20]. However, the interaction between plasma and the precursor is dependent upon its atomization behavior. In literature, APPJs are widely used to deposit metal oxide films, such as ZnO [21][22][23]. Depositions of metal oxide films of silicon and aluminum were also reported [12]. The benefit of atmospheric pressure plasmas in synthesizing or depositing materials is their high selectivity, which mediates the fabrication of materials on the substrates. Not only metal oxides, but metal nanoparticles can also be deposited on various substrates using an APPJ. The percentage of nanoparticle content on the depositions and their morphology can be controlled.

c) Biomedical applications of APPJ: The research on biomedical applications of non-equilibrium plasmas, also known as plasma medicine, started in the middle of the 1990s seeking the use of plasmas to decontaminate biotic media; such as tissue and skin, and abiotic media and surfaces [24]. The aim of the practice was to use plasma technology to sterilize tools and disinfect wounds for rapid healing. Even though high-temperature plasmas are well known for sterilization purposes, using them in therapeutic applications can cause lethal damage to living systems. But recent improvements in atmospheric pressure plasmas guarantee high performance low-temperature plasmas for biomedical applications [25]. Non-thermal atmospheric pressure plasmas operate at temperatures slightly above room temperature (35°C) but they are very effective in bacterial inactivation [26], sterilization [27], dentistry [28][29], wound healing [30], treatment of cancer cells [29], genetics [31], etc. Nevertheless, non-equilibrium APPJs generate plasma in an open space rather than in a confined space, which is much more suitable for plasma medicine. On the other hand, the advances achieved with APPJs in the past decade have greatly pushed forward the research in plasma medicine. In addition, the urgent demand for suitable plasma sources has attracted significant effort to develop, optimize, and understand APPJs. The number of publications in both plasma medicine and APPJs has grown exponentially in the past decade. Today, work on plasma-aided wound healing, blood coagulation, dentistry, cancer treatment, and much more is going on in earnest at several laboratories worldwide.

d) Nanomaterial processing and modification - material synthesis using atmospheric pressure plasmas: Material processing via microplasma jets are fascinating because of the ideal approaches such as localized deposition and surface functionalization. Previous reports have demonstrated the deposition of patterned nanostructured coatings [32] using atmospheric pressure plasmas. To make this plasma technology compatible with large scales, an array of microplasma jets can be considered. However, the focus of APPJs is on localized depositions and nanomaterial fabrication. Compared with other means of material fabrication, atmospheric pressure plasmas offer active species responsible for the chemical reactions which can be applied to the surface of interest, instead of placing the samples inside the

reactor. The technique is very relevant to sensitive surfaces, and thin films that require moderate treatments.

The interactions of atmospheric pressure plasmas with liquids are as fascinating as in nanomaterial fabrication. Plasma-liquid chemistry has been studied for more than 100 years, about plasmas formed inside or on the surface of the liquids [33]. Because of the potential applications of nanomaterials in nanomedicine and nanoelectronics, the interest in precise synthesis of nanoparticles and nanomaterials using plasma has grown due to its simplicity when using the precursors. Moreover, the plasma interface with liquids and vapors could enable synthesis and/or functionalization of nanostructures in the same phase [34]. One of the main advantages of the plasma-liquid chemistry is its compatibility with applications such as analytical chemistry and medicine; either dry products like depositions of nanomaterials from liquid/vapor phase, or colloidal dispersions. On the other hand, nanomaterials synthesized in liquid phase in low pressure plasmas are limited to applications involving liquids with low vapor pressures, like ionic liquids. In recent years, non-thermal atmospheric pressure plasmas are adding up their capacity to use various liquids or mixture of liquids. Most common liquid entities used in atmospheric pressure plasma processing is water as a solvent; plasmas formed at liquid/vapor interfaces to form metal nanoparticles in aqueous solutions [35][36], ethanol is also a common precursor. These solvents can be easily incorporated with atmospheric pressure plasma in-situ or ex-situ. However, compatible liquid mixtures (water-ethanol, for instance) can also be a promising solvent or precursor material for various metal nanoparticle fabrication. The mechanisms that lead to the formation of nanoparticles remains unclear or poorly understood because of the unpredictability of plasmas. But the reactions at the gas/liquid/vapor-plasma interfaces are generally initiated and carried over by the in-house electrons of plasma during the process, which depicts a fast and unique reaction mechanism.

1.4 Fabrication of Nanoparticles of Metal/Metal Oxides in a Single Step

Over the last decade, there has been a rapid rise in the number of reports in the literature that discuss applications of microplasmas for nanomaterials synthesis. The broad range of configurations that have been explored illustrates the versatility of microplasma sources but also makes a comprehensive classification of all the studies quite daunting. Nonetheless, there are some common features; for example, most of the configurations that have been used for nanomaterials synthesis are continuous and operated at a steady state. As stated earlier, this is not surprising since continuous processes are particularly useful for nanomaterials synthesis to control the nucleation and growth, with the easy collection of products. Many of the experiments involve a single microplasma source to prepare materials locally, sufficient for lab-scale studies, but a potential drawback for large-scale applications. Otherwise, the experimental details of each process vary quite dramatically and can be differentiated by various process parameters such as the electrode geometry,

frequency of the power coupling, specific material chemistry, and method of introducing precursor and how the product is collected.

1.4.1 Plasma – Liquid/Vapor Chemistry

Plasma-liquid/vapor chemistry is a new direction in plasma science in corporation with wet phase systems. Even though the ow-pressure or thermal plasmas were in use for over 100 years, their use in liquid systems was limited because of the compatibility and the evaporation of the liquids in longer time scales. Also, the process required external cooling to prevent the evaporation of the liquids. However, the non-thermal processing of the atmospheric pressure plasmas has made a huge impact on material processing. The interface with atmospheric pressure plasmas is more stable in such a way that common liquids like water can be used in the process and can be applied in many situations like water treatment or chemical processing and analysis. In the case of chemical processing, the plasma-liquid/vapor interactions open up new pathways which may lead to the direct formation of nanomaterials inside the plasma or in the liquid. The formation of nanoparticles using atmospheric pressure plasmas is well-established method and a lot of studies and mechanisms are being studied.

Earlier reports declared platinum nanoparticles were synthesized using an APPJ ignited with hydrogen gas on the surface of aqueous solution of hexachloroplatinic acid (H_2 [$PtCl_6$]) [35]. The research suggests that the plasma-generated ions, excited species, atoms or electrons inside the plasma during the process can facilitate the reduction of $(PtCl_6)^{2-}$ ions inside the solution. Furthermore, followed by the reduction, the platinum seeds nucleate and form nanoparticles. They monitored the growth of the particles and found out that the estimated growth is 1.2×10^{-5} mol/min, from the UV-vis absorption spectra. This reduction rate is comparable to other reduction methods in use. Also, the article reports the synthesis of spherical, extremely small platinum nanoparticles of diameter 2 nm with uniform size distribution. However, there has been research to reduce the metal salts with atmospheric pressure plasmas to see just the plasma species can reduce the metal salts. The research could be a breakthrough because unlike conventional methods including the colloidal growth method, plasma processing does not require any critical conditions or external chemical reducing agents like sodium borohydride ($NaBH_4$) and can be considered a biocompatible method. Moreover, since the method does not use any surfactants or stabilizers, the nanoparticles can be selectively modified or functionalized.

However, the reduction mechanism of the species inside the plasma involving metals was unclear particularly if H_2 gas is not taking part in the process, but, there can be similar mechanisms with water. Water can easily generate oxidizing and reducing agents with plasma caused by the electron impact dissociation within the water. The dissociation can generate hydrogen and hydroxyl radicals, and hydrogen peroxide which is a reducing agent for metals like gold. In atmospheric pressure plasmas presence of nitrogen and oxygen reactive species is also possible which can contribute to the plasma-liquid interactions and reduce the metal cations. Sankaran et al., in one of their findings, have shown that electrochemical reactions can be simply initiated by microplasmas, reactions similar to electrochemical cells [37]. The only difference is that these reactions are caused by the interactions of gas-phase electrons with metal ions in the solutions. In their work, they

created a dc microplasma at the surface of the electrolyte solution which is performed as a cathode, and a solid metal electrode immersed in the electrolyte operated as an anode.

The setup created an electrochemical cell. A current flow has been created as a result of the plasma ignition and half-cell reactions were observed at the anode and cathode. The oxidation reactions at the cathode followed by the dissolution of the metal-to-metal cations were then got reduced to metal in the cathode (electrolyte solution) and nucleation and growth of the nanoparticles in interaction with the microplasma.

From similar investigations and observations, conclusions are made such that the gaseous electrons from the plasma can interact with a solution at the interface (plasma-liquid boundary) or at the surface of the liquid which can lead to electrochemical reactions (as shown in Figure 1.4). Similar interactions were also reported with large volume glow discharges with inert gases and low operating pressure that could lead to the reduction of metal cations.

Whether at the surface or below the surface, there is a significant scope of plasma-liquid interactions even if the plasma is generated outside the liquid. On the other hand, the measurement of species is challenging both in gaseous and liquid phases. Despite that, these near-surface interactions could be very interesting for plasma medicine and plasma-nanoscience. However, there should be considerable understanding of the interactions of traditional gas phase plasma chemistry with biological fluids and their uses for specific purposes. This particular interfacial plasma (near the liquid surface) can also be considered as plasma-vapor because at the interface it is more or less in vapor state. This cocktail plasma is composed of radicals, ions, electrons and photons, which can interact and initiate a cascade of reactions in the interface followed by the chemical reactions in the liquid. However, the very important electron interactions directly with the vapor phase are often neglected in most studies.

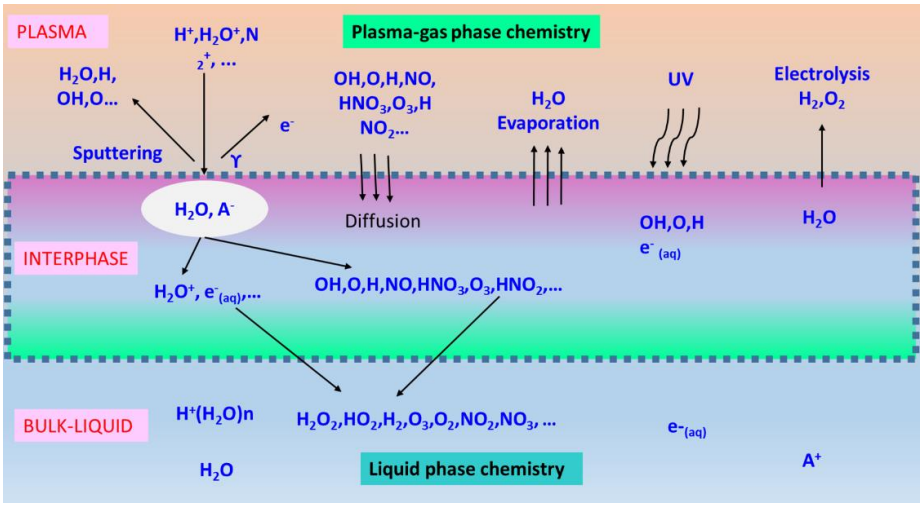

Figure 1.4: Schematic overview of some important transfer processes at the plasma–liquid interface.

Electrons leave the bulk plasma with energies that depend on the plasma type and configuration used; however, we can expect highly energetic electrons to arrive at the liquid surface (up to a few eVs) giving rise to different energy-dependent reaction paths. An

example of an energy-dependent electron-induced reaction is dissociative electron attachment (DEA). Ideally, different molecular fragments could be selectively dissociated from the same target molecule. While the DEA reactions between electrons and single molecules within the plasma phase are well understood, actual plasma-induced DEA in liquid has yet to be observed directly and the interaction between plasma and bulk liquid or even droplets may well present a much more complex picture that has recently generated considerable research interest [40][41]. Furthermore, electron-induced reactions taking place at the interface differ from electron-induced reactions occurring in the gas phase because, in the former, electrons have the opportunity to interact with liquid chemical species that are not present in the gas phase. In addition, the products of the reactions taking place at the plasma–liquid interface will tend to remain in the liquid phase leading to cascaded liquid-based chemistry. Cascaded liquid-based chemistry presents a scenario largely dominated by molecular potentials and reaction activation energies. This differs from the gas-phase chemistry in plasmas where the species and in particular charged species behave as isolated entities. With these isolated entities, the kinetic energies play an important role in determining reactions.

The rapidly increasing interest in the formation and interaction of plasmas in atmospheric pressures with liquid/vapor precursors appears to be a natural progression of plasma nanoscience. Moving to the vapor phase increases the dependency of the volatility of the liquid more significantly than increasing gas pressure and results in additional captivity of atmospheric pressure plasmas. Highly localized, remotely generated discharges offer a potential route to reduction and growth or deposition of pattern materials directly at the nanoscale. Synthesis of metallic and non-metallic (such as carbon) nanomaterials in higher production rates is possible in vapor phase. Future studies will need to accomplish unique processing set up and operating conditions to fabricate nanomaterials that hold great promise for many applications.

1.4.2 Instantaneous Reduction of Metal Salts by Plasma-Vapor Chemistry and Compatibility of the Precursors

The reduction mechanism of metal salts in the plasma-vapor interface would rather be explained as a combination of plasma-liquid phase chemistry and plasma-gas phase chemistry. This can be called a plasma-vapor interface where the wet electrons and plasma species play the key role in the reduction of metal salts and synthesis of metal nanoparticles.

The fast electrons are created by the discharge and initiate the chemistry, which takes place in the plasma. The electrons collide with the gas/vapor molecules and excite them to higher energy levels, thereby losing the corresponding amount of energy. The excited molecules can now initiate reactions because of their higher internal energy.

Water-based solutions need to be used to simplify the reduction inside the plasma. In other words, water-soluble metal salts should be used for the plasma-induced reduction process. The hydrate ions and hydrogen peroxide ions act as reducing agents for the reduction of metal salts. The formation of H_2O_2 is a consequence of reactions occurring at the plasma–liquid interface. Because H_2O_2 cannot be observed without plasma, it is evident that plasma electrons contribute to or initiate reactions in the bulk liquid through the

plasma–liquid interface; however, at this time, we cannot confirm the mechanism. As previously discussed, DEA is a possible type of reaction that can occur at the plasma–liquid interface. Dissociative electronic attachment to water exhibits resonant peaks for various electron energies above 6 eV and can produce a range of radicals and ions such as $OH^{\bullet}$, OH, O, and H. For these reactions, the dominant reactive channel is water.

The formation of hydrogen peroxide should result from subsequent cascaded chemistry and, therefore may originate from either $OH^{\bullet}$ or OH. Because the reaction 2 $OH^{\bullet}$ to H_2O_2 is energetically most probable, the formation of hydrogen peroxide could indicate that OH radicals are formed at the plasma–liquid interface. Therefore, DEA reactions may be prevailing in this case. However, the complexity and number of possible reactions necessarily could be complemented with simulations if needed.

1.5 Remarks on the Fabrication of Nanomaterials Using APPJs

The manipulation of atmospheric pressure plasma procedures can only be achieved by understanding the physical and chemical properties of each plasma system used in respective practices and the precursors. However, most plasma-assisted material fabrication methods are used in industrial processes even with partial knowledge of chemical and physical properties coupled with plasma. Nevertheless, the area, especially non-equilibrium atmospheric pressure plasmas, is often non-predictive in nature; hence, the amendment of synthesis processes is without the risk of product loss. Thus, the advancement of the atmospheric pressure plasma processing can be accomplished by wise selection of plasma system and the raw materials for the synthesis.

Gaining a detailed understanding of physical and chemical mechanisms inside the corresponding plasma systems intricately provides the database for the qualitative analysis of plasma interactions. Characterizing the electron-ion-photon interactions, such as collisions, with atomic and molecular species within the plasma, would facilitate the formulation of modified synthesis procedures over time.

A wide variety of configurations can be used to produce plasma–liquid systems. In this contribution, we have focused on a simple DC atmospheric pressure microplasma to highlight interesting aspects that derive from the interaction of plasma electrons with a solution. More specifically, electron-induced reactions have been used for the synthesis and functionalization of nanomaterials. Gold NPs synthesis and functionalization of quantum confined silicon nanocrystals have been discussed in more detail as examples. While the literature already reports the possibility of synthesizing and functionalizing a range of other nanomaterials, the reaction paths, and growth mechanisms are still largely unknown. Future research efforts should therefore produce hybrid models that can describe the exchanges between the plasma phase and the liquid solution.

It should be noted that for nanomaterials processing, the plasma model might not require an accurate set of gas-phase chemical reactions. Understanding the mechanisms involved in plasma–liquid interactions, together with experimental investigations, should lead the way to precision synthesis with accurate control over nanomaterial morphologies. Furthermore, the use of more complex chemistries may open the possibility of producing

composite and self-organized nano architectures. There is no doubt that plasma-vapor chemistry at atmospheric pressure represents a new and growing field that will challenge traditional wet chemical methods for nanomaterials synthesis. Nonetheless, the impact of plasma–liquid interactions should be considered in a much broader sense as it represents a fundamentally new approach to activating chemical reactions in liquids. The emerging field of plasma medicine results from such an approach, and many more applications will follow. Although clear challenges will be encountered for scaled-up or industrially viable processes, plasma-vapor chemistry can greatly impact various application fields. Here, we would like to emphasize that a larger effort on basic fundamental studies is required to support balanced progress in the field adequately. The risk is that without scientific understanding, technological progress will be hindered.

1.6 Objectives and Hypothesis

The purpose of this PhD is to fabricate a fast and reliable synthesis procedure for the generation of nanoparticles that are high in demand for various applications. This work would contribute to the solution and replacement of complex synthesis methods that currently exist, specifically as follows:

a) The work would be the solution for gold nanoparticle synthesis, replacing toxic chemical procedures and time-consuming biological procedures with an atmospheric pressure plasma jet (APPJ), which does not require any external reducing agents or surfactants. Moreover, in other methods with the use of reducing agents or surfactants, purification of the final product would be an extra step. Here, in plasma procedure, we can avoid that process as well.
b) This PhD should be an answer for a fast and reliable method for the preparation of pure nanoparticles of metals and metal oxides, which are widely used for sensitive applications. At the same time, the procedure is financially viable and easy to implement.
c) This PhD should address the solution of a non-toxic procedure, which is very relevant environmentally and in individual health and safety; a plasma-chemical procedure only needs a metal precursor, and there is no byproduct.
d) The atmospheric pressure plasma chemistry would back up the instantaneous reduction of metal salts, which readily leads to the synthesis followed by the rapid quenching and deposition of nanoparticles. The conventional biological non-toxic procedures would take hours or even days to complete the reaction.
e) This PhD work should be a key to easy and economical synthesis of active nanoparticles for sensing applications in nanoscience and nanotechnology research.

The hypothesis of the PhD thesis is that the atmospheric pressure plasma jets generated within an inert gas flow could offer a new tool, which would facilitate simultaneous reduction and/or formation of nanoparticles and instantaneous deposition of size controllable plasmonic gold and metal oxide nanoparticles. This synthesis mechanism

would improve current state-of-the art on the field of synthesizing non-toxic metal-metal oxide nanoparticles for various applications.

The objective of this PhD thesis is to meet the purpose of conveying an easy platform for the synthesis of metal and metal oxide nanoparticles. The work is targeted at:

1. Designing and assembling a plasma deposition system employing atmospheric pressure plasma jet as a tool.
2. Formulation of favorable atmospheric pressure plasma conditions such as gas flow, power etc. which would influence the reduction/synthesis rate of metal or metal oxide nanoparticles.
3. Interpretation of possible plasma mechanisms for the formation of nanoparticles.
4. Analysis and scope of synthesized nanoparticles according to their size, shape and physiochemical characteristics, for instance, plasmonic behavior of polyhedral nanocrystals of gold.
5. Investigation of the applications of plasma-generated nanoparticles in bio-sensing applications utilizing the molecular attributes of the nanoparticles; nanoelectronics devices, plasmonic sensors, etc.

Chapter 2

Deposition of Precious Metal Nanoparticles with Atmospheric Pressure Plasma Jet

As the demand for highly pure metal nanoparticles increases, we are exploring new aspects of science to innovate existing synthesis techniques. However, some of the techniques get more complicated while they yield highly pure nanoparticles or get more time-consuming and problematic multiple steps. Atmospheric pressure plasma jets could be a simple solution to the existing problem. This chapter is a research article depicting a new method for the instantaneous reduction and deposition of metal nanoparticles using an atmospheric pressure plasma jet has been described. Experimental optimization to get pure nanoparticles of gold (Au) from hydrogen chloroauric acid ($HAuCl_4$) using an atmospheric pressure plasma jet has been established in this chapter. In addition, the non-equilibrium atmospheric pressure plasma chemistry in interaction with the vapor is explained. The mechanism of formation of nanoparticles is believed to be initiated by the high-energy electrons from the plasma. The precursor is used as a solution in water as well as in ethanol to study the effect of the solvent in the vapor that interacts with plasma. It was found that as the ethanol concentration increases, the deposition rate increases.

Regarding the contribution of the author: The author of the dissertation has contributed to the idea and carried out the experimental work of plasma deposition.

(*Article has been submitted the Journal of Alloys and Compounds*)

From Faceted Nanoparticles to Nanoporous Film by Plasma-Jet Redox Reaction of Ionic Gold

Aswathy Vasudevan [a, b], Vasyl Shvalya [a], Martin Košiček [a, b], Janez Zavašnik [a, b], Andrea Jurov [a, c], Neelakandan M Santosh [a], Aleksander Zidanšek [b, d, e], Uroš Cvelbar [a, b] *

[a] Department of Gaseous Electronics (F6), Jožef Stefan Institute, Jamova cesta 39, SI-1000 Ljubljana, Slovenia

[b] Jožef Stefan International Postgraduate School, Jamova cesta 39, SI-1000 Ljubljana, Slovenia

[c] University of Zagreb, Faculty of Chemical Engineering and Technology, Department of Inorganic Chemical Technology and Non-Metals, Trg Marka Marulica 20, Zagreb 10000, Croatia

[d] Department of Condensed Matter Physics (F5), Jožef Stefan Institute, Jamova cesta 39, SI-1000 Ljubljana, Slovenia

[e] Faculty of Natural Sciences and Mathematics, University of Maribor, 2000 Maribor, Slovenia

* Corresponding author: uros.cvelbar@ijs.si (U. Cvelbar)

Abstract

Cold-atmospheric plasma-assisted deposition has emerged as an efficient technique for synthesising gold nanoparticles (AuNPs). Here, a plasma-vapour interaction is used for the simultaneous reduction and deposition of AuNPs from an inorganic precursor ($HAuCl_4$). As surface analyses suggest, plasma input power plays an important role in reduction efficiency, whereas argon gas flow rate reduction leads to the formation of smaller particles. This study demonstrates that the presence of ethanol in the reactive mixture of gold promotes improved reduction of gold to nanostructures owing to their volatile properties. A systematic investigation of plasma and the deposited nanostructures reveals that the reduction is mainly caused by the free electrons and *in-situ* formation of hydrogen peroxide inside plasma. Our method demonstrates that a uniform AuNP film can be created within 5 min by controlling plasma parameters. Deposited AuNPs feature advanced plasmonic surface-enhanced Raman scattering responses, tested with Raman marker Rhodamine R6G, enabling their use as a potential substrate for fast and reliable optical analytical biochemical sensing.

Keywords: plasma redox reaction, atmospheric pressure plasma jet, gold nanoparticles, surface-enhanced Raman scattering (SERS)

Graphical Abstract

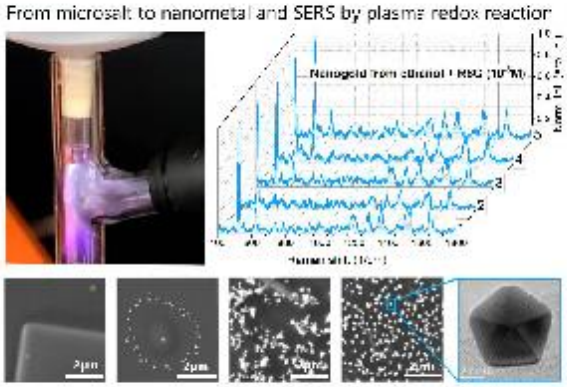

1. Introduction

The need for better synthesis approaches to design metal nanoobjects of desired size and shape has generated significant research attention in the field of nanoelectronics device development. At a reduced scale, metal nanoparticles are known to exhibit enhanced surface electron activity and better optical/catalytic properties, mainly due to the surface and structural defects. This has been used to advance electrical and electrochemical performance of various functional metals [1–3]. Lately, gold has been one of the most comprehensively explored metals, being also a material of frequent choice to improve the operational characteristics of analytical and diagnostic devices [4,5]. Faceted gold nanoparticles also possess excellent plasmonic features beneficial for theranostic and nanomedicine applications [6–8]. High demand for high purity/quality gold nanoparticles (AuNPs) has prompted the exploration of various research approaches targeting a fast, facile and low-cost synthesis technique for nanogold structures. A variety of bottom-up methodologies, including laser ablation, chemical, electrochemical and sonochemical pathways, have so far been investigated for synthesising AuNPs [9–13]. Approaches, such as chemical or electrochemical and thermal reduction procedures, include multiple complex steps and demand further purification or centrifuge-based particle separation techniques.

Generally, the preparation of nanogold by chemical reduction procedures has two main parts: a) reduction of the precursor material by a reducing agent, and b) stabilisation of the product to avoid particle aggregation. One of the most used techniques for synthesising AuNPs is based on the Turkevich method from 1951, which involves the reduction of $HAuCl_4$ by sodium citrate in water [14]. This method can effectively produce AuNPs below 100 nm in diameter. Similar reduction mechanisms were established using the reduction of $HAuCl_4$ and chloroaurate $(AuCl_4)^-$, by controlling the ratio between the reducing agent (trisodium citrate) and the stabilising agent (gold) [15,16]. Later, Brust and Schiffrin in 1994, brought about a phase-

transferring reduction-based mechanism for synthesising AuNPs [17]. Here, the chloroaurate ions were transferred into a toluene phase from the aqueous solution, employing tetraoctylammonium bromide as the phase-transferring agent, followed by reduction using $NaBH_4$ in the presence of dodecanethiol. Although chemical methods are the most common procedures for synthesising metal nanoparticles, toxic reagents and stabilising agents involved during synthesis hinder their large-scale use in many application areas.

Electrochemical synthesis using a simple two-electrode cell, followed by oxidation of the anode and reduction of the cathode, was also reported to synthesise AuNPs [18]. The method has been successful owing to its ability to control nanoparticle yield. In addition, new approaches have been developed, such as seeding AuNP growth and biological methods, which involve mild toxic agents for nanoparticle production compared to chemical methods. However, these nanogold synthesis reactions are time-consuming (a couple of hours to several days) [19,20]. Laser ablation is also reported as an alternative technique to rapidly prepare nanometric-sized particles as colloids [21].

All of the techniques mentioned above are limited when dealing with the direct deposition of synthesised particles for electric circuits and advanced electronic applications. Direct deposition of gold particles is widely achieved by the drop-casting method. This technique is simple but lacks control in terms of the distribution of nanoobjects and their aggregation on top of various surfaces. Moreover, nanoparticle attachment on the substrate is not sufficiently strong; nanoparticles can be peeled off with water rinsing or compressed air while drying, unless chemical adsorption is involved.

Therefore, an advanced technique that allows the synthesis and direct deposition of AuNPs on different substrates with high controllability and eco-friendly production is needed. In this aspect, plasma-enabled technologies have emerged as an alternative technique for the controlled synthesis of AuNPs. Among different plasma-deposition techniques, an atmospheric pressure

plasma jet (APPJ)-based electrochemical reduction of the liquid precursor has been explored to overcome the bottlenecks of nanomaterials synthesis. Atmospheric-pressure plasmas provide fast and controllable nanoobject design at low cost [22,23]. During the plasma–liquid interaction, when the plasma generated from an APPJ system interacts with water in the vapour phase, the high density of gas-phase plasma electrons creates a rapid cascade of nonlinear chemical reactions. In the case of gold-containing aqueous solutions, such plasma interactions create highly reactive radicals ($H^{\bullet}$ and $OH^{\bullet}$) [24,25] responsible for the successful synthesis of nanogold. Also, unlike conventional nanogold production methods, plasma-enhanced vapour deposition is highly reproducible and facile because it does not require external reducing agents. By simply treating $HAuCl_4$/sodium citrate aqueous solution with an Ar gas pulsed-power plasma jet, nanogold can be synthesised [26]. Moreover, nanoparticle attachment on the surface is more reliable than drop-casting [27].

Here, we demonstrate the feasibility of an APPJ system for the controlled synthesis of AuNPs with different morphologies. The present work investigates combined features of the APPJ system during nanogold synthesis: (i) nearly instant reduction processing for high purity gold nanocrystal growth, and (ii) improved adhesion of noble metal nanoobjects on the substrate surface. As a result of these combined effects, nanogold structures are successfully fabricated and deposited on the substrate surface with controlled spacing. Additionally, we reveal that nanogold can be produced in the form of coupled AuNPs and nanoporous film structures by varying the gas and liquid phase interaction between plasma and water, water-ethanol and ethanol vapours, all containing Au-salt originating from $HAuCl_4$ precursor. The demonstrated method suggests that continuous films of AuNPs can be synthesised within 5 min at low power and cost. The deposited nanogold structures have promising plasmonic properties, which are tested for detecting biological dyes using surface-enhanced Raman scattering (SERS). These

advantageous features will enable a future pathway for designing advanced plasmonic substrates at low cost for different electronic and optical sensing applications.

2. Experimental Section

2.1. Materials

Crystalline hydrogen tetrachloroaurate (III) hydrate (99.9% metal basis, Au 49% min) was purchased from Alfa Aesar by Thermo Fisher (Kandel) GmbH, Germany. The precursor was analytical grade and used without further purification.

2.2. Synthesis of gold nanocrystals

2.9 mM precursor solution was made with $HAuCl_4 \cdot 3H_2O$ in distilled water. The precursor was then kept at 80 °C with stirring and cooled to room temperature before transferring to the experimental setup. A part of the solution was then transferred to a nebuliser. The synthesis setup comprised an APPJ connected to a high-voltage power supply and an inlet for He working gas, and a nebuliser containing the precursor, connected to a gas inlet with Ar for nebulisation followed by atomisation. The atomised precursor droplets were then introduced to the plasma in the Ar gas range 1000–2000 sccm to observe Ar flow rate dependence (feed/carrier gas) in the deposition. Plasma was ignited with He at a flow rate of 290 sccm and interacted with the feed. Three specific calibrated values of power were used to ignite the plasma and to examine the dependence of applied power on the formation of nanoparticles. A silicon substrate was used for deposition and placed under the plasma stream at a distance of 1.5 cm. Nanoparticles formed inside the plasma were directly collected on the silicon substrate. Plasma deposition was conducted for 5 min to produce different nanogold structures. The same procedure was repeated with different solvent concentrations of deionised water and ethanol; 3:1, 1:1 and 1:3 of water and ethanol, respectively, with the same concentration of $HAuCl_4$.

2.3. Characterisation Techniques

Surface morphology and chemical features of the fabricated nanoparticles using APPJ deposition were studied using different characterisation techniques. Plasma excited species were analysed by emission spectroscopy. Detailed information on the characterisation techniques is given below.

2.3.1. Surface Morphology and Crystal Structure

The size, shape, chemistry and distribution of the nanoparticles were analysed by a scanning electron microscope (SEM, Prisma E, Thermo Fisher Scientific Inc.) equipped with an energy dispersive X-ray spectrometer (EDS) and operated at 15 kV. Micrographs at different magnifications were recorded by secondary emitted electrons and backscattered electrons. AuNP size distribution was formulated from the SEM micrographs using ImageJ software (https://imagej.nih.gov/ij). The morphology and crystal structure of the nanoparticles were assessed by a transmission electron microscope (TEM, JEM-2100, JEOL Inc.) operating at 200 kV. To avoid sample preparation artefacts, AuNPs were plasma-deposited directly onto the amorphous carbon grids, mounted in a double-tilt low-background holder, and transferred into the goniometer. Micrographs were recorded by a slow-scan CCD camera (Orius SC1000, Gatan Inc.).

2.3.2. Surface Chemistry Analysis and Optical Properties

Surface elemental composition and chemical bonding analysis were carried out on the material after deposition by X-ray photoelectron spectroscopy (XPS) using a PHI-TFA spectrometer (Physical Electronics Inc., Chanhassen, MN, USA) equipped with an Al-monochromatic X-ray source operating at an energy of 1486.6 eV. Diffuse reflectance spectra were collected using a Perkin Lambda UV-Vis device (model 1050) using an integrating sphere (inner diameter 15 cm). The selected resolution was 0.5 nm, and the range measured was from 500 nm to 750 nm.

2.3.3. Plasma Diagnostics

Analysis of gas-phase plasma was conducted by optical emission spectroscopy (OES). The spectrometer used for plasma species identification was a broad-range spectrometer, model LR1, from the company ASEQ Instruments, Vancouver Canada. Additionally, the spectra were used for gas temperature determination. For this purpose, a spectrometer with a higher resolution that records a range from 300 to 330 nm was used, also from ASEQ Instruments. Gas temperature was determined by comparing simulated and recorded optical spectrums of the OH radical rotational-vibrational band. Obtained temperature was OH rotational temperature, which can be assumed to be the gas temperature in this type of plasma. Simulation and comparison were conducted with computer software LIFBASE version 2.1 (https://www.sri.com/platform/lifbase-spectroscopy-tool/).

2.3.4. Surface-Enhanced Raman Scattering (SERS)

Water-diluted Rhodamine R6G with a concentration of 10^{-6} M was drop-casted onto the sensing substrate. The volume of liquid used was 1 µl. Raman fingerprints were collected using a confocal micro-Raman device (NT-MDT, model NTegra Spectra II) with a Peltier cooled CCD detecting unit. A laser wavelength of 633 nm was exposed to the analyte. Recording time for a single spectrum was 1 s and accumulated five times with a ×60 magnifying objective.

3. Results and Discussion

All the atmospheric pressure plasma-enabled gold deposition is performed at a constant time of 5 min at different plasma parameters. In the first case, plasma power is varied to understand its effect on gold deposition. The surface morphology of the obtained gold structures after 5 min deposition at various plasma power ranges is presented in **Fig. 1**. Three different power regimes are tested; namely high, medium and low, equal to 25 W, 18 W and 11 W, respectively.

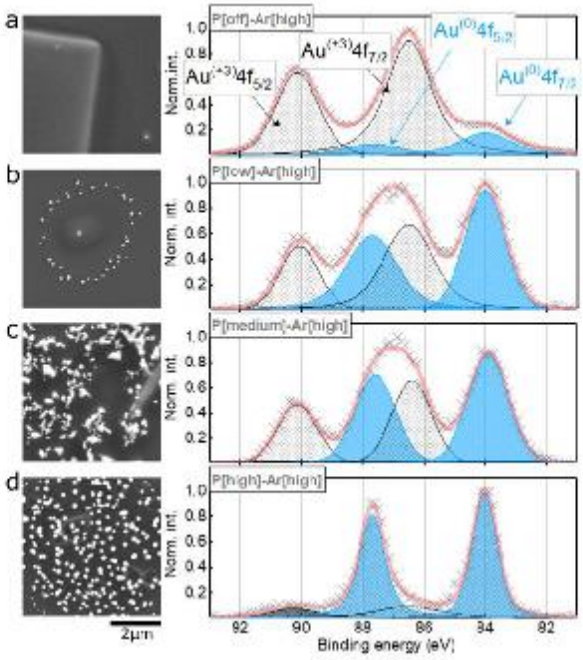

Fig. 1. (Left) SEM images displaying a general view of nanoparticle deposition on top of a silicon wafer at the highest Ar flow rate (2000 sccm) and different plasma power regimes: a – plasma off, b – low power (11 W), c – medium (17 W), d – high (25 W). (Right) Corresponding XPS fits reflecting an area interplay between the metallic and ionic contribution of $Au^{(0)}$ $4f_{5/2}$ and $Au^{(0)}$ $4f_{7/2}$ core levels.

SEM analysis confirms the formation of nanostructures at the substrate surfaces, and the influence of plasma power on the surface morphology. At low plasma power, nanoparticle deposition occurs in a very scattered manner, which indicates low nanoparticle reduction, also confirmed by XPS studies. With a 'medium' power, reduction is obviously improved. This is supported by a larger quantity of nanoparticles formed, lower chlorine content and enlarged area of both $Au^{(0)}$ $4f_{5/2}$ and $Au^{(0)}$ $4f_{7/2}$ core level shares. Particles are aggregated and reveal no dominant surface morphology. Reduction is improved significantly with the highest plasma power, as is visually confirmed by SEM and XPS results (**Fig. 1d**). From the SEM micrographs, noble metal nanoobjects are more separated and possess well-developed distorted spherical shapes. The approximate mean particle size created is ~100–150 nm. XPS core level peak deconvolution for this sample suggests the highest level of gold reduction from Au^{3+} state to Au^0. However, a portion of non-reduced gold Au^{+3} $4f_{5/2}$ and Au^{+3} $4f_{7/2}$ still do not vanish completely. Chlorine content given by XPS intensities is the smallest among all the samples.

In addition to the effect of plasma power for reducing $HAuCl_4$ aqueous solution, the effect of other parameters is also investigated. The role of different carrier and precursor gas flow rates is considered. Starting from the highest Ar flow at 2000 sccm, then reducing to 1500 sccm and finally finishing with 1000 sccm, a slight improvement in reduction efficiency is achieved. Mostly, this is caused by a smaller amount of precursor transported to the reaction site. This result is confirmed by lower XPS intensities of the high-resolution Au*4f* spectral region, where almost no sign of ionic contribution is found (1500 and 1000 sccm). The XPS core level chlorine Cl*2p* peak is the same level as the background. At 500 sccm flow rate, XPS detects no gold on the silicon wafer, so this case warrants no further consideration. It could be related to the fact that no vapours containing gold precursor are delivered to the plasma. Regarding the effect of Ar flow rate on particle size, general flow could lead to smaller particles, but the morphology remains similar. After careful analysis with SEM in **Fig. 2**., it is observed that the mean size of

particles reduces from ~150-200 nm down to ~100 nm, when the lowest and highest flow rates are compared. At the same time, the nanoparticle population on the silicon surface increases for the 1000 sccm Ar flow. The results of the medium flow fall between a range of extreme samples.

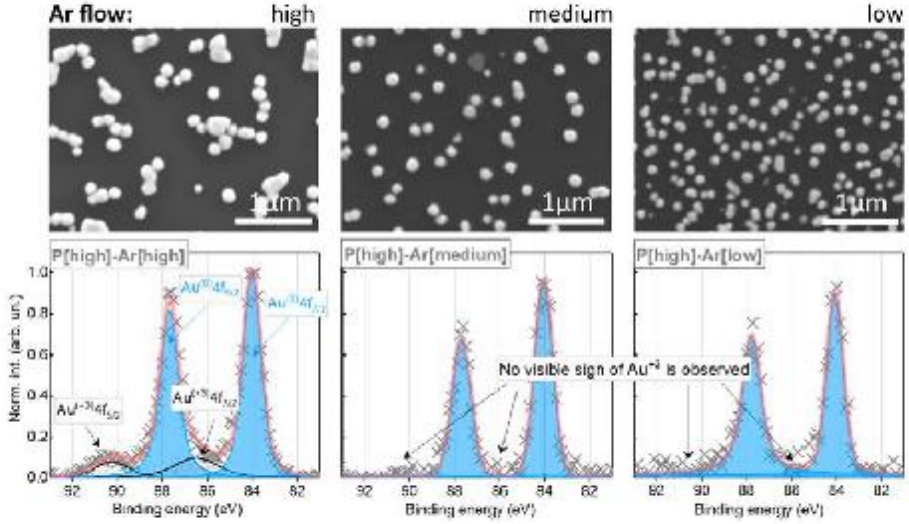

Fig. 2. (Top) SEM images of nanoparticles representing their size and distribution features under different Ar flow rates (high – 2000 sccm, medium – 1500 sccm, low – 1000 sccm). (Bottom) Corresponding peak deconvolution standing for ionic and metallic contribution into the Au*4f* region.

Based on XPS data obtained after deconvolution analysis, reduction efficiency can be presented via Au/Cl atomic ratio evaluation and monitoring of the diminishing feature occurring for the ionic share of Au^{+3} *4f* core level peaks. The reduction is already sufficient (**Fig. 3a**) at the highest plasma power (25 W) and medium-feeding gas flow rate (1500 sccm). Chlorine content in the samples located in the dashed red area is at the detection limit of the spectrometer. After optimum reduction is achieved, a closer look at the nanoparticle morphology is needed to understand nucleation and nanoparticle growth better.

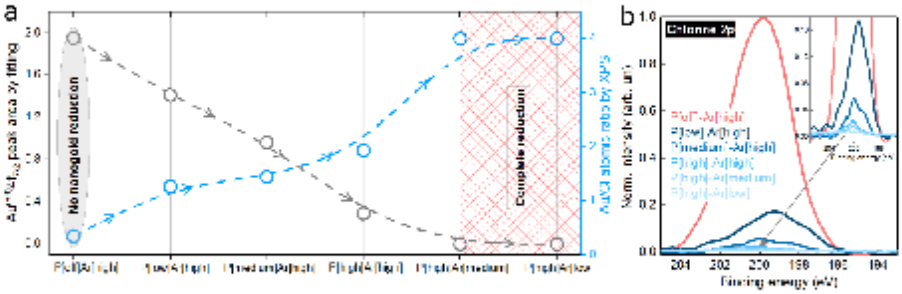

Fig. 3. (a) Reduction efficiency of $HAuCl_4$ to nanogold evaluated from XPS results based on an ionic contribution of Au^{3+} *4f* core level component (grey curve) and Au/Cl atomic content on the silicon surface. (b) High-resolution Cl *2p* peak representing intensity change with plasma power.

In order to understand the morphology of the AuNPs, TEM analysis is conducted. The AuNPs are directly deposited onto the TEM grid, and the micrographs reveal two significantly different size classes (**Fig. 4a**). The smaller nanodots have an average size up to 4 nm, with the majority being 1–2 nm and populating the majority of the carbon support film in a dense yet separated way (**Fig. 4a'**). The morphology of these particulates is irregular or spherical-like, and the crystal structure is free of internal defects. Accompanying AuNPs are larger and well-separated, with an average size of 40–50 nm. These can be divided into two groups. Irregularly shaped particulates appear subordinately and are distinguishable by a number of internal defects (**Fig. 4a"**). The other group differs by well-developed morphology and distinct Wulff shapes. Among them, we can distinguish single-crystal particles up to 20 nm in size, consisting of simple platonic shapes, predominantly the combination of octahedrons, cubes and their combinations, i.e. cuboctahedrons (**Fig. 4b**). The anisotropic 2D shapes result from one or more structural defects and are represented by thin trigonal and hexagonal shapes with 1 or more Σ3 twin boundaries (**Fig. 4c**); the same defect is also present in five-fold twinned AuNPs, resulting in well-known decahedral shapes (**Fig. 4d**). The morphology of the AuNPs is strongly affected

by internal structural defects and therefore determines their shape- and size-dependent physical and chemical properties.

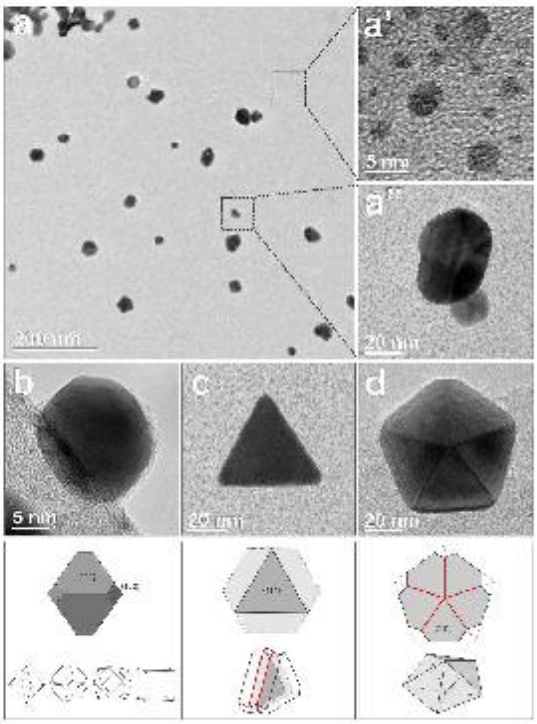

Fig. 4. (a) Low-magnification TEM micrograph of directly deposited AuNPs on an amorphous carbon grid, (a') densely populated by Au nanodots and (a'') irregularly shaped AuNPs. The well-developed particulates show forms of (b) irregular octahedrons, (c) triangular and hexagonal plates with single or multiple twinning boundaries, and (d) decahedrons with five-fold symmetry; the twinning boundary is marked with a red line.

Considering the changes in surface morphology and the reduction reaction along with plasma parameters, the changes that occur at different plasma parameters also play a critical role. Thus, plasma can be characterised by OES measurements. Optical emission spectra are populated with other excited species originating from Ar and He gases, environmentally present N and

NO ions, and positively/negatively charged radicals and ions. It should be noted that a relatively intense region contains OH bands (**Fig. 5a**). With a reduction of Ar flow, namely from 2000 to 1000 with an intermediate step of 1500 sccm, the excited lines of Ar are reduced (**Fig. 5b**). Still, their influence on OH radical formation is minor (**Fig. 5c**), the intensities of which remain similar. The difference occurs if discharge power is reduced, where reactive OH radicals and other species naturally lose their emission intensities (**Fig. 5d**).

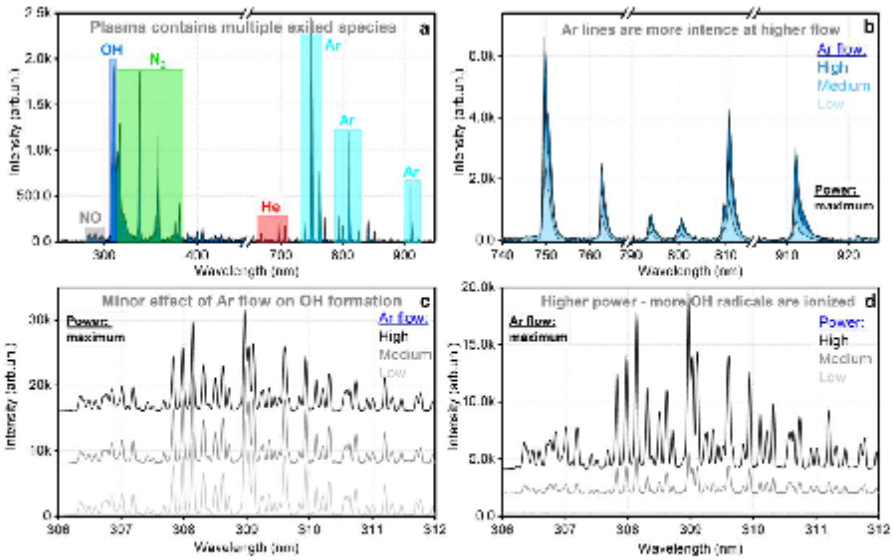

Fig. 5. (a) Optical emission spectra of plasma during deposition ($P = 25$ W) at fixed flow rates for He (290 sccm) and Ar (2000 sccm). (b) Zoomed Ar emission region indicates different peak intensities regarding feeding Ar gas flow rate; high – 2000 sccm, medium – 1500 sccm, low – 1000 sccm. He is kept at 290 sccm. (c) OH emission region at a different Ar flow rate. (d) OH emission region at different plasma power; high – 25 W, medium – 17 W, low – 11 W.

To approach the optimum reduction efficiency for nanogold formation, the interplay between plasma power and feeding gas flow rate is examined. Raw solution concentration is not of interest in the research conducted. At first, Ar flow rate gas is kept at its maximum (2000 sccm),

and plasma power is changed from its highest value accessible from the generator used down to a value where OH radicals can still be recognised from the background noise in OES. Thus, the OES spectrum is measured at three power regimes: low, medium and high, respectively. Additionally, a sample with no plasma involved is presented for comparison and to strengthen the understanding of nanoparticle formation on the silicon surface. After the same deposition time, the following can be observed.

If plasma is not ignited, no reduction is expected, which is confirmed by the large amount of gold in its ionic state in the raw precursor. SEM images reveal the presence of a micron-sized salt particle originating from a precursor (observation of AuNPs is a rare event in this case). Photoelectron spectroscopy reveals the presence of gold as two pairs of doublets signalling the contribution of different valance states, where an ionic contribution is dominant. A small portion of reduced gold (evident from XPS fittings) can be attributed to a minor effect of the beam during electron microscopy analysis. The largest amount of chlorine is a particular characteristic of this sample (**Fig. 3b**), the intensity of which is much more prominent compared to samples with ignited plasma, meaning no reduction is happening.

When plasma is ignited, the reduction starts immediately, even at the lowest power tested. The chlorine peak is reduced drastically, accompanied by the abrupt increase of gold in its metallic state (see blue areas in fittings). SEM signals reveal nanogold growth (bright particles in the image). However, a non-reduced salt is present at the surface in quite significant amounts indicating that a further power increment is required. Analysis of the optical emission spectra indicates that $HAuCl_4$ solution reduction could be caused by intermediate unstable, reactive H_2O_2 formation inside the plasma (**Fig. 5b**). The formation of H_2O_2 is mainly from the recombination of OH species, and the generated hydrogen peroxide may reduce Au^{3+} to Au^0. The reduction reaction could be represented as the following chemical process:

$$3H_2O_2 + 2AuCl \rightarrow 2Au^0 + 6H^+ + 3O_2 \quad (1)$$

In conventional chemical reduction techniques, the reduction of ionic gold Au(III) in $HAuCl_4$ towards its metallic state $Au^{(0)}$ involves multiple intermediate metastable states like Au(II) and $Au^{(I)}$, which cause time delays in the reduction process. Here, much faster processes occur, and AuNPs are feasibly synthesised by an APPJ introduced to an aerosol containing hydrogen tetrachloroaurate (III) hydrate ($HAuCl_4.xH_2O$). Therefore, a plasma-enabled reduction mechanism of gold particulates is proposed based on the findings from these characterisation studies. In the present APPJ system, plasma interactions occur between the inert gas (He, from the top, see **Fig. 6a**) and feeding gas Ar together with precursor microdroplets. The initiated gas-vapour interface interaction is responsible for the reduction and formation of nanoparticles. Following the known reaction kinetics and the obtained optical emission analysis, a qualitative description of the reduction and growth of AuNPs from the aqueous solution of $HAuCl_4$ by plasma can be provided. In the reduction process, free electrons (**Fig. 6b**) inside the plasma (e^-_{gas}), the H, OH radicals and hydrated electrons (e^-_{aq}) in the aerosol,[28][29] accompanied by the H_2O_2 formed inside the plasma drive the plasma-induced reduction process:

$$e^-_{gas} + H_2O \rightarrow OH\bullet + H- \quad \text{and} \quad 2\,OH\bullet \rightarrow H_2O_2 \quad (2)$$

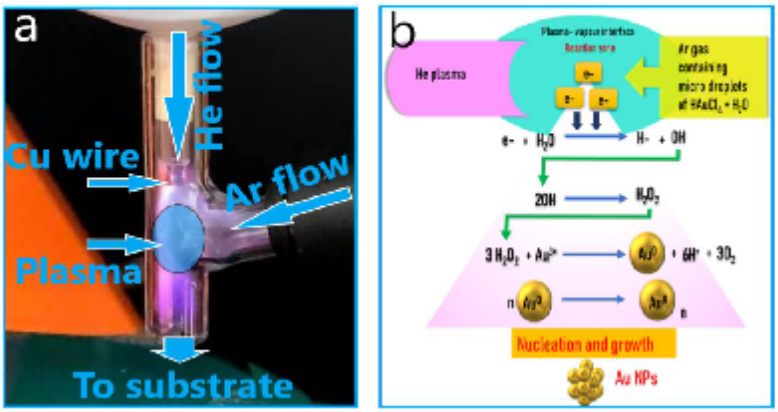

Fig. 6. (a) Experimental setup (with plasma ignited: ready-to-go regime, no precursor added) consisting of an APPJ operating on He gas and inlet for feed carried by Ar. (b) Schematic representation of plasma-vapour reduction mechanism driven by free electrons that initiate Au nucleation.

The OH radicals generated inside the plasma recombine to form H_2O_2, which reduces the metal salt to metallic nuclei that the following chemistry can support. Electron attachment dissociation occurs near the vapour/gas phase via free electrons from the plasma. H- ions are a byproduct and have very short lifetimes; nevertheless, they are also involved in a reduction process. The negatively charged hydrogen ions react with the water molecules quickly without participating in the reaction leading to the reduction of the metal salt. However, the OH radicals, which have a lifetime of nanoseconds, recombine and produce H_2O_2. The free electrons which are not participating in the dissociation of water molecules become hydrated and bound to water. These hydrated electrons can only produce OH^- and $H^\bullet$ in shorter nanosecond timescales. The hydroxide ions and hydrogen-free radicals follow the same reaction leading to the formation of H_2O_2, which could be the reduction agent of the metal salt. Surface and chemical composition analysis, along with plasma diagnostics, confirm the plasma-enabled reduction and deposition of gold structures in the form of nanoparticles.

Another strategically relevant question is the role of precursor solution. To investigate this, gold solution is prepared with water, alcohol and their mixture, and the effect of the presence of alcohol in the solution is assessed. To study the plasma power and gas flow rate effect, the solution is prepared only with deionised water. Here, aqueous solution is mixed with different concentrations of ethanol. Thus, five different concentrations of water-ethanol (W-E) solutions are prepared: W-E: 100-0, W-E: 75-25, W-E: 500-50, W-E: 25-75 and W-E: 0-100. In all cases, the concentration of the stock solution is kept fixed; the total amount of liquid is the same for the same salt quantity. Ethanol is more volatile than water and might affect the deposition efficiency considering the different chemistry, which might also be reflected in plasma characteristics. These two extreme cases are presented: He-Ar plasma with water and He-Ar plasma with absolute ethanol. The ionised gas states are analysed using OES spectra, and differ from each other, ascribed to the presence and behaviour of different reactive species. Considering the plasma ignites at atmospheric pressure, OES reveals that the presence of N, NO, O, He and Ar is common for all samples (**Fig. 7**). However, a noticeable difference is observed. After normalisation (N-related peak at 355.6 nm is used), it is observed that the most prominent features occur within the UV range, where the OH region is also observed (305–315 nm). It is less intense for ethanol-containing plasma by a factor of at least two. Visually, the ethanol-containing ignited plasma is also different, as the plasma jet is seen clearly up to the substrate surface, and a naked eye can monitor gold deposition. In fact, in the ethanol case, deposition seems to be a continuous film, but SEM analysis reveals a high level of porosity or spacing. This could be caused by the much higher volatility of alcohol compared to water, which leads to easier mass transport of gold precursor.

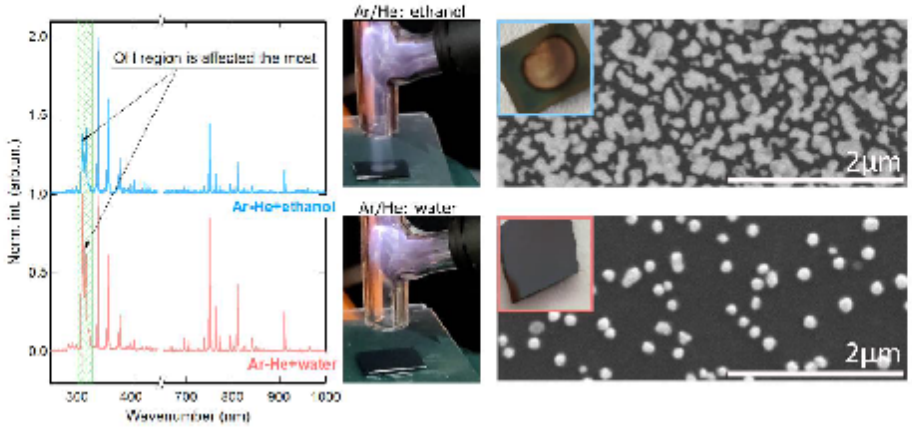

Fig. 7. OES spectra for plasma ignited with the addition of water (red) and ethanol (blue), accompanied by *in-situ* deposition photos of the system at corresponding regimes. SEM images reveal the surface state after 5 min of processing. Insets are digital photos of both substrates.

The intermediate concentrations where H_2O and C_2H_5OH are present do not differ significantly from the water sample, although particles are slightly smaller. However, if considering single particles from each sample (TEM analysis), the dominant geometry of nanoparticles is not changed; truncated crystals are still observed, as for deposition from water only. Particle size reduction might be related to the fact that gas temperature is reduced when alcohol is added (as seen from SEM). At first, the gas temperature is about 330 K with no liquid involved (Ar – 2000 sccm, He – 290 sccm). After the nebuliser introduces water vapour, the temperature almost doubles, reaching 620 K in the OH region. Then, step by step, the gas temperature drops to 580 K, 530 K and 500 K for samples W-E: 75-25, W-E: 50-50 and W-E: 25-75, respectively. It has to be mentioned that OH peak emission intensities are also lower when ethanol is involved in the precursor solution. Finally, no OH is detected for the pure ethanol sample, where a porous film is obtained after 5 min of deposition. It can be suggested that recombination processes and chemical reaction (salt reduction) rate are faster, and the technique used cannot monitor species

created in the particular OH spectral region. Smaller particle size, especially in the case of gold, is tightly connected to optical features related to the surface plasmon resonance (SPR) features [30]. Starting with a 'water' sample, a shift can be observed when alcohol is added up to 75%. The SPR blue shift is caused by a smaller particle size [31]. In the case of pure ethanol, a red shift occurs due to the coupling effect and dipole plasmon resonance (**Fig. 8**) [32].

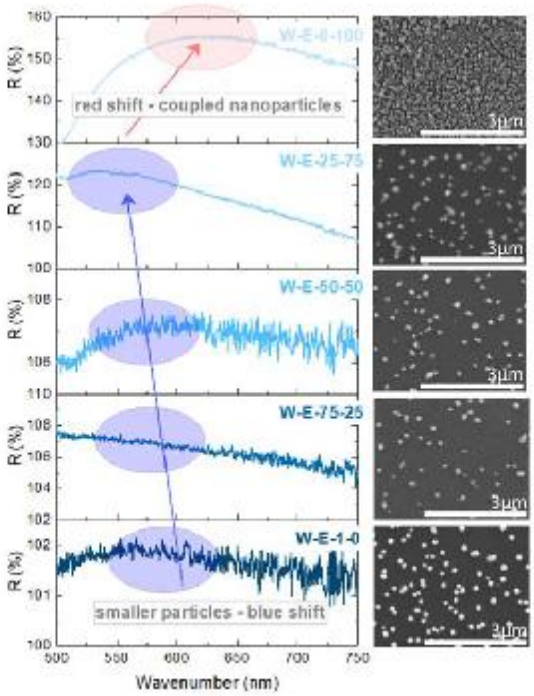

Fig. 8. Diffuse reflectance spectra of plasma deposited nanogold on top of the silicon substrate, accompanied with corresponding SEM surface guidelines. Note: untreated silicon is used as a background sample for DR spectra recording. Thus, all the reflectance is caused by nanoparticles.

Because of obvious plasmonic activity and the position of the resonance peaks caused by scattering and reflections, the samples W-E: 100-0 and W-E: 0-100 are tested regarding analytic

SERS capabilities. Similarly, two different nanometal-containing surface morphologies (separated particles and aggregated ones) that form a porous nanogold film are compared. A red laser (633 nm) is used to probe Raman spectra of Rhodamine R6G (water diluted 10^{-6} M) dye pipetted on top of the samples. The results presented in **Fig. 9** (olive curves stand for spectra of R6G collected from silicon) unanimously suggest that the nanoporous structure (blue curves) is significantly better than those composed of non-coupled nanogold (red curves). The intensity increments of the R6G peaks placed within a fingerprint region are at least 340% higher for the 'ethanol' sample compared to the 'water' one.

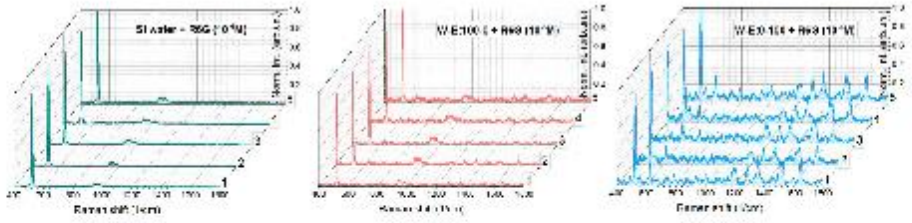

Fig. 9. Fingerprint SERS spectra of water diluted Rhodamine 6G dye (10 µl, 10^{-6} M) drop-casted on silicon (olive data), W-E: 100-0 (red data) and W-E: 0-100 (blue data) substrates.

The nanoporous substrate has an analytical enhancement factor ($AEF = \frac{I_{SERS} \times N_{Raman}}{N_{SERS} \times I_{Raman}} = \frac{I_{SERS} \times C_{Raman}}{C_{SERS} \times I_{Raman}}$), of about 10^7. The high efficiency of porous-like substrates regarding their ability to trace molecular spectra (Raman) of the various samples at nanovolume quantities is not surprising and was confirmed in recently published articles [33,34]. By controlling OH emission in plasma discharge and by solution volatility interplay, different nanogold materials can be synthesised and, more importantly, deposited on a different substrate in a single step. This highlights how the method can be of application for advanced nanoelectronics, especially the design of novel substrates (optical, plasmonic, catalytic).

4. Conclusion

The reduction of gold from hydrogen chloroauric acid was successfully accomplished by using an atmospheric pressure plasma jet operated with helium and argon as carrier gas. The effect of plasma power was investigated, leading to the conclusion that truncated geometry of nanoparticles can be obtained when plasma discharge is ignited at 25 W. Argon flow rate reduction from 2000 to 1000 sccm affects nanoparticle size, having virtually no effect on the morphology of the particles. A possible plasma reduction mechanism is discussed that could be related to the formation of hydrogen peroxide (H_2O_2) inside the plasma, facilitating the transition of gold from its ionic state toward metallic, thereby initiating nucleation and nanoparticle growth due to structural defect formation. Gas temperature reduction in the OH emission region was observed with the introduction of ethanol. This reduction was quite large, from nearly 630 K (water only, no ethanol) to 500 K (water-ethanol: 25%-75%), leading to nanoparticle size shrinkage and surface plasmon resonance blue-shift. For absolute ethanol, OH emission was not detected; however, increased liquid volatility improved mass transport of the raw precursor and porous nanogold film was obtained within 5 min of the deposition process. This particular substrate with the diffuse reflectance peak matching the laser wavelength (633 nm) revealed highly improved SERS properties due to strongly coupled nanoobjects that favour the generation of plasmonic media due to dipole plasmon resonance.

CRediT Authorship Statement

A. Vasudevan: Formal analysis and synthesis, Writing - original draft, Conceptualisation; **V. Shavlya**: Conceptualisation, Data curation, Formal analysis: XPS, UV-Vis, SERS, Writing - original draft, review and editing; **M. Kosicek**: Formal analysis – SEM, TEM; **J. Zavasnik**: Data curation, Formal analysis - TEM, Original draft-reviewing and editing; **A. Jurov:** Formal

analysis - OES; **N. M. Santhosh:** Data curation, Original draft-reviewing and editing; **A. Zidanšek:** Formal analysis, Validation, Original draft- reviewing and editing; **U. Cvelbar:** Conceptualisation, Data curation, Validation, Funding acquisition, Writing - original draft-reviewing and editing.

Acknowledgements

This work was performed under the project PEGASUS (Plasma Enabled and Graphene Allowed Synthesis of Unique Nano-structures), funded by the European Union's Horizon research and innovation program. Authors acknowledge the ARRS program no. P1-0417, project N2-0059, and NATO (Science for Peace and Security Programme), "Nanomaterials for Explosive Traces Detection with SERS" grant no. G5814. A.V. acknowledge the support of ADFUTURA (Public Scholarship, Development, Disability and Maintenance Fund of the Republic of Slovenia).

References

[1] K. Sahu, A. Bisht, S.A. Khan, A. Pandey, S. Mohapatra, Engineering of morphological, optical, structural, photocatalytic and catalytic properties of nanostructured CuO thin films fabricated by reactive DC magnetron sputtering, Ceram. Int. 46 (2020) 7499–7509. doi:10.1016/j.ceramint.2019.11.248.

[2] A. Zaleska-Medynska, M. Marchelek, M. Diak, E. Grabowska, Noble metal-based bimetallic nanoparticles: the effect of the structure on the optical, catalytic and photocatalytic properties, Adv. Colloid Interface Sci. 229 (2016) 80–107. doi:10.1016/j.cis.2015.12.008.

[3] S. Guo, J. Li, S. Dong, E. Wang, Three-Dimensional Pt-on-Au Bimetallic Dendritic Nanoparticle: One-Step, High-Yield Synthesis and Its Bifunctional Plasmonic and Catalytic Properties, J. Phys. Chem. C. 114 (2010) 15337–15342. doi:10.1021/jp104942d.

[4] B. Ankamwar, Biosynthesis of Gold Nanoparticles (Green-gold) Using Leaf Extract of

Terminalia Catappa, E-Journal Chem. 7 (2010) 1334–1339. doi:10.1155/2010/745120.

[5] A.J. Mieszawska, W.J.M. Mulder, Z.A. Fayad, D.P. Cormode, Multifunctional Gold Nanoparticles for Diagnosis and Therapy of Disease, Mol. Pharm. 10 (2013) 831–847. doi:10.1021/mp3005885.

[6] A. Oyelere, Gold nanoparticles: From nanomedicine to nanosensing, Nanotechnol. Sci. Appl. Volume 1 (2008) 45–66. doi:10.2147/NSA.S3707.

[7] S.A.C. Carabineiro, Applications of gold nanoparticles in nanomedicine: Recent advances in vaccines, Molecules. 22 (2017). doi:10.3390/molecules22050857.

[8] E. Boisselier, D. Astruc, Gold nanoparticles in nanomedicine: preparations, imaging, diagnostics, therapies and toxicity, Chem. Soc. Rev. 38 (2009) 1759–1782. doi:10.1039/b806051g.

[9] J. Turkevich, P.C. Stevenson, J. Hillier, A study of the nucleation and growth processes in the synthesis of colloidal gold, Discuss. Faraday Soc. 11 (1951) 55. doi:10.1039/df9511100055.

[10] M. Nakanishi, H. Takatani, Y. Kobayashi, F. Hori, R. Taniguchi, A. Iwase, R. Oshima, Characterization of binary gold/platinum nanoparticles prepared by sonochemistry technique, Appl. Surf. Sci. 241 (2005) 209–212. doi:10.1016/j.apsusc.2004.09.046.

[11] Yu, S.-S. Chang, C.-L. Lee, C.R.C. Wang, Gold Nanorods: Electrochemical Synthesis and Optical Properties, J. Phys. Chem. B. 101 (1997) 6661–6664. doi:10.1021/jp971656q.

[12] F. Porta, Gold nanostructured materials for the selective liquid phase catalytic oxidation, J. Mol. Catal. A Chem. 204–205 (2003) 553–559. doi:10.1016/S1381-1169(03)00338-8.

[13] R. Herizchi, E. Abbasi, M. Milani, A. Akbarzadeh, Current methods for synthesis of gold nanoparticles, Artif. Cells, Nanomedicine, Biotechnol. 44 (2016) 596–602. doi:10.3109/21691401.2014.971807.

[14] J. Turkevich, P.C. Stevenson, J. Hillier, A study of the nucleation and growth processes in

the synthesis of colloidal gold, Discuss. Faraday Soc. 11 (1951) 55. doi:10.1039/df9511100055.

[15] P. Zhao, N. Li, D. Astruc, State of the art in gold nanoparticle synthesis, Coord. Chem. Rev. 257 (2013) 638–665. doi:10.1016/j.ccr.2012.09.002.

[16] J. Kimling, M. Maier, B. Okenve, V. Kotaidis, H. Ballot, A. Plech, Turkevich Method for Gold Nanoparticle Synthesis Revisited, J. Phys. Chem. B. 110 (2006) 15700–15707. doi:10.1021/jp061667w.

[17] M. Brust, M. Walker, D. Bethell, D.J. Schiffrin, R. Whyman, Synthesis of thiol-derivatised gold nanoparticles in a two-phase Liquid–Liquid system, J. Chem. Soc., Chem. Commun. (1994) 801–802. doi:10.1039/C39940000801.

[18] C.-J. Huang, P.-H. Chiu, Y.-H. Wang, K.-L. Chen, J.-J. Linn, C.-F. Yang, Electrochemically Controlling the Size of Gold Nanoparticles, J. Electrochem. Soc. 153 (2006) D193. doi:10.1149/1.2358103.

[19] N.R. Jana, L. Gearheart, C.J. Murphy, Seeding growth for size control of 5-40 nm diameter gold nanoparticles, Langmuir. (2001). doi:10.1021/la0104323.

[20] K.X. Lee, K. Shameli, Y.P. Yew, S.-Y. Teow, H. Jahangirian, R. Rafiee-Moghaddam, T. Webster, Recent Developments in the Facile Bio-Synthesis of Gold Nanoparticles (AuNPs) and Their Biomedical Applications, Int. J. Nanomedicine. Volume 15 (2020) 275–300. doi:10.2147/IJN.S233789.

[21] T. Kaneko, K. Baba, R. Hatakeyama, Gas–liquid interfacial plasmas: basic properties and applications to nanomaterial synthesis, Plasma Phys. Control. Fusion. 51 (2009) 124011. doi:10.1088/0741-3335/51/12/124011.

[22] D. Mariotti, R.M. Sankaran, Microplasmas for nanomaterials synthesis, J. Phys. D. Appl. Phys. 43 (2010) 323001. doi:10.1088/0022-3727/43/32/323001.

[23] V. Amendola, S. Polizzi, M. Meneghetti, Laser Ablation Synthesis of Gold Nanoparticles

in Organic Solvents, J. Phys. Chem. B. 110 (2006) 7232–7237. doi:10.1021/jp0605092.

[24] J. McKenna, J. Patel, S. Mitra, N. Soin, V. Švrček, P. Maguire, D. Mariotti, Synthesis and surface engineering of nanomaterials by atmospheric-pressure microplasmas, Eur. Phys. J. Appl. Phys. 56 (2011) 24020. doi:10.1051/epjap/2011110203.

[25] P.J. Bruggeman, M.J. Kushner, B.R. Locke, J.G.E. Gardeniers, W.G. Graham, D.B. Graves, R.C.H.M. Hofman-Caris, D. Maric, J.P. Reid, E. Ceriani, D. Fernandez Rivas, J.E. Foster, S.C. Garrick, Y. Gorbanev, S. Hamaguchi, F. Iza, H. Jablonowski, E. Klimova, J. Kolb, F. Krcma, P. Lukes, Z. Machala, I. Marinov, D. Mariotti, S. Mededovic Thagard, D. Minakata, E.C. Neyts, J. Pawlat, Z.L. Petrovic, R. Pflieger, S. Reuter, D.C. Schram, S. Schröter, M. Shiraiwa, B. Tarabová, P.A. Tsai, J.R.R. Verlet, T. von Woedtke, K.R. Wilson, K. Yasui, G. Zvereva, Plasma–liquid interactions: a review and roadmap, Plasma Sources Sci. Technol. 25 (2016) 053002. doi:10.1088/0963-0252/25/5/053002.

[26] P. Maguire, D. Rutherford, M. Macias-Montero, C. Mahony, C. Kelsey, M. Tweedie, F. Pérez-Martin, H. McQuaid, D. Diver, D. Mariotti, Continuous In-Flight Synthesis for On-Demand Delivery of Ligand-Free Colloidal Gold Nanoparticles, Nano Lett. 17 (2017) 1336–1343. doi:10.1021/acs.nanolett.6b03440.

[27] J. Patel, L. Němcová, P. Maguire, W.G. Graham, D. Mariotti, Synthesis of surfactant-free electrostatically stabilized gold nanoparticles by plasma-induced liquid chemistry, Nanotechnology. 24 (2013) 245604. doi:10.1088/0957-4484/24/24/245604.

[28] J.J. Zou, Y.P. Zhang, C.J. Liu, Reduction of supported noble-metal ions using glow discharge plasma, Langmuir. (2006). doi:10.1021/la061795b.

[29] T. Kaneko, K. Baba, R. Hatakeyama, Gas-liquid interfacial plasmas: Basic properties and applications to nanomaterial synthesis, Plasma Phys. Control. Fusion. (2009). doi:10.1088/0741-3335/51/12/124011.

[30] C. Tira, D. Tira, T. Simon, S. Astilean, Finite-Difference Time-Domain (FDTD) design of

gold nanoparticle chains with specific surface plasmon resonance, J. Mol. Struct. 1072 (2014) 137–143. doi:10.1016/j.molstruc.2014.04.086.

[31] X. Huang, P.K. Jain, I.H. El-Sayed, M.A. El-Sayed, Plasmonic photothermal therapy (PPTT) using gold nanoparticles, Lasers Med. Sci. 23 (2008) 217–228. doi:10.1007/s10103-007-0470-x.

[32] S. Manivannan, R. Ramaraj, Assemblies of silicate sol–gel matrix encapsulated core/shell Au/Ag nanoparticles: interparticles surface plasmon coupling, J. Nanoparticle Res. 14 (2012) 961. doi:10.1007/s11051-012-0961-y.

[33] S.K. Srivastava, A. Shalabney, I. Khalaila, C. Grüner, B. Rauschenbach, I. Abdulhalim, SERS Biosensor Using Metallic Nano-Sculptured Thin Films for the Detection of Endocrine Disrupting Compound Biomarker Vitellogenin, Small. 10 (2014) 3579–3587. doi:10.1002/smll.201303218.

[34] N. M. Santhosh, V. Shvalya, M. Modic, N. Hojnik, J. Zavašnik, J. Olenik, M. Košiček, G. Filipič, I. Abdulhalim, U. Cvelbar, Label- Free Mycotoxin Raman Identification by High-Performing Plasmonic Vertical Carbon Nanostructures, Small. 17 (2021) 2103677. doi:10.1002/smll.202103677.

Highlights (for review)

Highlights

- Nanogold is obtained by the single-step plasma-jet redox reaction of ionic solution
- No additional reagent is involved in nanogold formation
- Nanoparticles are obtained from water, and the nanoporous film is printed from ethanol
- Nanoporous film reveals high SERS activity with the analytical enhancement factor ~ 10^7

Chapter 3

Deposition of Metal Oxide Nanoparticles Using Atmospheric Plasma Jets

Low-temperature atmospheric pressure plasma technologies offer the preparation of a variety of coatings and depositions, like in the previous chapter, with different chemical compositions, structures and morphologies. Fascinatingly, the progress in aerosol-assisted deposition process in which the precursor solutions or nanoparticle dispersions combined with plasma results in nice nanoparticle films. However, in the case of deposition transition metal oxides, the challenges are mainly the selection of the precursor solvent, the compatibility of the precursor with the plasma system, and the precursor's solubility in the solvent. From the previous research, we have concluded that water as a universal solvent can be a good precursor solvent and very compatible with the plasma system. Here the work has done in three transition metal oxides; insoluble (Nb_2O_5) and (RuO_2), and slightly soluble (V_2O_5) in an aqueous medium. This research reports the successful deposition of the particles, regardless of the solubility of the precursor material. Nevertheless, the atmospheric pressure plasma system is a successful candidate for the deposition of metal oxides. This chapter is a spin-off from chapter 1 and summarizes the research conducted so far on the deposition of metal oxides using the same atmospheric pressure plasma jet processing. A brief discussion on the outlook of future research is also included.

Regarding the contribution of the author: The author performed consecutive studies on the deposition of different metal oxides and a European patent on "Method for In-Situ Synthesis and Deposition of Metal Oxide Nanoparticles with Atmospheric Pressure Plasma" has been filed.

3.1 Introduction

Atmospheric pressure plasma jets allow the easy fabrication and modification of materials for a wide range of applications. The versatility of atmospheric pressure plasma processes is manipulating the chemical reactions in a way that is fast and simple, passing over the intermediate steps in the reactions. Synthesis of nanomaterials using atmospheric pressure plasmas also reduces the cost and maintenance because the process does not need any expensive vacuum equipment. However, the production of atmospheric pressure plasmas for material processing metal oxides is in a way tricky because of the unpredictability of atmospheric pressure plasmas with oxidation-reduction reactions, expressly for the transition metals. However, microplasmas offer a dial-up delivery of the precursors with favorable temperature conditions for the formation of nanoparticle formation.

Transition metal oxides (TMOs) are exceptional materials due to their electrical properties that have been known for decades, for a wide range of applications, for example, flat panel displays and energy storage applications etc. The transition metals in a brief are very accessible by defect engineering, doping, and quantum confinement creating high entropy oxides of the same with improved properties. Atmospheric pressure plasmas stand here for a feasible synthesis platform to tune the size, composition and defects over the transition metal nanoparticles [42][43].

Technically the plasma-assisted depositions are carried out using an aerosol containing either the metal oxide itself or a precursor solution for the same. The term aerosol refers to a mixture of liquid or solid particles suspended in a gaseous medium. The size of the suspended particles can be below 100 µm and the density below 1% [44]. However, since the metal oxide depositions are usually initiated from precursor solutions, here we mainly focus on aerosols formed by liquid droplets (by ultrasonic generation, pneumatic jets or electrostatic atomization). The droplet characteristics and distributions could vary according to the method of aerosol formation. By the use of a proper selection of precursors, metallic thin films and coatings can be deposited fast with high reproducibility and purity.

In this chapter, we are discussing plasma-assisted deposition of coatings, particularly vanadium pentoxide and niobium pentoxide coatings, which are two major transition metal oxides with a wide range of applications in the past few years. Properties of the materials and advantages and limitations of atmospheric pressure plasma-assisted depositions and outlooks are being briefly discussed.

3.2 Materials and Methods

All the materials used in this work were in laboratory grade and used without further purification.

3.2.1 Materials

All the chemicals used in this work were purchased from Alfa Aesar, ThermoFisher GmbH, Erlrnbachweg, Kandel, Germany: Niobium pentoxide (Nb_2O_5) - 99.9% metal basis, Vanadium pentoxide (V_2O_5) - 99.6% metal basis and Ruthenium oxide (RuO_2) - 99.95% metal basis (74% Ru).

3.2.2 Methods

3.2.2.1 Preparation of Feed Solution/Suspension

The precursor materials appeared as powders and were mixed with water (solvent). 0.01 g of the precursor was mixed with 10 mL of water to create a suspension or a solution according to the solubility of the metal oxide.

3.2.2.2 Deposition of Metal Oxide Nanoparticles Using Atmospheric Pressure Plasma Jet

4 mL of the feed solution/suspension is transferred to the nebulizer, which is connected to the APPJ. The nebulizer is supplied with constant Argon gas flow at a rate of 2300 sccm that can create constant nebulization and can carry the feed to the jet. The APPJ is ignited by an inert gas flow of Helium at a rate 290 sccm. The plasma combines with the feed inside a reaction tube of a diameter 8 mm. A silicon wafer substrate has been placed at the bottom of the get at a distance of 1 cm. A moving substrate holder has been installed and operated by software (Windows for PC), in order to ensure a uniform deposition over the substrate.

3.2.2.3 Characterization of Nanoparticles

The preliminary characterization to understand the deposition trends has been conducted.

a) SEM (Scanning Electron Microscopy): scanning electron microscope (SEM, Prisma E, Thermo Fisher Scientific Inc.) equipped with an energy dispersive X-ray spectrometer (EDS) and operated at 10 kV was used to observe the distribution, size and morphology of the particles deposited on silicon wafer substrate.
b) TEM (Transmission electron Microscopy): transmission electron microscope (TEM, JEM-2100, JEOL Inc.) was used to observe the crystallography of the particles deposited.

3.3 Results and Discussion

From the preliminary study of the depositions of above-described metal oxides, a short discussion is given below.

Since all the feed dispersions are made in distilled water and the solubility of the metal oxides in water considerably low, the depositions are different in their size, crystallinity

and the distribution on the substrate. RuO_2 and Nb_2O_5 are insoluble in water whereas the solubility of V_2O_5 slightly (0.7 g/L) in water. However, the deposition of the metal oxides using the APPJ was successful and could be studied intensively later on.

3.3.1 Depositions of RuO_2

Ruthenium (IV) oxide is the most common oxide of ruthenium and a conducting transition metal oxide which has unique electrochemical properties. It is widely used as an electro catalyst in the production of chlorine and oxygen. Since Ruthenium (IV) oxide (RuO_2) is insoluble in water, a dispersion of the same in water. The depositions were clustered. From the SEM micrographs, particle size is around 100-200 nm. The agglomeration is assumed to be because of the poor solubility of the metal oxide in water. From the TEM, there is no particular crystallinity can be found.

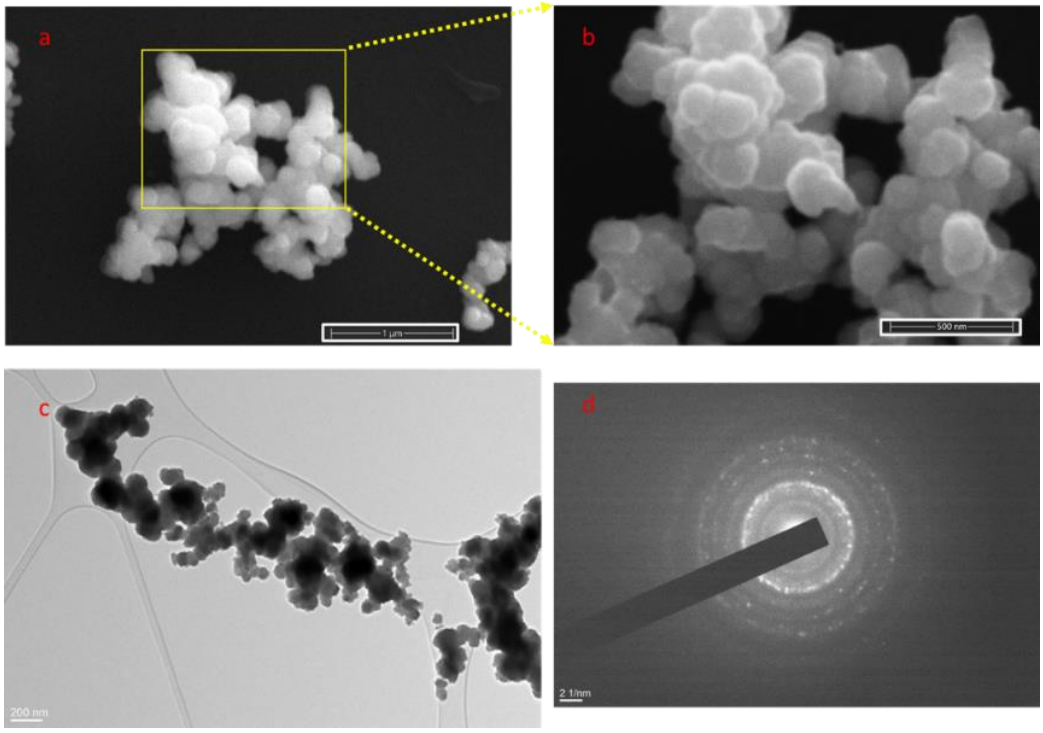

Figure 3.1: (a, b) SEM micrographs showing the deposition of RuO2 on silicon wafer substrate; (c) TEM micrographs of deposited RuO2 nanoparticles; (d) Diffraction patterns obtained from TEM showing the polycrystallinity of the particles.

3.3.2 Depositions of Nb_2O_5

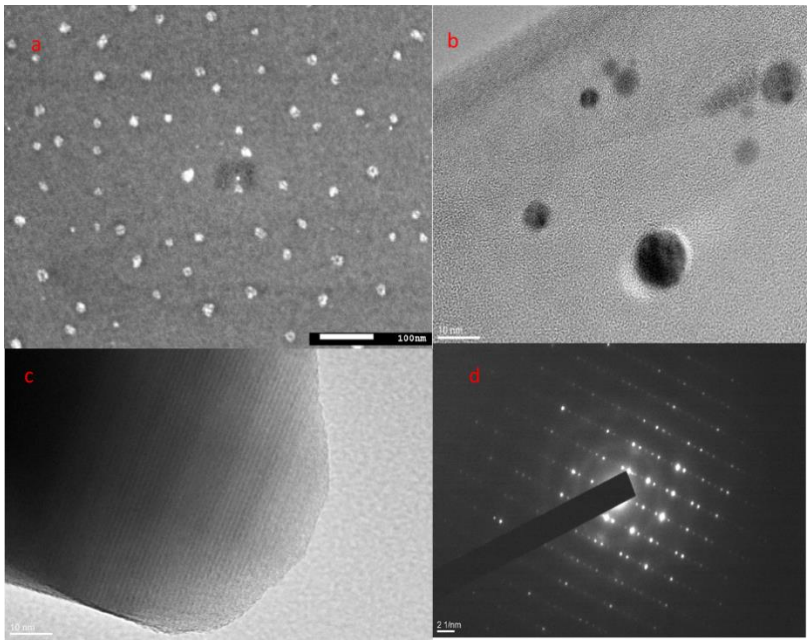

Figure 3.2: (a) SEM micrographs showing the deposition of Nb2O5 on silicon wafer substrate; (b, c) TEM micrographs of deposited Nb2O5 nanoparticles; (d) Diffraction patterns obtained from TEM showing the crystallinity of the particles.

Niobium (V) oxide (Nb_2O_5) is an insoluble, unreactive solid usually used as a precursor for materials containing niobium. The nanoparticles deposited on the silicon wafer substrate were uniformly deposited, and the size of the nanoparticles were around 10-20 nanometers. The particles are found to be single crystalline in nature from the diffraction patterns.

It is to be noted that even though the metal oxide is insoluble in water, the nanoparticles deposited on the substrate are well dispersed, and no agglomerated particles were found.

3.3.3 Depositions of V_2O_5

Vanadium pentoxide is slightly soluble in water (0.7 g/L (20 °C)) and particles deposited on the silicon wafer substrate is comparatively small and they have a narrow size distribution with diameters around 6 nm. Considering the slight solubility of the metal oxide in water, the deposited nanoparticles are well promising with very small particle diameter. It can be considered as a novel method for deposition of vanadium pentoxide nanoparticles with APPJs for various applications. The technology is reported (Appendix A) and applied for a patent at European Patent Office, which is under final evaluation.

Vanadium pentoxide is a promising candidate for coating materials and application of its optical activities and electronic properties, such as making laser crystals, decoration nanoparticles and in alloys and ceramics.

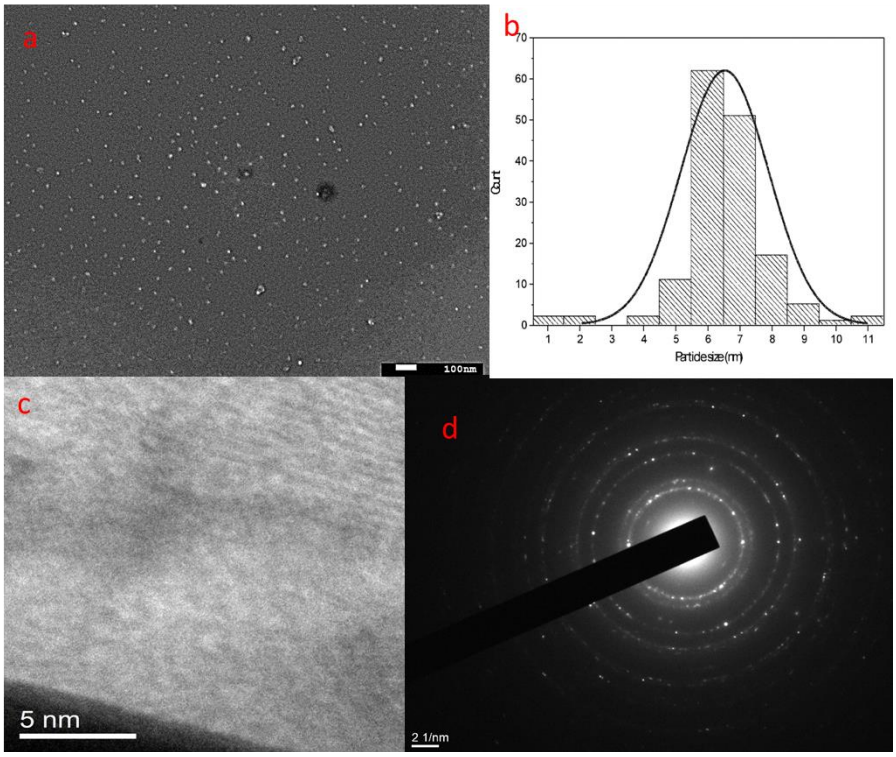

Figure 3.3: (a) SEM micrographs showing the deposition of V_2O_5 on silicon wafer substrate; (b) size distribution of V_2O_5 nanoparticles on Si wafer substrate; (c, d) TEM image and diffraction patterns obtained from TEM showing the crystallinity of the particles.

3.4 Conclusions and Future Works

The preliminary results from the depositions open up a possibility to print metal oxide nanoparticles from their bulk materials/powders. To keep the depositions less complicated, water is used as the solvent/dispersive medium. The size of the deposited particles can be affected by the solubility of the metal oxide in water. Fabrication of nanoparticles such as of stable vanadium pentoxide is very promising for future applications. Atmospheric pressure plasma jets are a reliable and compatible tool for the fast deposition of such nanomaterials directly to the substrate of choice. The work to achieve the goal is ongoing.

Chapter 4

Applications of Plasma-Generated Nanoparticles

The application of plasma-generated nanomaterials in various biomedical fields is a hot topic. Plasma-processed nanomaterials are a superior choice when it comes to purity as well as in material processing. In this chapter, we are conferring the application of specially designed plasma-processed nanomaterials in descriptive DNA studies. The gold nanoparticles fabricated by atmospheric pressure plasma jet possess highly efficient plasmonic arrangements, which can be used as a tool in sensing applications in the biomedical field. Here in, we present a DNA study using Surface-Enhanced Raman Spectroscopy using plasma-engineered nanoparticles as a tool. Following the strategy of single-step reduction of liquid water-diluted Hydrogen Chloroauric acid precursor by electron donation, the NPs formation was accelerated significantly and more importantly, without involving any chemical reducing agents. By applying plasma-vapor interaction technique, we synthesized Au nanoparticles and controllably deposited them on a flat Si substrate forming unique circular clusters with abundantly present NPs dimers and chains. The designed substrate hugely over performs Au-coated flat silicon substrate that helped improve the SERS chip's optical response and collect nicely resolved vibrational fingerprints of DNA fragments extracted from *E. coli*, *M. luteus*, *S. aureus* and *J. lividum* bacteria. Finally, using a spectral range, where four nucleotide bases reveal prominent separated Raman peaks and take a fundamental genomic ratio GC% as a key spectral difference, all DNA bacterial strains were successfully distinguished by SERS using PCA (principal component analysis) method.

Regarding the contribution of the author: The author of the dissertation has contributed to the synthesis part of the SERS substrate developed by atmospheric pressure plasma deposition.

(Article has been submitted to the journal Nano Letters)

Bacterial DNA Recognition by SERS Active Plasma-Coupled Nanogold

Vasyl Shvalya, Aswathy Vasudevan, Martina Modic, Mohammad Abutoama, Cene Skubic, Neje Nadlikar, Janez Zavašnik, Damjan Vengust, Aleksander Zidanšek, Ibrahim Abdulhalim, Damjana Rozman and Uroš Cvelbar**

Vasyl Shvalya - Department of Gaseous Electronics (F6), Jožef Stefan Institute, Jamova cesta 39, SI-1000 Ljubljana, Slovenia, EU.

Aswathy Vasudevan - Department of Gaseous Electronics (F6), Jožef Stefan Institute, Jamova cesta 39, SI-1000 Ljubljana, Slovenia, EU & Jozef Stefan International Postgraduate School, Jamova cesta 39, SI-1000 Ljubljana, Slovenia, EU.

Martina Modic - Department of Gaseous Electronics (F6), Jožef Stefan Institute, Jamova cesta 39, SI-1000 Ljubljana, Slovenia, EU.

Mohammad Abutoama - Department of Electrooptics and Photonics Engineering and the Ilse Katz Center for Nanoscale Science and Technology, School of Electrical and Computer Engineering, Ben-Gurion University of the Negev, Beer Sheba 84105, Israel.

Cene Skubic – Centre for Functional Genomics and Bio-Chips, Institute of Biochemistry and Molecular Genetics, Faculty of Medicine, University of Ljubljana, Zaloška 4. SI-1000 Ljubljana, Slovenia.

Neje Nadlikar – Centre for Functional Genomics and Bio-Chips, Institute of Biochemistry and Molecular Genetics, Faculty of Medicine, University of Ljubljana, Zaloška 4. SI-1000 Ljubljana, Slovenia.

Janez Zavašnik - Department of Gaseous Electronics (F6), Jožef Stefan Institute, Jamova cesta 39, SI-1000 Ljubljana, Slovenia, EU.

Damjan Vengust - Department of Gaseous Electronics (F6), Jožef Stefan Institute, Jamova cesta 39, SI-1000 Ljubljana, Slovenia, EU

Aleksander Zidanšek - Department of Gaseous Electronics (F6), Jožef Stefan Institute, Jamova cesta 39, SI-1000 Ljubljana, Slovenia, EU & Jozef Stefan International Postgraduate School, Jamova cesta 39, SI-1000 Ljubljana, Slovenia, EU.

Ibrahim Abdulhalim - Department of Electrooptics and Photonics Engineering and the Ilse Katz Center for Nanoscale Science and Technology, School of Electrical and Computer Engineering, Ben-Gurion University of the Negev, Beer Sheba 84105, Israel.

Damjana Rozman – Centre for Functional Genomics and Bio-Chips, Institute of Biochemistry and Molecular Genetics, Faculty of Medicine, University of Ljubljana, **Zaloška** 4. SI-1000 Ljubljana, Slovenia.

Uroš Cvelbar - Department of Gaseous Electronics (F6), Jožef Stefan Institute, Jamova cesta 39, SI-1000 Ljubljana, Slovenia, EU.

KEYWORDS. DNA genomic ratio, Plasma electrochemical reduction, coupled plasmonic nanogold, DNA Raman fingerprints.

ABSTRACT. Herein we describe how Surface-Enhanced Raman Spectroscopy (SERS) can be used to identify bacteria based on their genomic DNA composition and can thus serve as a

"sample-distinguishing marker". Successful spectral differentiation of bacterial species was accomplished with nanogold aggregates synthesised through single-step plasma reduction of the liquid noble-metal precursor. A high enhancement factor ($EF = 10^2$) in truncated coupled plasmonic particulates allowed SERS-probing at the nanograms sample quantities. The simulations confirmed the occurrence of strongest electric field confinement within nanometric gaps between Au dimers/chains, from where the molecular fingerprints of exemplary bacterial DNA-fragments gained the photon scattering enhancement. The most prominent Raman modes linked to fundamental base-pair molecular vibrations were deconvoluted, and data was used to proceed with nitrogenous base content evaluation. The genomic composition (percentage of GC and AT) was successfully validated by the third-generation sequencing using nanopore DNA sequencing technology, further proving that the SERS technique can be employed to swiftly specify bio-entities by the discriminative principal component statistical approach.

INTRODUCTION

Airborne and waterborne bacterial pathogens are abundant biological organisms worldwide, causing a destructive impact on human wellbeing.[1] Thus, there is a growing global need for medical, biological, pharmaceutical and food industries to develop novel analytical methods that provide in-depth differentiation of hazardous bio-entities and DNA characterisation.[2,3] Despite the comprehensive scientific effort put into this task, it is a significant challenge to find, tune and successfully exploit an approach that can be reliable for DNA fragments. Well-known spectroscopic tools, collectively known as surface-enhanced Raman spectroscopy (SERS) have already started being applied to the task, making the first experimental steps towards proving SERS' practical consistency when dealing with DNA structural investigations.[4,5] A key breakthrough has been incorporating nanoscale-sized noble metal crystals of various geometries

into the process.[6] And here is the reason why. Controlled attachment of metal nanoparticles on top of diverse substrates, including 2D/3D periodic and non-periodic structures, creates a perfect plasmonic medium to capture light and produce confined electromagnetic (EM) fields in hot-spot regions.[7] Under mutual resonant excitation at the metal-dielectric interface, the attached analyte's vibrational features are intensified significantly because of the enlarged Raman cross-section.[8,9] Depending on particle alignment and illumination conditions, the photon scattering efficiency within a plasmon-active area can be $>10^7$, enabling single-molecule Raman probing.[10]

Recently, the surface plasmon resonance (SPR) enhanced scattering has assisted in screening binding energy of single proteins, providing a piece of evidence that SPR phenomena could serve as a key factor for levelling-up bio-nanosensing devices.[11] Furthermore, by merging DNA engineering with nanoplasmonics, not only is accurate DNA detection possible,[12] but also SERS-identification of separated single nucleotides such as *adenine* (A), *guanine* (G), *cytosine* (C) and *thymine* (T).[13] However, when extracted DNA fragments are composed of nucleobases mixture (which happens most of the time), huge practical obstacles arise. Frequently the issue is related to insufficient plasmonic signal enhancement generated by commercially available Au or Ag nanocolloids. Additional difficulties can be attributed to non-homogeneous nanoparticle (NP) distribution over the surface, leading to problems with SERS hot-spot populations.

In this work, we aimed to solve this problem, designing a novel, highly efficient plasmonic arrangement to accomplish the discrimination of the bacterial DNA (Figure 1). Following the strategy of single-step reduction of liquid water-diluted hydrogen chloroauric acid precursor by electron donation, nanoparticles formation was accelerated significantly and more importantly, without involving any chemical reducing agents.[14] By applying the plasma–vapour interaction

technique,[15,16] we synthesised Au nanoparticles and controllably deposited them on a flat Si substrate, forming unique circular clusters with abundant NP dimers and chains.

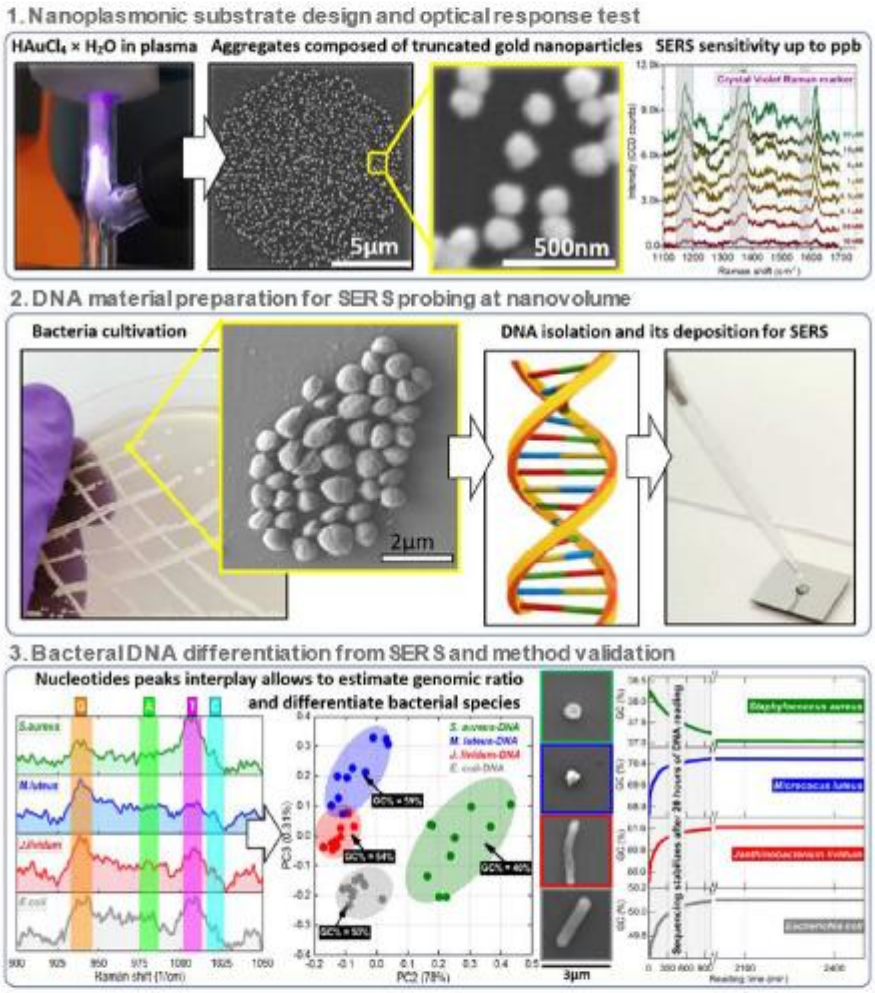

Figure. 1. Research methodology for SERS bacterial identification. Simplified scheme of the research steps. methodological investigation steps: (1) – Atmospheric pressure plasma-jet system operating on Ar/He gas mixture

was used for nanogold synthesis and their coupling on the silicon wafer, with followed substrate sensitivity test. (2) – Cultivation of bacterial strains, followed by DNA fragments isolation via extraction protocol (see supplementary) and preparing DNA as a liquid analyte in buffer solution for SERS; (3) - DNA samples were SERS measured, spectra were mathematically elaborated to be processed by principal components analysis PCA statistical approach. The genomic ratio of GC% versus AT was estimated from peak intensities, and the numbers obtained were compared to the long-read nanopore DNA sequencing method.

As observed, the designed substrate substantially overperforms Au-coated flat silicon substrates, helping improve the SERS chip's optical response to allow the collection of well-resolved vibrational fingerprints of DNA fragments extracted from *Escherichia coli, Janthinobacterium lividum*, *Micrococcus luteus* and *Staphylococcus aureus* bacteria. Utilising a spectral range where four nucleotide bases reveal prominent separated Raman peaks and take a fundamental genomic ratio GC% as a key spectral difference, all DNA bacterial strains were successfully SERS-distinguished by the principal component analysis (PCA) method. Finally, GC contents were validated by whole genome sequencing of the bacterial strains by the Oxford Nanopore technology. This work proves that the applied surface-enhanced Raman spectroscopy method has the potential to be successfully employed to specify bio-entities reliably by the discriminative prinsipal component statistical approach.

RESULTS AND DISCUSSION

Gold nanoaggregates designed by single-step plasma-assisted reduction. Plasma processing provides accelerated chemical reactions, allowing a nearly instant transformation of ionic Au(III) into metallic Au(0), and speeding up the metastable intermediate oxidation state reductions that occur during conventional wet chemical treatment without including any reducing activator.[14] In the current situation, noble metal precursor reduction occurs due to electron donation inside the

discharge of plasma, where the hydrated electrons (e^-_{aq}), and free (e^-_{gas}) together with H and OH active radicals act as electrochemical reducing factor.[17,18] The optical emission measurements collected in the progress of plasma discharge (Figure 2a) indicate the occurrence of reactive species, showing up a strong contribution of argon and helium excited lines (blue and violet boxes in Figure 1a). The obtained set of peaks placed between 320–450 nm are features linked to nitrogen lines appearing from the interaction of plasma with environmentally present nitrogen molecules. Highly reactive OH^- radicals found at 310 nm appear as a result of interaction between water diluted raw precursor, ambient air and ignited plasma. These active hydrogen-free radicals and hydroxide species recombine within the plasma discharge, creating highly oxidative H_2O_2 species, transforming the ionic metal with oxidation state Au(III) down to metallic state Au(0), which initiates nanocrystal growth from gold nuclei (Figure S1).

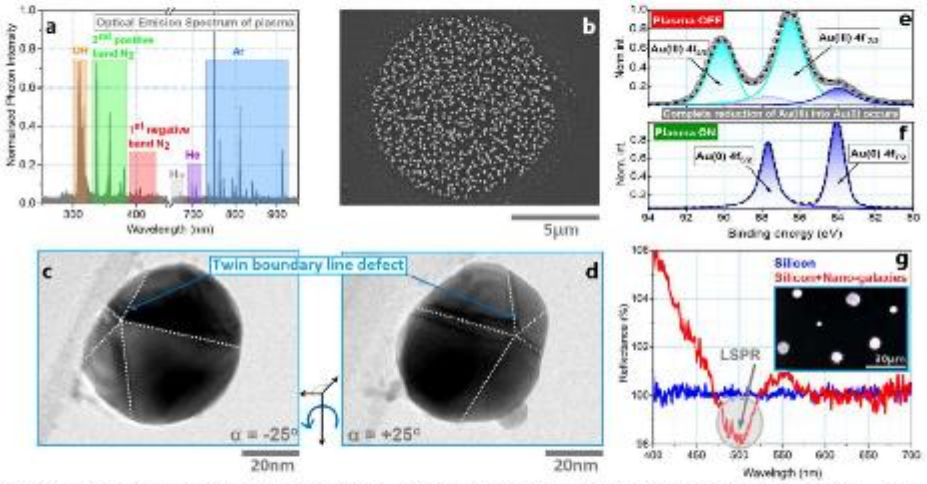

Figure 2. Synthesis of truncated nanogold aggregates. (a) Optical emission spectrum of the ignited plasma. (b) Backscattered electron-scanning electron microscopy (HR-SEM) micrographs of Au particles on top of the silicon wafer obtained after atmospheric pressure plasma jet treatment of the water-diluted hydrogen chloroauric acid precursor. (c–d) Transmission electron microscopy (TEM) micrograph pair, a part of the tilt-series used for

nanoparticle morphology reconstruction (α is tilt angle in *z*-axis. (e) X-ray photoelectron spectroscopy (XPS) spectrum of the dried raw precursor, revealing corresponding peaks for gold with ionic Au(III) (cyan areas) and metallic Au(0) (blue areas) core level contributions. (f) Au peak deconvolution obtained from XPS data after plasma-jet deposition. No ionic species are obtained. (g) Diffuse optical reflectance of the flat silicon taken as a reference (blue curve) and silicon with deposited nano-gold (red curve). The inset is an optical image of gold clusters over flat silicon taken in a dark-field configuration using a halogen bulb as a light source.

Consequently, micron-sized roundish aggregates consisting of coupled gold nanoparticulates are observed after a deposition procedure (Figure 2**b**). We argue that each circular Au aggregation is the end-product of precursor droplet reduction, and the following hypothesis explains the process involved. The aqueous solution of $HAuCl_4 \times H_2O$ possesses low volatility, and its droplets are of relatively large volume. Thus, during drop 'free-fall', nucleation is completed and grown gold nanocrystals gently land on the Si wafer. Once the solution's volatility is increased by adding ethanol with 1:1 volume ratio to water, as demonstrated by Hong *et al.*, then tinier particles are obtained that homogeneously cover the supporting Si substrate.[14] As observed from backscattered electron-scanning electron microscopy (BE-SEM) micrographs, larger/heavier metal particles are clustered tightly within a circularly shaped area. Their mean diameter varies in the range 10 ± 4 microns (Figure S2**a**). It was found that an average cluster's population is approximately 40 ± 5 within an area of about 0.1 mm^2. The rest of the Si substrate is decorated homogeneously by Au particles of a smaller size (<100 nm). (Figure S2**b,c**). Transmission electron microscopy (TEM) observations revealed that the nanoparticles are single-phase truncated gold nanocrystal dodecahedrons (Figure 2**c,d**) with distinct internal planar defects (five-fold twinning). For the selected nano-gold pattern (Figure 2**b**), a defined filling factor by nanoparticles is 0.178 (17.8%). The liquid precursor's reduction efficiency by plasma processing is quite high, as the amount of chlorine detected by energy-dispersive X-ray spectroscopy (EDS) is nearly negligible (Figure

S3a). No other contaminants are detected. The exact numbers of the elemental composition are collected in Table S1. No trace of chlorine on Si after plasma deposition is obtained from X-ray photoelectron spectroscopy (XPS) data either (Figure S3b). The opposite occurs for dried raw precursor material, a typical chlorine peak (Cl 2p) centred at about 199 eV is distinctly observed (Figure S3b). Deconvoluted high-resolution Au4f XPS peaks exhibit a dominant contribution of ionic Au(III) in dried precursor, while after reduction, nanoparticles reveal a metallic state of gold Au(0) (Figure 2e,f).

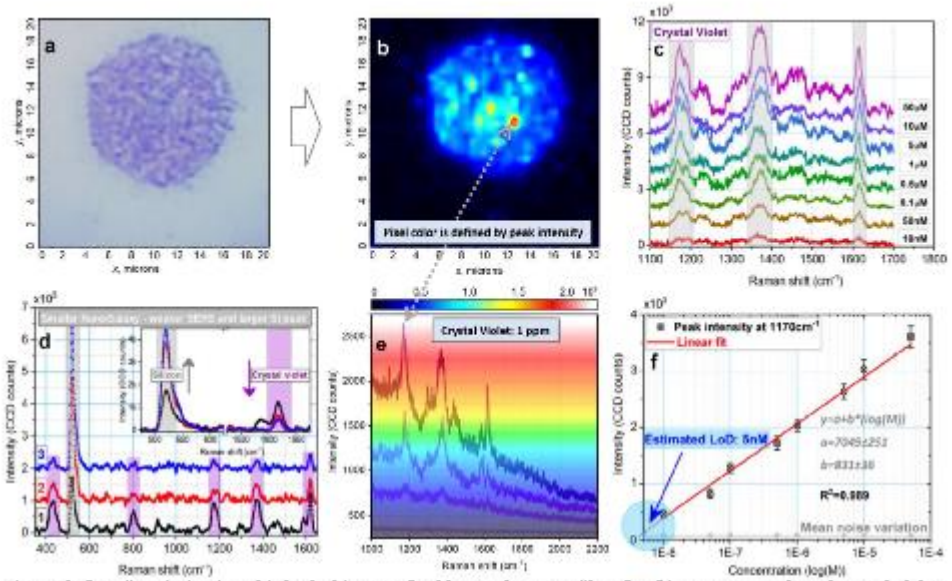

Figure 2. SERS optimisation. (a) Optical image of gold nanocluster on Si wafer. (b) Raman mapping of crystal violet (CV) deposited on gold decorated silicon. (c) Raman spectra of crystal violet aqueous solution in respect to the concentrations. (d) SERS of 1 ppm CV from different nanoclusters labelled as: '1' – *large*, '2' – *medium*, '3' – *small*. (e). Vibrational spectra of CV, where the intensity of a mode located at 1180 cm^{-1} defines a pixel colour in (b). (f) Raman intensity of the antisymmetric stretching ($CC_{sym}C$) band at different concentrations and its linear extrapolation.

Plasma-made nanogold is highly SERS-active. Following a procedure reported by Bossard-Giannesini and collaborators,[19] the surface plasmon resonance was investigated by collecting a diffusive component of the reflected light. Similarly to the reported investigations,[19] a derivative-like spectrum is obtained with a wide negative localised surface plasmon resonance (LSPR) peak centred around 500 nm and a shoulder rising at 550 nm (**Figure 2g**). It might be suggested that negative LSPR corresponds to absorbance and a small positive hump appears because of extinction from nanoparticles. Afterwards, the plasmonic properties of the designed surface were SERS-tested. At first, crystal violet (CV; 10^{-6} M) was deposited on the sensing substrate (**Figure 3a**), and Raman mapping was performed with a total number of 400 spectra acquired (**Figure 3a,b**)). The colour of each pixel corresponds to the intensity of the characteristic antisymmetric stretching $\nu_{as}(CC_{center}C)$ molecular mode located at 1180 cm^{-1}; shown by a coloured scale (**Figure 3b,e**). The other two main peaks in the presented spectra arise from the symmetric stretching vibration of the $(C\text{-}C)_{ring}$ at 1625 cm^{-1} and the bending motion of the $\delta(CH)/\delta_s(CH_3)/\delta(CCC)_{ring}$ band at 1391 cm^{-1}, which are well resolved as well.[20,21] Note that a contour of the enhanced signal coincides precisely with the cluster's real shape, indicating its enhanced optical response (**Figure 3a,b**). Furthermore, within the plasmonic area, signal intensity is locally increased by a few orders of magnitude. Although a higher Raman signal could be to a certain extent, related to increased concertation of colouring agent, we believe that it is far more likely a consequence of increased efficiency arising from enhanced plasmon coupling between two neighbouring gold nanoparticles. This SERS response within nanometric gaps is well understood and has been recorded numerous times.[22,23,24]

The analysis of micro-clusters of different sizes provided insight into the cumulative effect of Raman signal enhancement. Three types of circular aggregates were considered according to their

outer contour radii: large, medium and small, with an approximate diameter of 14, 8 and 2.5 μm, respectively (Figure S4). At first, ImageJ software was used to estimate the filling factor related to the number of nanoparticles placed inside. By counting all the nano-objects within a single cluster, the filling factor '*f*' slightly increases with area expansion according to the following trend *f* = 0.10 → 0.12 → 0.14. However, '*f*' never goes higher than 0.2. Then, a portion of Au dimers and chains were estimated. This was done by adjusting the ImageJ circularity filter from 0–1, relying on nanoparticle geometrical likeliness to a perfect circle. As it gets close to 1, particles deviating from an ideal circle and mostly aggregates can thus be distinguished analytically. By setting a circularity filter from 0.1–1 (Figure S4**a1,c1**), almost all nano-objects are counted. In contrast, once the filter was set within the range 0.85–1 the agglomerates composed of even just two gold nano-objects can be clearly pinpointed (Figure S4**a2,c2**). Regardless of the type of cluster, the amount of such agglomerates is about 30–40%. Thus, it could be believed that the bigger cluster would provide higher cumulative signal enhancement due to having a larger number of hot-spots. These three clusters are SERS-compared below.

Crystal violet molecular marker was drop-casted onto the plasmonic surface, dried and measured with Raman spectroscopy (Figure 3**d**). The first thing to notice is how the Raman peak associated with crystalline Si (521 cm^{-1}) increases with Au cluster diameter shrinkage. This is expected because the scattering laser spot covers a larger surface area than just with silicon. This peak is particularly intense for *small* nano-gold clusters whose diameter is 2.6 μm (Figure 3**d** *inset*).

On the other hand, photon scattering intensity corresponding to the model dye CV rises when the cluster area becomes larger. Taking a peak of CV located at 1620 cm^{-1} as a reference and considering an optical response of a *large* cluster as 100%, the *medium* cluster reveals 1.9× and *small* Au aggregates 2.7× intensity reduction.

To probe the limit of sensitivity of a large cluster, a set of different ethanol-diluted dye concentrations were SERS-probed. The photon scattering intensity of the main Raman modes enclosed in 'grey boxes' (Figure 3c) decreases with lower concentrations. Spectra are, however, still well-resolved at minimum concentrations equal to 10 nM. A semilogarithmic plot of 'signal intensity vs concentration' (Figure 3f) follows a linear trend, where it can be observed that a minimum concentration of about 5 nM would still probably be resolved out of the noise spectrum. The enhancement factor (EF) is estimated to be as high as $\sim 10^7$, indicating the excellent detection abilities of the substrate.

Ultrahigh field enhancement favours accurate SERS recording of DNA. Simulations confirm the occurrence of electric field hot-spots in nanometric gaps. In attempts to quantify the enhancement of the SERS signal by the structure that consists of nano-objects and their aggregates on Si substrate, EM field distribution (FD) simulation was performed using COMSOL Multiphysics software (Figure 4a-b). The aim was to monitor the FD of a selected area within a cluster (1 μm^2) because it contains single Au nano-objects of about 150 nm in size as well as their geometrical interplays such as dimers and chains (Figure 4c). Due to many NPs forming the cluster, simulating the FD within the whole structure would require huge computation time and resources. Considering that synthesised particles are neither spherical nor ideal truncated bipyramids, it was decided to elaborate on two extreme boundary cases: ideal spherical and five-edged bipyramid geometries (Figure S5). Thus, a real scenario could naturally be expected to fall between the modelled results. The important evidence coming from Figure 4a is that the largest field enhancement (FE) exists within the nanometric gaps between the NPs forming the dimers and chains. In contrast, much smaller enhancement is observed around single nano-objects, supporting the significance of close-packing NPs. Additionally, the influence of the distorted NP

geometry accompanied by sharp edges (Figure 4b) also favours EM enhancement. As follows from calculations (Figure 4a-b), the field intensity is greater at least by a factor of ~2 in the case of bipyramids compared to spheres due to the stronger field confinement effect near the tips (see supplementary description related to Figure S6, S7).

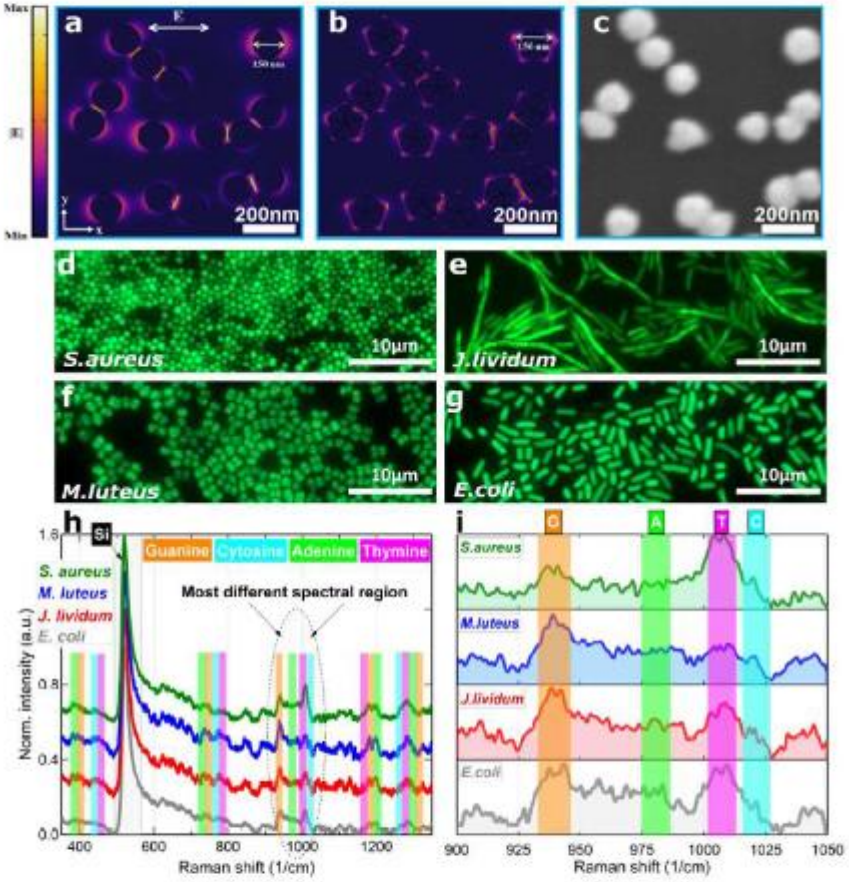

Figure 4. Electric field confinement ensures reliable bacterial DNA sensing. (a) FD simulations inside the unit cell of the considered periodic structure with spherical particles. (b) The same FD simulation for distorted five-edged-like bipyramids. Remarks: λ = 633 nm, normal incidence and TE polarisation were used to simulate the gold NPs on a silicon substrate. Air was assumed to exist between the NPs and the superstrate material. For a more quantitative

estimation of the field, see the supplementary information. (c) SEM image of an Au NP cluster selected for real-case scenario Maxwell EM field modelling. (d-g) Microscope images of cultivated bacterial species. (h) SERS spectra of extracted bacterial DNA in the fingerprint region. (i) Enlarged part of the long-range spectra highlighting the most prominent vibrational differences in gaseous content-sensitive region.

Next, DNA fragments were extracted from four exemplary bacterial species. Pair of spherically shaped (*S. aureus, M. luteus*) and rod-like looking bacteria (*J. lividum, E. coli*) (Figure 4**d-g**). Following a protocol (see supplementary), the DNA material was prepared in buffer solution, drop-casted on the substrate, dried under ambient conditions and then SERS measurements were conducted (Figure 4**h-i**). A sign of the successfully deposited analyte on the sensing surface can be confirmed by interference lines observed from an optical image captured in a bright-field regime and scattering lines in dark-field mode. (Figure S8). Ten vibrational spectra for each macromolecular DNA complex were accumulated and elaborated mathematically, applying baseline subtraction, smoothing function, and data normalisation (Figure S9). Within Figure 4**h**, the strongest peak placed at 521 cm^{-1} is assigned to the Si transverse optic vibrational phonon mode araising from the substrate. At the same time, the rest of the spectral interval is populated with Raman signals originating from bacterial DNA that covers Au nanoaggregates. Despite being quite similar in shape at first look, the spectra reveal noticeable dissimilarities across the measured range. Following the pioneering vibrational research conducted by Otto *et al.*,[25] the Raman peaks of the main nucleotide bases (*guanine* 'G', *cytosine* 'C', *thymine* 'T' and *adenine* 'A') were marked according to their locations across the spectra. Typically, a mixture of different nucleotides is associated with plenty of vibrational modes, frequently overlapping each other within the fingerprint region. However, two spectral intervals, namely 350–450 cm^{-1} and 875–1075 cm^{-1}, might be used to indicate the presence of all four nucleotides. In the low-frequency range (350–450 cm^{-1}), below 400 cm^{-1}, spectra are dominated by the ring bending vibrations of the structurally

larger complexes consisting of two aromatic rings (G and A). Similar vibrational features of the nucleotide's bases possessing one structural ring (C and T) are shifted towards higher frequencies and located just above 400 cm^{-1}.

Characteristic genomic content is a key factor for DNA distinguishing. Nevertheless, more distinct information is hidden in the spectral region 875–1075 cm^{-1} (Figure 4i). Here, peaks are sharper, more intense and well separated. Referring to Otto *et al.* research,[25] the prominent Raman mode at 940 cm^{-1} originates from **'G'** structure and the peak located near 1008 cm^{-1} is attributed to **'T'** nucleic base. It is worth mentioning an evident high-wavenumber shouldering **of 'T' mode** due to a peak at 1021 cm^{-1} caused by a combined contribution of $NH_2^{rocking}$ + $C_6H^{bending}$ vibrations in **'C'** molecular structure of bacterial DNA.[25] **Raman features of 'A' cannot be resolved clearly in this range (between 'G' and 'T' horns) due to a more complex mutual interaction with other** structural modes vibrations of similar intensity, FWHM and area (see fitting data and table in supplementary) (Figure 5a). Above mentioned findings**, especially 'G' and 'T' related Raman** peaks intensity ratio interplay, were taken as key spectral features to run a PCA (principal component analysis). The PCA tends to classify the spectra by creating separated data clusters with common features reflected in a loading plot. (Figure 5c-d). From these two graphs, a general remark rises: PC1 vs PC2 combination, which is typically sufficient for separating two groups of samples, in our case, is not applicable to classify four different sets of bacterial DNA. A combination of higher principal components is required for adequate sample distinguishing. The graph composed of **'PC2 (abscisc)' vs 'PC3 (ordinate)** ((Figure 5d))' contains four colored data clouds, each including ten spectra (one dot – one spectrum) correlated to a particular bacterial DNA sample. A detailed description of dimensionality-reduction data processing with related figures (Figure S10-12) is kept in supplementary.

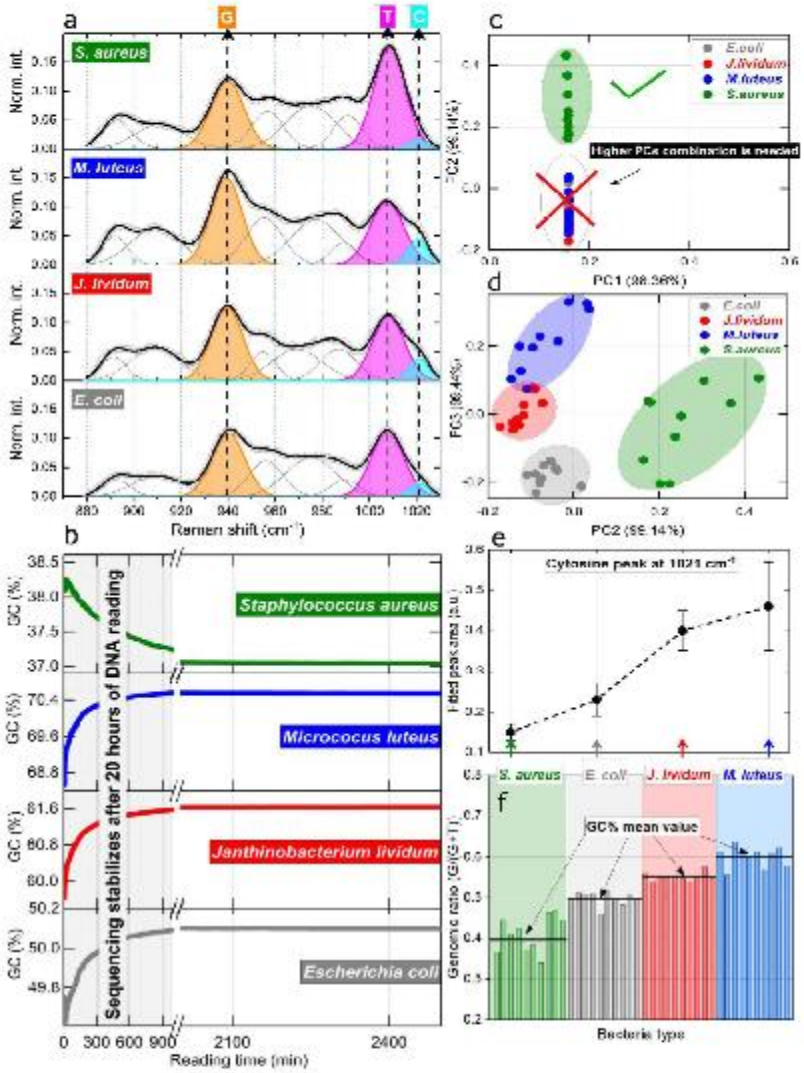

Figure 5. Distinguishing DNA by genomic content and data verification by DNA sequencing method. (a) SERS data with Gaussian fittings of the nucleotide modes in a specified spectral interval. (b) Sequencing technique with *in-situ* GC nucleotide content during DNA nanopore reading of each bacterial DNA. **(c,d) SERS PCA with clustered spectral data. (e) The fitted area of SERS measured 'C' peak at 1021** cm^{-1} (f) Calculated genomic ratio of bacterial DNA using peaks intensity SERS data with indicated mean values a certain DNA type.

The most reasonable question to ask here is subsequent. Is there any relation between a fundamental genomic ratio GC% (G, C) of bacterial DNA and the Raman intensities of certain peaks within this range? To better understand the PCA results, these three characteristic peaks deconvoluted with Gaussian function were analysed regarding their intensity. From the Gaussian fittings (Figure 5a), it can be observed that for *E. coli*, the intensities of 'T' and 'G' are nearly the same. The relevant fitting information (area, full-width at half-maximum (FWHM), position) of characteristic SERS modes elaborated in Figure 5a are listed in Tables S2–S4. For *S. aureus*, the 'G' peak is much smaller than 'T', while the opposite occurs for *M. luteus* DNA. In the case of *J. lividum*, the 'G' mode slightly overpowers the 'T' peak.

The observed peak intensities behaviour correlates with DNA GC% content of measured bacterial species. To visualise the occurring situation better, the following procedure was conducted. **Considering that 'G' always** pairs **with 'C' and 'T' is structurally connected to 'A', the** experimental genomic ratio might be estimated via a typical relation (G/G+T), focusing on peak intensities. The (G/G+T) contents calculated for all DNA spectra are depicted (Figure 5f), where a step-like behaviour of mean values (black horizontal line) increases in accordance with literature given data of GC% content, following a natural sequence *S. aureus* > *E. coli* > *J. lividum* > *M. luteus*. According to the available database, the average GC% value for bacterial DNA tested within a report should fall within a range of *M. luteus* = *69 ± 4 %*, *J. lividum* = *61 ± 4 %*, *E. coli* = *50 ± 6 %*, and *S. aureus* = *39 ± 4 %* (see supplementary). However, the bacterial genome GC content may vary substantially by the number of cell divisions; thus, the whole genome sequencing of bacterial strains was conducted, applying the long reads offered by Oxford Nanopore technology (Figure 5b). At the beginning of the DNA reading, an error is the largest, reaching up to 5%, and after approximately 20 hours of non-stop sequencing, a graph shows that a stable,

precise, saturated value was obtained and the final numbers for a genomic content are given: *M. luteus* = 70 ± 2%, *J. lividum* = 61 ± 2%, *E. coli* = 50 ± 2%, and *S. aureus* = 37 ± 2%. In turn, the nucleotide contents obtained from SERS measurements followed by (G/G+T) expression are as follows: *M. luteus* = 59 ± 5%, *J. lividum* = 54 ± 4%, *E. coli* = 50 ± 3%, and *S. aureus* = 40 ± 6%. **Interestingly, a contribution of the shouldering 'C' peak** at 1021 cm^{-1} follows the logic of the (G/G+T) ratio as well as GC%: its area/intensity is the smallest for *S. aureus* and the largest is found for *M. luteus* bacterial DNA (**Figure 5e**). It further validates the reliability of Raman nanospectroscopy for DNA genomic study. A larger uncertainty in SERS results might be related to the following reasons; (i) smaller sample quantity compared to the amount requested for sequencing and (ii) purity of the examined sample in SERS analysis (additional purification step is required for Nanopore Technology to prevent blocking of protein pores).

***Table 1.** A general comparison between the Nanopore sequencing and SERS technologies in the bioanalysis area.*

Crucial Metrics	**Methods**	
	Sequencing	**SERS**
Sensitivity (amount of sample used)	200 ng	100 ng
Steps before data collection	1 – Bacteria cultivation 2 – DNA extraction 3 – Purification of DNA 4 – Preparation of libraries 5 – Genome reading 6 – DNA fragments assembling 7 – Bioinformatics analysis	1 – Bacteria cultivation 2 – DNA extraction 3 – Spectra recording 4 – PCA analysis
Selectivity	Very high	High
Analysis time	Hours – Days	Seconds – Minutes
Overall analysis cost	High	Low
Scale and area of application	*Molecular level:* DNA/RNA *Other molecules:* --------Not applicable-------- *Cellular level* --------Not applicable--------	*Molecular level:* DNA/RNA *Other molecules:* lipids, proteins, sugars - YES *Cellular level* Bacteria, viruses, fungi – YES
Type of data	DNA composition sensitive – YES DNA topology sensitive – NO	DNA composition sensitive – YES DNA topology sensitive –YES

Even though the final genomic content obtained from sequencing technology might deviate to a certain extent from those estimated from SERS measurements, it can be suggested that the nanoRaman technique possesses a strong analytical potential for compositional/structural investigations of biological materials at molecular and cellular levels (Table 1). Also, despite pointing to a proof-of-concept, there is still room for the method improvement in a presented challenge. In particular, increasing selectivity (reducing error, validation of DNA SERS markers) might be addressed via elaborating on sample, purity, diversity and quantity, varying the exposure time/power, and targeting an even better plasmonic match between a sensing substrate and incident laser beam.

CONCLUSIONS

In conclusion, it can be stated that an accurate distinctive vibrational analysis of bacterial DNA is possible with advanced nanoplasmonics. Prepared, characterised, and verified in the research, SERS-active micron-scale aggregates composed of truncated nano-gold particulates, obtained by a plasma–driven instant reduction mechanism, can serve for SERS probing of biological macromolecules at nanograms sample quantities (100 ± 10 ng/μl). Involving no external reducing agent, the plasma processing accelerated the formation of multiple nanogold dimers and chains particulates. Verified by field distribution modelling, the plasmonic substrate achieves a strong electromagnetic confinement effect with an experimentally proven enhancement factor as high as ~10^7. The outstanding analytical performance of the substrate assisted in fast collecting (5 sec for a single spectrum) and, more importantly, for the first time, specifying the vibrational fingerprints of DNA fragments extracted from common bacterial species (*Escherichia coli*, *Janthinobacterium lividum*, *Micrococcus luteus* and *Staphylococcus aureus*) by multivariate

statistical PCA analysis, linking the results to genomic content ratio. This was estimated from both Raman and low-error long-reading sequencing techniques. At last, SERS is highly sensitive to the DNA environment and offers a faster, more facile complementary pathway that enables obtaining primary data on GC% or distinguishing between DNA by operating at smaller sample quantities and allowing to skip an additional DNA purification step, which is required for the Nanopore DNA sequencing technique.

ASSOCIATED CONTENT

Supporting Information

Synthesis of nano-gold. Crystalline tetrachloroaurate (III) hydrate ($HAuCl_4 \times H_2O$) (99.9% metal basis, Au 49% min) was used as the raw precursor purchased from Alfa Aesar by Thermo Fisher (Kandel) GmbH, Germany. The material was weighed at the amount of 0.01 g and dissolved in 10 ml of distilled water to make the feed solution, which was heated at 60 °C for 30 min using magnetic stirring. The solution was kept aside to cool down to room temperature. After, 4 ml of the preheated solution was transferred to the nebuliser in tube contact with the atmospheric pressure plasma jet system. The experimental setup comprised two vertically aligned quartz tubes of inner diameter 3 mm and 7 mm, where the larger one was an actual plasma chamber. The smaller tube was also of a shorter length. A gold-coated copper wire was inserted, whose free tip acted as a plasma ignition point. The main inlet gas was helium flowed at a rate of 290 sccm. The He plasma was ignited at a power of 25 W operated at a frequency of 21.2 kHz. A heavier argon carrier agent was connected to a nebuliser containing a liquid precursor solution $HAuCl_4 \times H_2O$. Gas Ar with a much higher flow rate set as 1000 sccm fetched vaped precursor microdroplets, bringing them into contact with the generated plasma. Note that no grounding was applied to the Si wafer. The substrate of approximate area 1 cm^2 was fixed on a moving stage motor operated by WinPC-NC software. Uniform distribution over the substrate was achieved by moving the sample stage in a zig-zag manner for 30 min. The nebuliser was constantly supplying the precursor at the rate of 1000 ml/min.

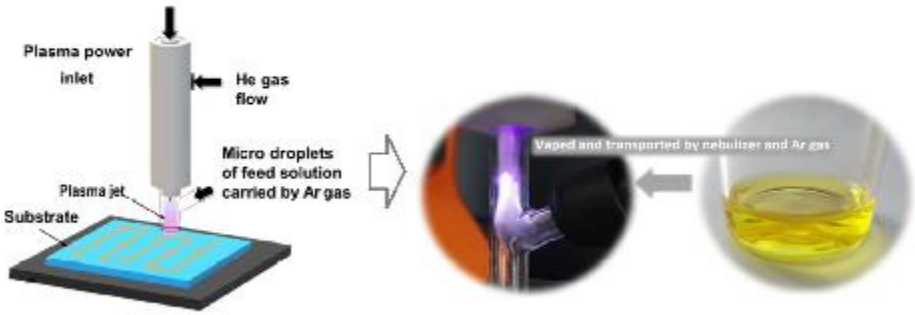

Figure S1. Plasma deposition setup schematics accompanied with photos of operando reduction–deposition process and feeding solution of water-diluted $HAuCl_4$ precursor.

SEM, TEM and size distribution analysis. Size, shape and arrangement of freshly deposited nanoparticles were investigated by exploiting a Prisma E scanning electron microscope (Thermo Fisher Scientific Inc.) in different magnifications using secondary emitted electrons accelerated at a voltage of 10 keV. Transmission electron microscopy (TEM, JEM-2100, Jeol Inc.) functioning at 200 kV was employed to characterise the gold nanoparticle's morphology. The images were collected by a slow-scan CCD camera (Orius SC1000, Gatan). Statistical data regarding the spatial distribution of nano-gold within a cluster was provided via software *ImageJ* using different circularity filters for each discrete task.[26]

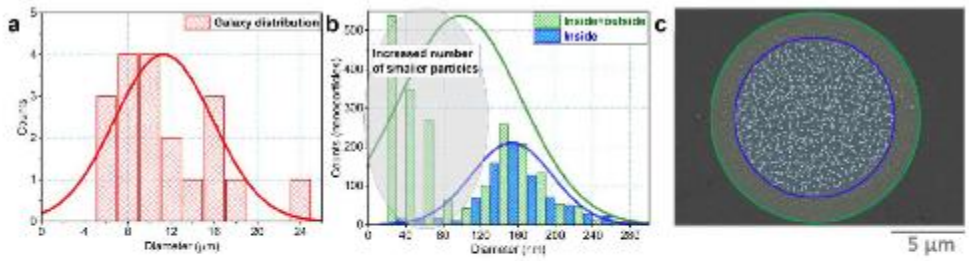

Figure S2. (a) - Mean size distribution of Au clusters. (b) Size distribution analysis of NPs enclosed within selected areas displayed in (c)

EDS and diffuse optical reflectance. The elemental composition of a selected area of the sample was carried out by energy-dispersive x-ray spectroscopy under acceleration voltage equal to 10 keV and an acquisition time of 120 s. A double beam UV–Vis spectrophotometer fabricated by Perkin Lambda (model 1050) equipped with a 150 mm integrating white sphere module was utilised to investigate the diffuse reflectance covering a spectral interval of 400–700 nm with a resolution of 0.2 nm.

Table S1. Surface composition of the plasma reduced gold nanoparticles on Si from EDS test.

Element	Atomic %	Error	Weight %	Error
Si	98.3	0.2	89.6	0.2
Cl	0.1	3.7	0.1	3.7
Au	1.6	3.7	10.3	3.7

X-ray photoelectron spectroscopy. The oxidation state of gold nanoparticles was investigated using PHI-TFA-XPS spectrometer (Physical Electronics Inc.) armed with an Al-monochromatic photon source operating at an energy of 1486.6 eV. XPS peak intensities were fitted via the OriginLab software package, using a Gauss–Lorentz function with Shirley-type background subtraction. The analysed surface area was approximately 400 μm^2.

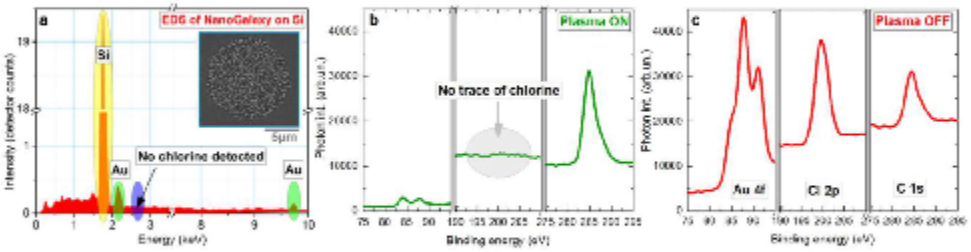

Figure S3. (a) Energy-dispersive X-ray spectroscopy (EDS) of Au-decorated silicon given in the inset. (b-c) XPS survey cut-off regions represent the absence of chlorine (Cl 2p) regarding clearly detected Au4f peaks after plasma deposition. Carbon C 1s peak is included as a reference peak.

Remarks: The curve "Plasma OFF" was recorded from a dried droplet of precursor with a focused X-ray beam on it; thus XPS signal is quite pronounced. An important piece of information here is the relative intensity of the Cl to Au peak. In the case of "plasma OFF", regime peak intensities are more or less similar, while for "Plasma ON" mode, there is no Cl 2p peak detected at all.

SERS measurements of crystal violet and DNA fragment. Vibrational spectra of model CV dye dissolved in water at different concentrations (5×10^{-5}–1×10^{-8} M) were collected using a confocal μ-Raman spectrometer (NT-MDT, model NTegra Spectra II) operating at 633 nm wavelength of a He-Ne laser. A 20× objective lens with a numerical aperture of 0.40 was used for laser beam control. At first, 1 μl of CV solution was pipetted on the sample surface and dried at ambient conditions. Then, Raman spectra of DNA samples were taken after 5 s laser exposure and an accumulation number of 3.

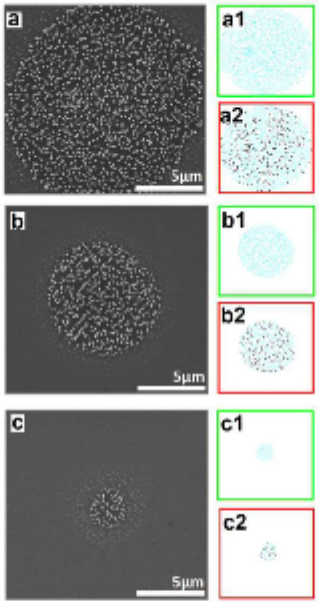

Figure S4 (a–c) BE-SEM images of gold clusters with different diameter. (a1–c1) Counted nanoparticles using ImageJ software when a "circularity" filter is in soft mode. (a2–c2) The same clusters processed with a rigorous "circularity" threshold (black particles are omitted).

Electromagnetic simulations. The distances between the different nano-aggregates are on the order of 30 µm and, therefore, no interaction is expected to occur between the individual Au clusters at visible wavelengths. Our interest is in calculating the FD within the selected area shown in Figure 3**a**. Due to the large number of NPs forming the circular pattern, simulating the FD within the micron-scale cluster would require huge computation time and resources. Therefore, two cases were considered and compared in the simulations to test the reliability of the results. First, periodic structure (along *x*- and *y*-directions) was considered in Figure 3 from the manuscript, where the unit cells represent the part of the nano-gold aggregate which was selected to build, as much as possible, a reliable EM simulation. In other words, the unit cell must include

single NPs, dimers and NP chains to give a realistic insight into the signal enhancement origin. The modelled structure was created in AutoCAD software. Since the Au particles deposited on the silicon substrate are neither completely spherical nor bipyramidal-like shaped, it was decided to elaborate on two extreme types of NP geometries, namely ideal spheres and bipyramids of the same size (Figure S5). Following this modelling logic, the real case scenario will for sure fall within results obtained for extreme geometries, increasing the credibility of theory–experiment interplay.

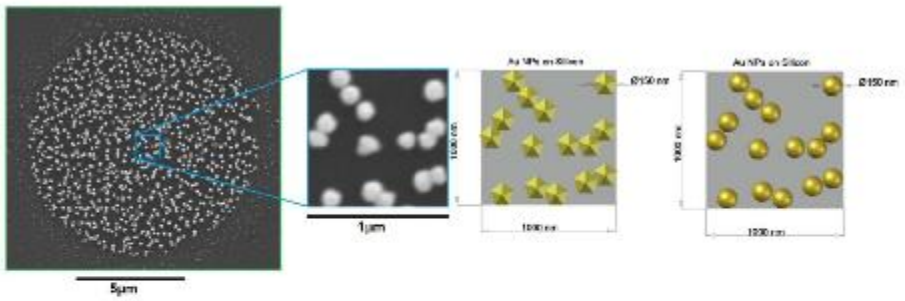

Figure S5. SEM image of NP interplays, where single nano-objects, dimers and chains are observed in the close neighbourhood. SEM is accompanied by corresponding 3D models using spherical and bipyramidal NP geometries.

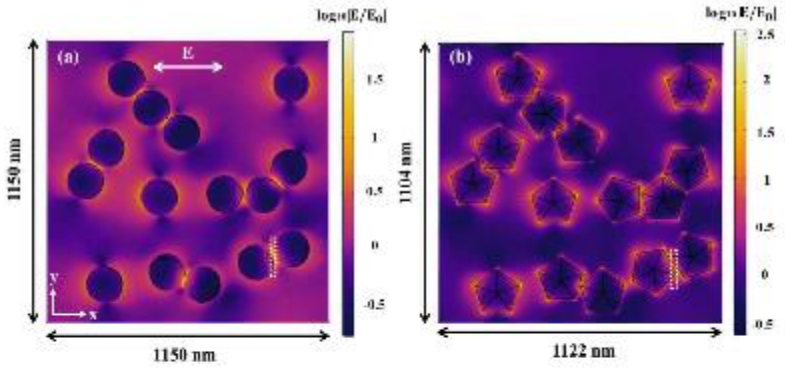

Figure S6. FD inside the unit cell of the considered periodic structure with (a) spherical and (b) non-spherical shape of the NPs. λ = 633 nm, normal incidence and TE polarisation were used to simulate the gold NPs on a silicon substrate. Air was assumed to exist between the NPs and for the superstrate. The field values are shown on a logarithmic scale.

As can be observed, the circular nano-gold pattern includes ~9 periods as the unit cell size in both *x*- and *y*-directions; this was the motivation for simulating the periodic structure. The field values in the manuscript are shown between minimum and maximum values to qualitatively show the location of the hot spots in a clear way by changing the colour bar. This provides more information regarding the calculated values of the electric field (shown in logarithmic scale) at each point in the structure as numerically achieved from the software without changing the colour bar; please see Figure S6, which is also important to demonstrate the fact that using the distorted NPs, higher enhancement is achieved because higher field values are observed in Figure S6**a** and S6**b**. In addition, several tests were performed to verify the accuracy and reliability of the calculation of the local FE in Figure S6. Average field calculations were also carried out inside defined boxes around the tiny gaps where the hot spots were observed (please see the dotted white regions in Figure S6**a** and Figure S6**b**; the box dimensions are: 30, 110, 10 nm in *x*, *y* and *z* axes, respectively). The calculations showed that a factor of ~2 enhancement in both the local and average fields in the case of the distorted NPs compared to the spheres due to the existence of the sharp edges.

The second simulation case is presented in Figure S7 below and considers a single spherical NP cluster. Figure S7 shows the FD inside the single spherical NP cluster for both TE (Figure S7**a**) and transverse magnetic (TM) (Figure S7**b**) **polarisations at λ = 633 nm and normal incidence in** which, for both cases, the largest FE (hot spots) is observed in the small gaps between the dimers and NPs forming the three NP groups. Finally, it is important to note that the FD inside the NP

cluster for the TE case (Figure S7)) showed similar FD behaviour as in the case of the periodic structure. This can tell us about the reliability of the simulation in regard to the FD within the NP cluster.

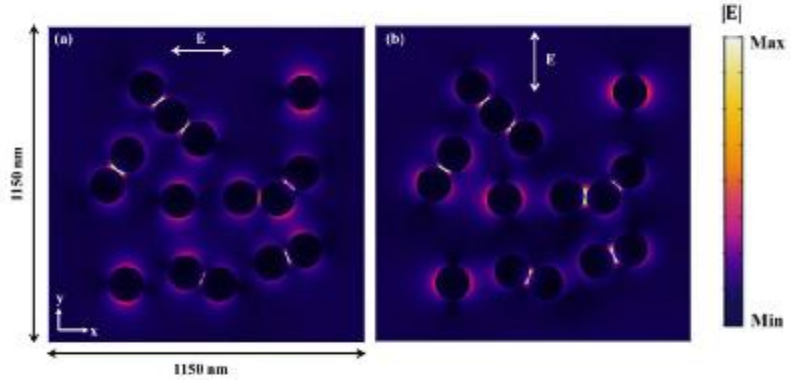

Figure S7. FD inside the single spherical NP cluster. λ = 633 nm, and normal incidence and TE polarisation (a) and TM polarisation (b) were used in the simulation of the gold NPs on a silicon substrate. Air was assumed to exist between the NPs and for the superstrate.

Bacterial DNA extraction. Genomic DNA fragments used for SERS experiments were isolated from 1.5 ml of an overnight culture of *Escherichia coli, Janthinobacterium lividum*, *Micrococcus luteus* and *Staphylococcus aureus* using GenEluteTM Bacterial Genomic DNA Kit (Merck, Darmstadt, Germany) according to the manufacturer's protocol. After the isolation procedure, DNA molecules were stored in elution solution, prepared from 10 mM Tric-HCl and 0.5 mM EDTA, pH 9.0. DNA concentration was measured using TayCell® (Hellma, Müllheim, Germany) and UV/VIS Lambda 1050 (Perkin Elmer, Massachusetts, USA). For SERS analysis, DNA solution with a concentration of 100 ± 10 ng/µl was pipetted on the silicon surface with pre-deposited nano-gold. The genomic ratio GC% of each bacterial DNA was extracted from a data library accessible using a link (https://genomes.atcc.org/genomes).

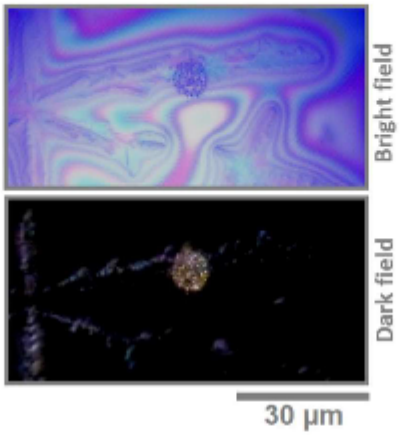

Figure S8. Optical image in bright-field and dark-field modes of the sensing substrate with dried DNA fragment deposited on top of it.

Gaussian deconvolution. Before extracting meaningful data, spectra were elaborated mathematically. Step one was a baseline subtraction using asymmetric least-squares fitting. The second procedure was to reduce noise from experimental curves by applying the locally estimated scatterplot smoothing (LOESS) function based on one main parameter: window size. Then, intensity normalisation was performed, ranging from 0 to 1 linked as minimum and maximum values. As a result, four spectra from different biospecies were obtained for Gaussian deconvolution, focusing on the most distinct Raman modes. The extructed fitting parameters are collected in Tables S2-S4.

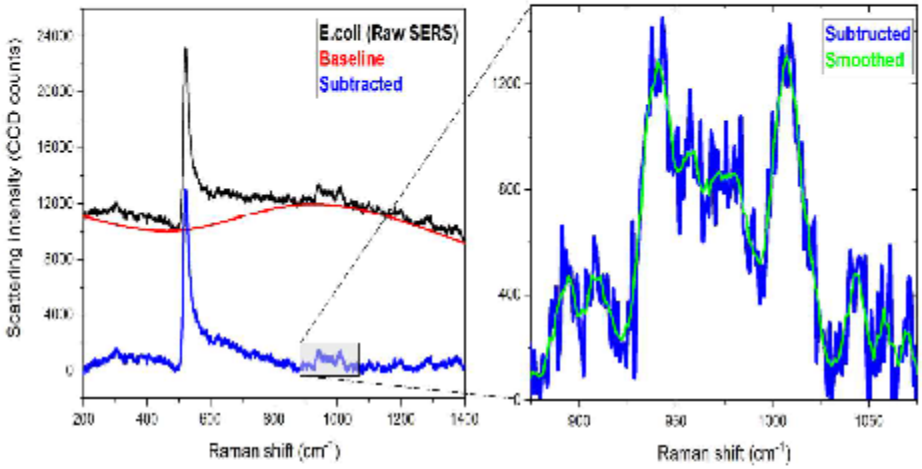

Figure S9. The preparation procedure of raw SERS spectra for PCA and Gaussian peak deconvolution.

Table S2. Relevant fitting parameters after Gaussian deconvolution for **guanine** peak.

	S. aureus	**E. coli**	**J. lividum**	**M. luteus**
Peak position	939.7±0.2	940.10±0.3	939.4±0.6	939.2±0.6
Peak Area	2.1±0.1	1.9±0.1	2.1±0.3	2.5±0.3
FWHM	16.7±0.6	16.3±0.4	15.9±0.6	15.8±0.7

Table S3. Relevant fitting parameters after Gaussian deconvolution for **thymine** peak.

	S. aureus	**E. coli**	**J. lividum**	**M. luteus**
Peak position	1008.6±0.2	1007.7±0.1	1008.1±0.2	1007.4±0.4
Peak Area	3.0±0.1	1.9±0.1	1.9±0.2	2.0±0.6
FWHM	15.9±0.3	16.2±0.5	16.1±1.2	17.0±2.8

Table S4. Relevant fitting parameters after Gaussian deconvolution for cytosine peak.

	S. aureus	*E. coli*	*J. lividum*	*M. luteus*
Peak position	1021.1±0.2	1021.2±0.4	1021.2±0.5	1021.2±0.1
Peak Area	0.15±0.02	0.23±0.04	0.40±0.08	0.46±0.11
FWHM	10.0±1.5	10.4±0.6	10.2±0.8	10.0±0.7

Step-by-step methodology of PC analysis. First, let's notice, that the most structurally valuable information is hidden within spectral intervals where intense peaks of guanine, cytosine and thymine occur. Thus, it was a solid reason to focus special attention on a reduced wavenumbers range of about 900-1050 cm^{-1}. Raw experimental data were elaborated similarly to a procedure employed for the spectra processing in the "Gaussian deconvolution" section. In total, 40 collected raw spectra, ten for each bacterial DNA, were baseline subtracted, smoothed, and normalised to run the principal component analysis approach. To reduce data dimensionality by multivariate ordination approach, special attention was focused on the first three principal components marked as PC1, PC2, PC3, pretending to order measured DNA spectra in a plane defined by two axes (PC1 vs PC2, PC1 vs PC3, and PC2 vs PC3) according to their extructed values. Following the well-known steps of the method (step 1: *standardisation*; step 2: *covariance matrix computation*; step 3: *compute the eigenvectors and eigenvalues of the covariance matrix to identify the principal components*), the analysis was accomplished. After the first step, needed to equalise the contribution of each continuous initial variable to the analysis, the scoring plot is obtained (**Figure S10**). Observing a graph in-depth, it can be pinpointed that PC1 asks a question, "which spectrum contains both guanine and thymine within a defined spectral range?". Subsequently, the PC2

scoring plot puts another query, "which spectrum reveals a more intense thymine Raman peak?" Lastly, in the remaining data, PC3 is interested "which spectrum possesses a larger difference between guanine and thymine peaks?"

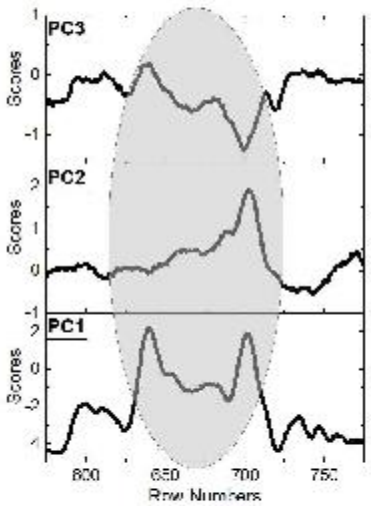

Figure S10. PCA creates lines in terms of least squares approximation by subtracting the mean and dividing by the standard deviation for each variable's value. All is reflected as PCs scores.

Afterwards of steps "2" (a covariance matrix is just a table summarising the relativeness between the created variable's pairs) and "3" (principal components are parameters constructed as linear combinations of the initial variables or their mixtures), the following graph with PCs for all spectra is obtained (**Figure S11**)

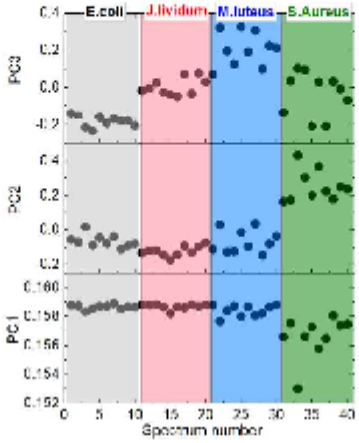

Figure S11. Calculated principal components for all spectra recorded.

It is worth noticing the values grouped better with increasing order of principal components. To visualise the clustered spectra of DNA, it is needed to take a closer look at 3D loading plots, where PCs serve as axis values (Figure S12). Although the 3D plot is a bit eye-confusing, its orthogonal projection reflects the situation on quite a decent level. In particular, a combination of higher-order components PC2 and PC3 classifies all measured vibrational spectra the best regarding their fundamental genomic ratio GC%. It can be related to PCs variance between their minimum and maximum values. This difference for PC1 ($\Delta(PC1_{max}\text{-}PC1_{min}) = 0.006$) is rather small, corresponding to about 100-fold less than that found for PC2 and PC3, where $\Delta(PC2_{max}\text{-}PC2_{min}) = 0.603$ and $\Delta(PC3_{max}\text{-}PC3_{min}) = 0.562$, respectively. Consequently, a projection onto the orthogonal line using only PC1 is not sufficient to pinpoint sufficient data grouping. In contrast, orthogonal planes comprising higher principal components are way more useful for analysing a large set of datapoint (Raman spectra) interlinked by common structural features.

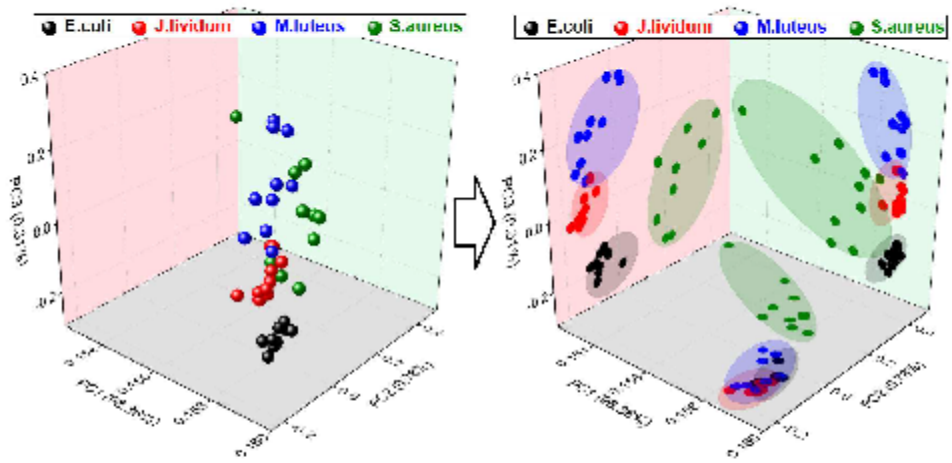

Figure S12. 3D visualisation of PCs loading plots accompanied by their projections onto main orthogonal loading planes.

DNA sequencing for GC% validation

Bacterial DNA concertation and purity were measured on NanoDrop 1000, 200 ng used for library preparation following Rapid Barcoding Sequencing protocol (SQK-RBK004, Oxford Nanopore Technologies) and sequenced on GridION sequencing device (FLO-MIN106 flowcell). Software for sequencing was MinKNOW, with Guppy basecaller. Sequencing quality was checked with NanoPlot software. Genomes were assembled with Flye software, and nucleotide content was extracted from reads with a custom-developed algorithm written in Python. Assemblies and extracted contents were compared, where 4.73 +/- 5.52 percent difference was observed.

DNA concentation and purity were measured on NanoDrop 1000. The library was prepared according to the Rapid Barcoding Sequencing protocol (SQK-RBK004, Oxford Nanopore Technologies). 200 ng of DNA was diluted to 7,5 µl in H_2O (concentration 26,67 ng/µl), for each bacterial strain in a separated 0.2 ml thin-walled PCR tube. 2,5 µl of Fragmentation Mix was added to the sample, for fragmentation and barcoding of samples (strains and corresponding barcodes are presented in Table S5). Samples and Fragmentation mix were incubated for 1 min on 30°C, 1 min on 80°C and put on ice to cool down. Barcoded samples were then pooled in 1,5 ml Eppendorf DNA LoBind tube, 40 µl of AMPure XP (Beckman Coulter) beads were added and incubated on a Hula mixer for 5 min at room temperature. Samples were put on a magnetic stand, and the supernatant was removed, washed two times with 70% ethanol and dried on air. Beads were resuspended in 10 µl of 10 mM Tris-HCl pH 7.5 with 50 mM NaCl, 10 µl of eluate-containing library was removed from the beads on a magnetic stand. 1 µl of RAP (Rapid Adapter) was added and incubated for 5 min at room temperature. 34 µl of SQB (Sequencing Buffer), 25,5 µl of LB (Loading Beads) and 4,5 µl of H_2O was added to the library and loaded to activated flow cell. Sequencing was run on GridION sequencing device (FLO-MIN106 flowcell, Oxford Nanopore Technologies), for 43 hours, producing a total of 1,23*10^6 fragment reads corresponding to 7.73 Gb of base pairs, with an estimated average read length 11,01 kb.

Table S5. Concentrations and sample purity with corresponding barcodes

Sample name	*S. aureus*	*M. luteus*	*J. lividum*	*E. coli*
Barcode	R1	R2	R3	R4
ng/µl	30.40	44.46	44.52	46.02
260	0.608	0.889	0.890	0.920
280	0.403	0.491	0.532	0.525

260/280	1.510	1.810	1.750	1.670
260/230	3.401	11.520	3.380	2.110
Volume for 200ng (µl)	6.58	4.50	4.49	4.35
Volume of H_2O (µl)	0.92	3.00	3.01	3.15

Raw sequencing data (*FAST5* files) was basecalled with *MinKNOW* software (version 21.11.7) on *GridION* sequencer (Oxford Nanopore Technologies). The basecaller used was *Guppy* (version 5.1.13) with a *High-accuracy basecalling* model, and sequencing reads were filtered with a minimum quality score of 9. After basecalling, the resulting *FASTQ* files (each containing 4000 reads), were merged to form one continuous file for each of the barcoded samples.

Sequencing quality was checked with *NanoPlot* software (version 1.36.2). Quality metrics are presented in Table S6.

Table S6. NanoPlot experiment quality metrics

	Mean read length	Mean read quality	Read length N50	Number of reads	Number of bases
Barcode – R1	1,629.0	11.6	3,615.0	49,445	80,543,832
Barcode – R2	7,341.5	11.7	13,164.0	89,472	656,857,414
Barcode – R3	7,199.9	11.9	12,654.0	273,574	1,969,709,635
Barcode – R4	5,598.4	11.9	9,896.0	556,732	3,116,808,015
Unclassified	5,412.2	6.7	10,380.0	256,812	1,390,690,486
Experiment	5,884.5	11.0	10,881.0	1,226,168	7,215,347,868

Bacterial genomes were assembled using *Flye* assembler (version 2.8.3-b1695). Assembled genomes were circularised with exception of *R1*, where a lower number of reads with shorter overall read length led to low genomic coverage (average contig coverage of 15x compared to more than 200x for other samples).

Assembled genomes were checked against the NCBI BLAST database (https://blast.ncbi.nlm.nih.gov/), for the best matches of the assembly to the reference genomes (Table S7).

Table S7: Barcode to NCBI BLAST database comparison

Barcode	Reference name	Identification percentage
R1	Staphylococcus aureus	99.97%
R2	Micrococcus luteus	99.98%
R3	Janthinobacterium lividum	97.30%
R4	Escherichia coli	99.99%

An algorithm for calculating separate nucleotide content was written and developed in Python programming language (version 3.7.3). The calculation was done in reads through time. Reads were grouped by time passed (every minute), and nucleotide content was calculated for each group. The output of the algorithm presented how nucleotide content was changing through time (Figure S13).

The nucleotide content of reads was further compared to the nucleotide content of assembled genomes. The observed differences (4.73 +/- 5.52) can be attributed to the assembly method/algorithm and other plasmids/genomes in the sequencing library. In contrast, when

assembled genomes were compared to the database references (https://www.patricbrc.org), differences in GC content were 0.11 +/- 0.098 percent.

The outlier in the last comparison was barcode *R1*. There the assembly fragments (although not circularised) GC nucleotide content was similar to the whole genome sequencing reference, but read GC content differed by a higher margin (5.35 percent). The cause of this could be attributed to sampling quality or contamination.

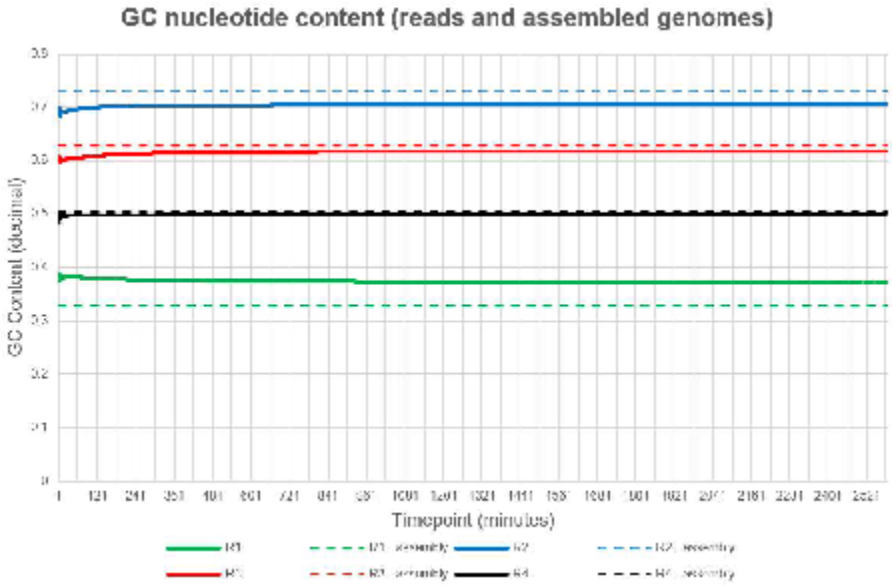

Figure S13. GC nucleotide content of reads and assembled genomes. Assembled genome GC nucleotide content (dashed line) does not change because it represents total genomic GC content.

AUTHOR CONTRIBUTIONS

V.S., M.M., U.C. conceived the research idea, guided the overall research progress and provided the final draft; A.V. co-wrote the first draft (synthesis part); A.V., J.Z.. contributed nanogold

synthesis, microscopy; M.M. prepared DNA analytes; V.S. and D.V. performed optical measurements, SERS and PCA analysis; M.A. and I.A. provided the electromagnetic field simulations and wrote the related text; C.S, N.N, D.R provided DNA reading measurements and genomic data, V.S., I.A., A.Z., and U.C. supervised, reviewed and prepared the final version of the paper.

Corresponding Authors

Vasyl Shvalya*. Department of Gaseous Electronics (F6), Jožef Stefan Institute, Jamova cesta 39, SI-1000 Ljubljana, Slovenia, EU. *Email:* vasyl.shvalya@ijs.si

Uroš Cvelbar*. Department of Gaseous Electronics (F6), Jožef Stefan Institute, Jamova cesta 39, SI-1000 Ljubljana, Slovenia, EU. *Email:* uros.cvelbar@ijs.si

Notes

All authors declare no conflict of interest.

ACKNOWLEDGMENT

The current work is supported by NATO grant G5814 – NOOSH; PEGASUS project (Plasma Enabled and Graphene Allowed Synthesis of Unique Nano-structures, No. 766894); ARRS program P1-0417, grant no. J4-1770 and AD FUTURA, Public Scholarship, Development,

Disability, and Maintenance Fund of the Republic of Slovenia. C. S., N. N and D. R would like to acknowledge P1-0390, MRIC-ELIXIR and ELIXIR-SI RI-SI-2.

ABBREVIATIONS

DNA - deoxyribonucleic acid; SERS – surface-enhanced Raman spectroscopy; XPS – X-ray photoelectron spectroscopy; EDS - energy-dispersive X-ray spectroscopy; SEM – scanning electron microscopy; NPs – nano particles; LSPR – localised surface plasmon resonance; CV – crystal violet; FE – field enhancement; EM – electromagnetic; FD – field distribution; PCS – principal component analysis; G – guanine; T – thymine; A – adenine; C – cytosine, TM-transverse magnetic, TE – transverse electric.

REFERENCES

(1) Baümler, A. J.; Sperandio, V. Interactions between the Microbiota and Pathogenic Bacteria in the Gut. *Nature* **2016**, *535* (7610), 85–93. https://doi.org/10.1038/nature18849.

(2) Gao, F.; Lei, J.; Ju, H. Label-Free Surface-Enhanced Raman Spectroscopy for Sensitive DNA Detection by DNA-Mediated Silver Nanoparticle Growth. *Anal. Chem.* **2013**, *85* (24), 11788–11793. https://doi.org/10.1021/ac4032109.

(3) Liu, N.; Liedl, T. DNA-Assembled Advanced Plasmonic Architectures. *Chem. Rev.* **2018**, *118* (6), 3032–3053. https://doi.org/10.1021/acs.chemrev.7b00225.

(4) Macdonald, D.; Smith, E.; Faulds, K.; Graham, D. DNA Detection by SERS: Hybridisation Parameters and the Potential for Asymmetric PCR. *Analyst* **2020**, *145* (5), 1871–1877. https://doi.org/10.1039/c9an01732a.

(5) Pyrak, E.; Krajczewski, J.; Kowalik, A.; Kudelski, A.; Jaworska, A. Surface Enhanced Raman Spectroscopy for DNA Biosensors - How Far Are We? *Molecules* **2019**, *24* (24). https://doi.org/10.3390/molecules24244423.

(6) Kravets, V. G.; Kabashin, A. V.; Barnes, W. L.; Grigorenko, A. N. Plasmonic Surface Lattice Resonances: A Review of Properties and Applications. *Chem. Rev.* **2018**, *118* (12), 5912–5951. https://doi.org/10.1021/acs.chemrev.8b00243.

(7) **Shvalya, V.; Filipič, G.; Zavašnik, J.; Abdulhalim, I.; Cvelbar, U. Surface**-Enhanced Raman Spectroscopy for Chemical and Biological Sensing Using Nanoplasmonics: The Relevance of Interparticle Spacing and Surface Morphology. *Appl. Phys. Rev.* **2020**, *7* (3), 031307. https://doi.org/10.1063/5.0015246.

(8) Amendola, V.; Pilot, R.; Frasconi, M.; Maragò, O. M.; Iati, M. A. Surface Plasmon Resonance in Gold Nanoparticles: A Review. *J. Phys. Condens. Matter* **2017**, *29* (20). https://doi.org/10.1088/1361-648X/aa60f3.

(9) Pilot; Signorini; Durante; Orian; Bhamidipati; Fabris. A Review on Surface-Enhanced Raman Scattering. *Biosensors* **2019**, *9* (2), 57. https://doi.org/10.3390/bios9020057.

(10) Abdulhalim, I. Coupling Configurations between Extended Surface Electromagnetic Waves and Localised Surface Plasmons for Ultrahigh Field Enhancement. *Nanophotonics* **2018**, *7* (12), 1891–1916. https://doi.org/10.1515/nanoph-2018-0129.

(11) Zhang, P.; Ma, G.; Dong, W.; Wan, Z.; Wang, S.; Tao, N. Plasmonic Scattering Imaging of Single Proteins and Binding Kinetics. *Nat. Methods* **2020**, *17* (10), 1010–1017. https://doi.org/10.1038/s41592-020-0947-0.

(12) Woo, A.; Lim, K.; Cho, B. H.; Jung, H. S.; **Lee, M. Highly Sensitive and Repeatable DNA-SERS Detection System Using Silver Nanowires-glass Fiber Filter Substrate.** *Anal. Sci.*

Adv. **2021**, *2* (7–8), 397–407. https://doi.org/10.1002/ansa.202000096.

(13) Huang, J. A.; Mousavi, M. Z.; Zhao, Y.; Hubarevich, A.; Omeis, F.; Giovannini, G.; Schütte, M.; Garoli, D.; De Angelis, F. SERS Discrimination of Single DNA Bases in Single Oligonucleotides by Electro-Plasmonic Trapping. *Nat. Commun.* **2019**, *10* (1), 1–10. https://doi.org/10.1038/s41467-019-13242-x.

(14) Hong, J.; Yick, S.; Chow, E.; Murdock, A.; Fang, J.; Seo, D. H.; Wolff, A.; Han, Z.; Van Der Laan, T.; Bendavid, A.; Ostrikov, K.; Murphy, A. B. Direct Plasma Printing of Nano-Gold from an Inorganic Precursor. *J. Mater. Chem. C* **2019**, *7* (21), 6369–6374. https://doi.org/10.1039/c9tc01808e.

(15) Richmonds, C.; Sankaran, R. M. Plasma-Liquid Electrochemistry: Rapid Synthesis of Colloidal Metal Nanoparticles by Microplasma Reduction of Aqueous Cations. *Appl. Phys. Lett.* **2008**, *93* (13), 129–132. https://doi.org/10.1063/1.2988283.

(16) Khatoon, N.; Yasin, H. M.; Younus, M.; Ahmed, W.; Rehman, N. U.; Zakaullah, M.; Iqbal, M. Z. Synthesis and Spectroscopic Characterization of Gold Nanoparticles via Plasma-Liquid Interaction Technique. *AIP Adv.* **2018**, *8* (1). https://doi.org/10.1063/1.5004470.

(17) Zou, J. J.; Zhang, Y. P.; Liu, C. J. Reduction of Supported Noble-Metal Ions Using Glow Discharge Plasma. *Langmuir* **2006**, *22* (26), 11388–11394. https://doi.org/10.1021/la061795b.

(18) Kaneko, T.; Baba, K.; Hatakeyama, R. Gas-Liquid Interfacial Plasmas: Basic Properties and Applications to Nanomaterial Synthesis. *Plasma Phys. Control. Fusion* **2009**, *51* (12). https://doi.org/10.1088/0741-3335/51/12/124011.

(19) Bossard-Giannesini, L.; Cruguel, H.; Lacaze, E.; Pluchery, O. Plasmonic Properties of Gold Nanoparticles on Silicon Substrates: Understanding Fano-like Spectra Observed in

Reflection. *Appl. Phys. Lett.* **2016**, *109* (11). https://doi.org/10.1063/1.4962731.

(20) Meng, W.; Hu, F.; Zhang, L. Y.; Jiang, X. H.; Lu, L. De; Wang, X. SERS and DFT Study of Crystal Violet. *J. Mol. Struct.* **2013**, *1035*, 326–331. https://doi.org/10.1016/j.molstruc.2012.10.066.

(21) Cañamares, M. V.; Chenal, C.; Birke, R. L.; Lombardi, J. R. DFT, SERS, and Single-Molecule SERS of Crystal Violet. *J. Phys. Chem. C* **2008**, *112* (51), 20295–20300. https://doi.org/10.1021/jp807807j.

(22) Hao, E.; Schatz, G. C. Electromagnetic Fields around Silver Nanoparticles and Dimers. *J. Chem. Phys.* **2004**, *120* (1), 357–366. https://doi.org/10.1063/1.1629280.

(23) Huang, Y.; Zhou, Q.; Hou, M.; Ma, L.; Zhang, Z. Nanogap Effects on Near- and Far-Field Plasmonic Behaviors of Metallic Nanoparticle Dimers. *Phys. Chem. Chem. Phys.* **2015**, *17* (43), 29293–29298. https://doi.org/10.1039/C5CP04460J.

(24) Huang, Y.; Chen, Y.; Wang, L.-L.; Ringe, E. Small Morphology Variations Effects on Plasmonic Nanoparticle Dimer Hotspots. *J. Mater. Chem. C* **2018**, *6* (36), 9607–9614. https://doi.org/10.1039/C8TC03556C.

(25) Otto, C.; van den Tweel, T. J. J.; de Mul, F. F. M.; Greve, J. Surface-Enhanced Raman Spectroscopy of DNA Bases. *J. Raman Spectrosc.* **1986**, *17* (3), 289–298. https://doi.org/10.1002/jrs.1250170311.

(26) Igathinathane, C.; Pordesimo, L. O.; Columbus, E. P.; Batchelor, W. D.; Methuku, S. R. Shape Identification and Particles Size Distribution from Basic Shape Parameters Using ImageJ. *Comput. Electron. Agric.* **2008**, *63* (2), 168–182. https://doi.org/10.1016/j.compag.2008.02.007.

BRIEFS.

High-performing plasma-coupled nanogold provides a reliable pathway for distinctive surface-enhanced Raman analysis of bacterial DNA fragments

SYNOPSIS. Graphical abstract

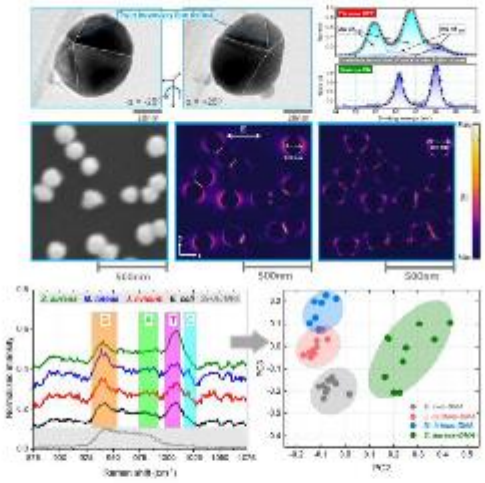

Chapter 5

Possibilities of Two-Dimensional Materials with Atmospheric Pressure Plasmas

This chapter is a mini-review that investigates the present and future possibilities of atmospheric pressure plasma jet and deposition of nanoparticles for the modification of two-dimensional materials. Two-dimensional materials like graphene and metal composites with similar 2D geometries are of major interest for the development of future electrical and electronic devices. Plasma, on the other hand, can easily manipulate the physical and electronic properties of the materials with simple surface modification. Plasmas can successfully manipulate the properties of 2D materials like graphene. Moreover, atmospheric pressure plasmas can provide a controlled change in the band gap of the materials, increased sensitivity, and improved structural stability to the materials by simply modifying their surface or adding foreign atoms like gold to the carbon lattice. Specifically, the edges of the 2D materials are more significant for nanoelectronics devices. 2D materials like nanoribbons, nanowalls, and nanosheets can be easily tailored by selectively doping adatoms like Au and N. Besides the modifications to materials, plasma also supports the growth and synthesis of nanostructures. The contributions from plasma in tailoring the materials can lead to an emerging field of nanoelectronics. This chapter discusses the modification of 2D carbon nanostructures specifically for novel edge-electronics using plasma technology.

Regarding the contribution of the author: The author of the dissertation has contributed to the idea and wrote the manuscript.

Front. Chem. Sci. Eng.
https://doi.org/10.1007/s11705-019-1805-4

REVIEW ARTICLE

Tailoring electrical conductivity of two dimensional nanomaterials using plasma for edge electronics: A mini review

Aswathy Vasudevan[1,2], Vasyl Shvalya[1], Aleksander Zidanšek[1,2,3], Uroš Cvelbar (✉)[1,2]

1 Jožef Stefan Institute, 1000 Ljubljana, Slovenia
2 Jožef Stefan International Postgraduate School, 1000 Ljubljana, Slovenia
3 Faculty of Natural Sciences and Mathematics, University of Maribor, 2000 Maribor, Slovenia

Abstract Since graphene has been discovered, two-dimensional nanomaterials have attracted attention due to their promising tunable electronic properties. The possibility of tailoring electrical conductivity at the atomic level allows creating new prospective 2D structures for energy harvesting and sensing-related applications. In this respect, one of the most successful way to manipulate the physical properties of the aforementioned materials is related to the surface modification techniques employing plasma. Moreover, plasma-gaseous chemical treatment can provide a controlled change in the bandgap, increase sensitivity and significantly improve the structural stability of material to the environment as well. This review deals with recent advances in the modification of 2D carbon nanostructures for novel 'edge' electronics using plasma technology and processes.

Keywords graphene, edge electronics, 2D nanomaterials, plasma, electrical conductivity

1 Introduction

Nanomaterials for electrochemical applications include the one-dimensional (1D) structures like nanoribbons, nanotubes and nanowires, the two-dimensional (2D) including single atom thick nanomaterials, nanowalls, nanoflakes and the three-dimensional (3D) such as quantum dots, nanoparticles, nanoballs and nanocones [1]. At various dimensions, the same chemical composition and structure can exhibit different properties while considering reduced scales. Graphene is an excellent material that can demonstrate this scaling effect. For example, below 10 nanometers, bandgap and transport properties are being changed, which is directly reflected in electrical conductivity. In 2005, Novoselov and co-workers presented graphene as a dense honeycomb crystal structure that can be considered as unrolled single-wall carbon nanotubes (SWCNTs). The authors have shown that the conductivity of one layer graphene sheet cannot be lower than a minimum value corresponding to the quantum unit of conductance, even when charge carriers concentrations approach to zero. Moreover, graphene possesses a strong integer quantum Hall effect at half-integer filling factors [2].

After discovering 3-dimensional fullerene and 1-dimensional carbon nanotubes (CNT), the carbon-based nanostructures became the most frequently studied nanomaterials. Most of the synthesised new low-dimensional structures, such as nanoribbons obtained from 2D crystals [3–5], revealed characteristic sp^2-hybridised chemical bonds. This type of hybridisation can also be found in other non-carbon contained 2D materials. By affecting sp^2-hybridised bonds with different tools, such as plasma, the electrical conductivity, capacitance and catalytic properties of these materials can be altered in a controlled way.

Due to their promising electronic properties, the majority of all 2D materials can be classified into several groups: 2D semiconductors, 2D ferromagnetic, 2D superconductors, 2D semimetals, 2D topological insulators, 2D metals. The mother of all those perspective materials is graphene, which in turn, opened the path for synthesising low-dimensional structures such as transition metal dichalcogenides (TMDs), transition metal oxides (TMOs), transition metal hydroxides (TMHs), elemental 2D phosphorene, germanene, tinene and silicene. In recent years, single layered TMDs are becoming increasingly important due to their

Received September 29, 2018; accepted December 6, 2018

E-mail: uros.cvelbar@ijs.si

diverse electrical properties and natural abundance. For TMDs a generalised chemical formula MX_2 is used, wherein, 'M' typically represents a transition metal of the groups 4–10 (Mo, Nb, W, Ni, V, or Re) [8], where X is a chalcogen (Se, Te, or S) [9–11]. TMDs possess very diverse electronic structures, ranging from superconductors ($TaSe_2$, $NbSe_2$) to insulators (HfS_2), making them versatile for electrochemical energy storage applications [12]. Later, semiconducting molybdenum disulfide (MoS_2) got the attraction of researchers for energy storage applications [13] by functionalisation and defect engineering of this 2D TMDC material. Semimetals like $TiSe_2$, and metals like $NbSe_2$, are known because they exhibit superconductivity behaviour at low temperature [14–16]. Correspondingly, the newly developed 2D nanosheets of transition metal dichalcogenides and metal oxides with interesting electronic structure are being comprehensively investigated [17]. Similarly, TMOs have promising optical properties due to their characteristic bandgap. For example, MnO_2 has a bandgap of 2.1 eV and exhibits a strong photoelectrochemical response to visible light [18]. Silicenes and phosphorenes are elemental semiconducting materials that possess an inherent direct bandgap and exhibit similar electrical properties as graphene [15,16]. The bandgap of graphene and its analogues from this group (silicene, germanene, and tinene) increases along the row C → Si → Ge → Sn. Currently, known members of the 2D material family are listed in Table 1 [19]. For real practical applications, the structural stability of these materials plays a crucial role. Monolayers of graphene, 2D chalcogenides, semiconducting dichalcogenides ($MoTe_2$, WTe_2), and 2D oxides (MnO_2) are stable under ambient environments. However, the metallic dichalcogenides ($NbSe_2$, NbS_2) and layered semiconducting chalcogenides (GaSe, GaTe) are stable only in inert atmospheres [17].

Prospective electronic transport properties [20], mechanical stability [21], photoelectrochemical response [22], and temperature dependence of the bandgap [23] make these materials suitable for applications in electronic devices, sensors, catalysts, energy harvesting, and data storage devices [12].

2 Electronic properties of graphene

The 2D materials possess unique properties due to their structural characteristics and quantum size effects associated with their layer thickness [24]. Nano-sized thin layers can allow a close contact between the interfacial layers. Notable variations in the physical and chemical properties are also observed in such layered materials due to the electron confinement effect. However, the absence of interlayer interaction is significant when we explore their band structure. Those one-atom-thick layers enable direct access and simple processing of the mobile charge carriers and their high carrier mobility even at low temperatures [25]. Since the manuscript is mostly related to the electrical properties of 2D materials and possible routes of their modifications, a brief description of graphene band structure is presented in this section.

The unit cell of graphene includes two carbon atoms which are gathered in a well-known hexagonal honeycomb structure (Fig. 1(a)) [26]. The electronic structure consists of valence and conduction bands formed by π- and π^* states, respectively. The band diagram is characterised by six highly symmetric K and K' points, known as Dirac points E_{Dirac}, where the energy distance between two zones is close to zero (Fig. 1(b)). In the low energy region, which is important for electron transport, dispersion reveals a linear behaviour (Fig.1(c)). As a consequence, the characteristic band structure can be considered as two cones in touch at E_{Dirac} (Fig. 1(d)). Since both valence and conduction bands in graphene are in touch, new energy states form near the Fermi levels (see Fig. 1(d)), which are sensitive to external influences, such as electric fields, plasma interactions, mechanical deformations, doping and adsorption. This property is very desirable in sensing applications, making graphene-based materials suitable for electrochemical energy storage [27–29]. Outstanding electrical properties of graphene are caused by the linear dispersion relation of charge carriers, which mimic massless relativistic particles [2]. The transport properties of graphene are also attributed to the absence of long-range interaction backscattering processes. As a result, the electron/hole elastic mean free path is about hundreds of nanometers. In graphene, additional scattering mechanisms take place, which is initiated by acoustic and optic phonons. In the acoustic case, the scattering is rather weak, while for the optic waves it becomes relevant only at very high frequencies (~1600 cm^{-1} or ~4.8×10^{13} Hz). The last case is outside the scope of our study, as we do not deal with the high electric field. The elastic and inelastic collisions are the subject of interest in long graphene

Table 1 An overview of 2D materials according to their electrical conductivity properties

2D material	Members	Examples	Ref.
Conductors	2D metals, carbon-based materials	BiTe, BSCCO, FeTe, NbS_2,VSe_2, graphene	[6]
Semiconductors	2D metal chalcogenides, 2D halides, 2D phosphides, 2D arsenide, 2D oxides, elemental	Tellurene, black phosphorus, CuS, SnS, MoS_2, WS_2, $SnSe_2$, BPS, $FePS_3$, $FePSe_3$, $As2S_3$, As_2Se_3, MnO_2, PbI_2, CdI_2	[7]
Insulators	*h*-BN, 2D hydroxides, 2D micas	MoO_3, Sb_2OS_2, $Ca(OH)_2$, $Mg(OH)_2$	[7]

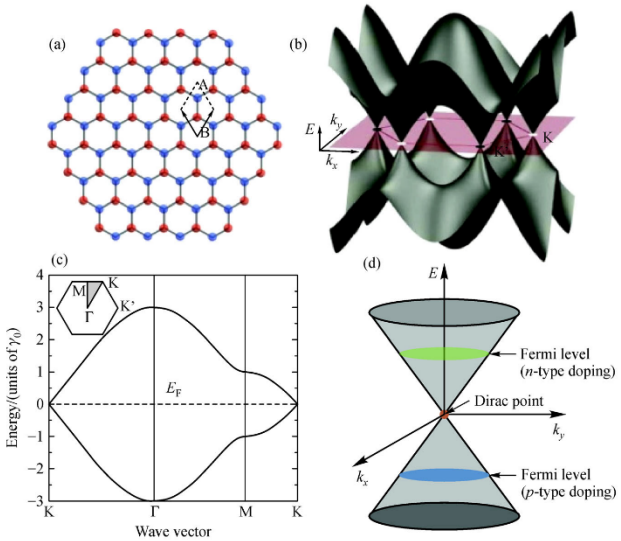

Fig. 1 Electronic structure of one layer graphene. (a) Honeycomb lattice structure of graphene consisting of two atoms (A and B); (b) The representation of the graphene band structure; (c) Phonon spectra of graphene. (d) The schematic representation of low energy band structure exhibiting zero energy gap at the Dirac point. 'Blue' and 'green' Fermi levels reveal *p*- and *n*-dopants states (reprinted with permission from the reference [26])

channels or in 2D nanostructures like nanoribbons, where the transport is changed from ballistic to diffusive [26]. In the case of 2D carbon nanostructures the scattering processes are mainly produced by impurities, defects or/and short-range phonon-phonon interactions, thus drastically reducing the mean-free path. In fact, the elastic collisions mechanisms caused by charged impurities, adsorbents and edge roughness are usually referred to as Coulomb scattering. On the other hand, the inelastic collisions that arise due to the acoustic and optical phonons can also contain the surface phonons of an insulating substrate [30]. Moreover, the scattering mechanisms and transport properties also depend on the edge structures and morphologies.

3 2D carbon nanostructure morphologies and transport properties

Two-dimensional structures can also be classified based on their interlayer bonding forces: layered van der Waals solids, layered ionic solids, and surface assisted non-layered solids. Layered van der Waals solids exhibit strong covalent or ionic bonds within the plane and weak van der Waals or hydrogen bonding out of the plane. They include atomically flat graphene, boron nitride (*h*-BN), phosphorene, transition metal dichalcogenides (TMDs), layered metal oxides. Layered ionic solids are 2D materials, which are assembled form of a charged polyhedral layer sandwiched between hydroxide or halide layers coupled by electrostatic forces. Compounds such as $La_{0.90}Eu_{0.05}Nb_3O_{10}$, $KLnNb_2O_7$, $Eu(OH)_{2.5}(DS)_{0.5}$ belong to this group. Surface-assisted nonlayered solids are materials comprised of an atomically thin-layered material, typically synthesised on a substrate via chemical vapour deposition (CVD) and epitaxial growth. Silicene and germanene are typical representatives of this category.

Interestingly, the deposition and growth of the 2D materials depend significantly on the medium and the substrate surface. During the epitaxial growth of structures on a substrate (usually a metal), the nanostructures like nanowalls, nanoislands and nanodisks are formed. These morphologies exhibit characteristic edges, which unveil different electronic structures compared with the centre areas of the islands [31]. Some characteristic two-dimensional shapes observed in literature are collected in Fig. 2. One of the most frequently obtained particles arrangements that grow on a substrate are nano-islands. The typical case of the gold island film prepared by vapour deposition [32] on top of the transparent substrates is

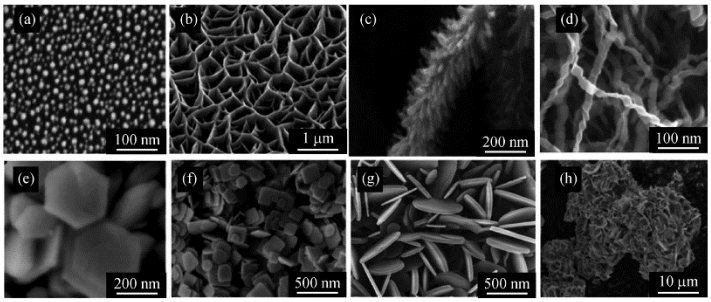

Fig. 2 Electron microscope images of different types of two-dimensional nanostructures. (a) Nano-island structure [37]; (b) Nanowalls [38]; (c) Branched nanostructures [39]; (d) Nanoribbons [40]; (e) Nanoplates [41]; (f) Nanodisks [42]; (g) Nanosheets [43]; (h) Nanoflowers [44]. (Reprinted with permission from the references listed above)

presented in Fig. 2(a). Nanodisks are the circular structures with specific enclosed edges. BiOCl single-crystal nanodisk (Fig. 2(e)) is for example used in photocatalytic activities due to its surface properties [33]. Branched nanostructures like for example ZnO branched nanowires are typically characterised by a higher surface area (Fig. 2(c)), which could be used in the photochemical cell for hydrogen evolution in water splitting [34]. Nanosheets and nanoplates are the flat 2D structures limited in surface area, which can be self-standing or bound to the surface. Examples are presented in Fig. 2(f) [35] and Fig. 3(g) [36].

2D nanosheets are materials with atomic or molecular thickness and large planar lengths so that the edges are not significant. The quantum confinement effects within the 2D layer govern the changes in electronic behaviour. The large surface-to-volume ratio and confined thickness to atomic scales offer incredibly high carrier mobility, the feasibility of chemical doping, mechanical flexibility, chemical stability, and optical transparency. This offers new potentials for the development of novel sensors and superior energy conversion and storage devices. Inspired by graphene, TMDs and TMOs have also been exfoliated and studied. Even though the excellent electrical conductivity of graphene makes it a transparent conductor, its zero bandgap limits its technological applications in electronic devices. However, TMDs (e.g., MoS_2) and TMOs (e.g., SnO) have a finite bandgap and therefore exhibit semiconducting behaviour. However, the exfoliation and the growth processes can make defects and impurities in 2D layers, which can alter their electronic properties. For example, in the SnO, exfoliated SnO monolayers the bandgap is wide as compared to layered structure because of the lack of electron lone pair interactions between the layers [45]. The defects form during the growth and can be tailored using adatoms like boron, carbon, nitrogen, oxygen, and fluorine, which can vary the number of valence electrons and therefore their transport properties.

Nanoribbons (NR) are flat 2D materials with a characteristic width of a few atoms, which are made up of a single or a few atoms thick lamellar crystals. Because of their narrow width edges are significant, and nanoribbons possess unusual optical and optoelectronic properties. We can vary these properties using different methods such as doping, selective functionalisation, applying external electrical/magnetic field or mechanical strain [46]. One of the widely used methods to obtain graphene nanoribbons is unzipping of CNT [47].

The characteristic width of NR is around 10 nanometers. Depending on the edge structure, non-chiral graphene nanoribbon (GNR) can be divided into two groups: armchair and zigzag. The principal difference in both shapes is defined by 30 degrees shift in their cutting direction. According to the classical nomenclature, the armchair shaped edges are characterised by the number of dimer lines (N_A) across the ribbons (Fig. 3(a)). On the other hand, the elemental pieces of the zigzag-like structure are zigzag chains (N_Z) (Fig. 3(b)) [48]. These two terminations make a clear difference between 2D graphene and NRs, simultaneously, giving rise to quantum confinement effect.

There have been only a few experimental studies on large 2D sheets and nanowalls, some of which are given in references [38,49,50]. It is difficult to investigate these materials because of their complicated synthesis and manipulation of the growth process. The main question is how to adapt their properties for implementation in the next generation nanoelectronics and also for advanced quantum computational devices. In the case of graphene, one approach to modifying its gapless nature is to transform them into narrow ribbons and thus obtain a finite energy gap. Graphene nanoribbons (GNRs) also show a local resonance within the energy gap. Because of

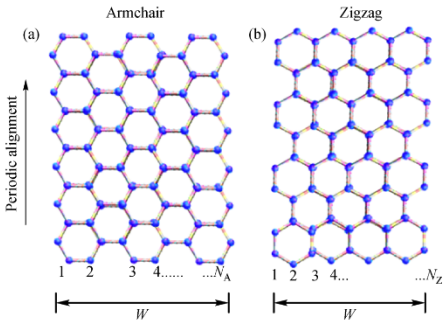

Fig. 3 Typical geometries of nanoribbons edges. (a) Armchair type arrangement: N_A is the number of dimers; (b) Zigzag type alignment: N_Z is the number of elements in the chains and W is the characteristic width [48]

that, the transport is carried out by the hopping of charge carriers through a quantum dot series [51]. A lot of theoretical studies were done on the transport mechanisms in GNRs. In nanoribbons, with width under a few nanometers, quantum confinement and edge effect are important and lead to exciting semiconducting features [52]. Earlier studies found that the armchair edged GNRs were typically semiconductors with gap size being inversely proportional to the ribbon width [53]. Quite the opposite happens with the zigzag edged GNRs (ZGNRs) in which metallic behaviour is linked to the localised edge states near the Fermi level. Later, the existence of a small bandgap in symmetric ZGNRs under bias voltage was also found by Li et al. [54]. Similar studies have been performed on phosphorene and bismuth nanoribbons [55,56]. The structure and chemical termination of the edges influence the charge carrier transport and thereby also device operation. The bonding characteristics between atoms change sharply at the edges, which can be used for functionalisation. Various nano-fabrication strategies including top-down and bottom-up strategies were adopted to realise nanoribbon structures in the sub-50 nm and even the sub-10 nm scale. From experimental observations of electrical properties like charge transport, edge disordered localisation and opening energy gaps can be explained as follows: (a) Transport behaviour due to intrinsic scattering, photon scattering, and impurity scattering. In general, the room temperature charge transport in nanoribbons is limited by intrinsic phonon scattering from the supporting substrate, impurity scattering, and edge roughness scattering [57,58]. It was reported that the carrier mobility starts to decrease when the ribbon width shrinks, because of the effect of the line edge roughness scattering [59,58]. Significantly smaller mobilities in chemically derived GNRs (200 $cm^2 \cdot V^{-1} \cdot s^{-1}$ with a ribbon width of 2 nm) [60] were observed due to rough edges. In the top-gated graphene-nanoribbon transistors made of 15-nm width GNRs etched with 50-nm ZrO_2 nanowires, the hole mobility was found to be of 1310 $cm^2 \cdot V^{-1} \cdot s^{-1}$, which is one of the highest values realised in GNR devices [61]. Until now, the influence of edge structure on the electronic properties of GNRs could only be verified with the study of the local density of states [62], which showed the existence of energy gaps for predominantly armchair-edged nanostructures. The width of the energy gaps decreases with increase in the ratio of zigzag versus armchair edges N_Z/N_A [63]. Figure 4 displays three possible ways of edge scattering: (1) Diffusive edge DE: the electrons are bouncing back and forth between the two edges, with a coefficient of the probability of being diffusely scattered P; (2) Structural edge-roughness SER: in this case, the ribbon edge structure is not uniform. Thus, the appropriate model, which describes the mobility degradation, has to be accompanied by width variations of the ribbons;

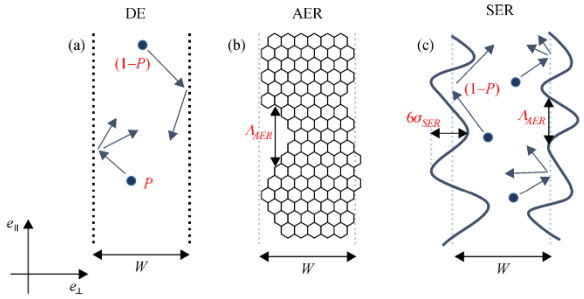

Fig. 4 Schematic representation of edge scattering mechanisms in graphene NRs. (a) DE-diffusive edge scattering; (b) Atomistic edge-roughness scattering; (c) Structural edge-roughness scattering. The coefficients are defined as follows: P is a probability collision coefficient, σ_{SER} is a standard width deviation, Λ_{SER} is SER correlation length, Λ_{AER} is AER correlation length, W is the characteristic width [64]

(3) Atomistic edge-roughness AER: the model is based on a modification of the nanoribbon edge by adding or subtracting one row of carbon atoms on each side [64]. (b) Edge roughness induced localisation effect. The transfer of electron wave function can be primarily hindered due to the quasi-one-dimensional Anderson localisations which are induced by edge disordering. That is, the suppression of conductivity near the charge neutrality point would occur with moderate edge roughness [65]. The calculation of the local density of states shows that the edge disorder can produce a strong enhancement of the electron density at the edge to form surface like localised states which do not participate in the charge transport [66]. The extracted localisation length depends on the disorder type. It decreases with the increase of disorder amplitude and with the reduction of ribbon width. Also, the localisation length reaches its minimum when the energy level approaches the Dirac point, resulting in enlarged transport gaps. A transport gap would develop where all the conducting channels were suppressed with the increasing disorder probability and ribbon length. The Anderson localisation induced transport bandgap was found not only in the edge-disordered armchair nanoribbons but also in the zigzag arranged NRs. The suppression of orientation effect was also predicted with the intensive disorder in which two rows of edge atoms were involved [67]. (c) Coulomb blockade effect. Another critical factor to be considered is the Coulomb blockade effect, which is due to the trapping of electrons on an island due to its charging effect under certain voltage conditions. It confirms the existence of a potential which is non-uniform, and it is associated with the quantum confinement of the carriers along the ribbon. This effect also prevents the Klein tunnelling processes [68] and creates a region of reduced conductivity inside. This effect was first observed in graphene quantum dot structure fabricated by e-beam lithography, in which a graphene island functioned as a quantum dot, while the bulk graphene served as electrodes and the graphene necks with a reduced width in between served as the tunnelling barriers [69,70]. Similar to this quantum dot structure formed by width tailoring, nanoribbons with large edge roughness may also undergo such dot-neck segregation. Therefore, they can be modelled as multiple graphene quantum dots in a series. Moreover, multiple Coulomb blockade effect was expected at low temperature. Sols and co-workers calculated the transport behaviour of edge disordered GNRs due to the Coulomb blockade effect [51]. Their result indicated that the Coulomb charging energy could open up an energy gap at low temperature.

The general idea of the Coulomb charge blocking effect in graphene nanoribbons is similar to the working principle of one electron transistor with two junctions. In the case of 2D NRs, the origin of reduction in conductance can be attributed to the localised charged defects (dots or necks) or the bandgap transformations [71]. Taking into account that the band structure is an inner property of the material, the energy gap rises due to electron-electron interaction and additionally supported by randomly localised charge carriers. In (Fig 5(a)) the typical trend of

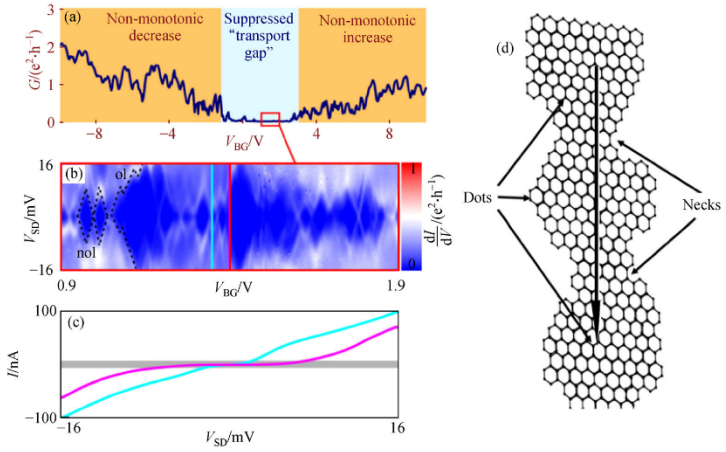

Fig. 5 Electric properties of graphene nanoribbons. (a) The low-temperature conductance of NR nanoribbons versus of applied gate voltage; (b) Conductance behaviour inside of the selected region; (c) Electrical current versus of applied bias voltage along two marked lines; (d) Dot-neck structure in disordered graphene nanoribbons. The disordered edge leading to the formation of dots and necks, where Coulomb-blockade takes place when the charge moves from one dot another [71]

the low-temperature conductance versus applied back voltage of graphene NRs is displayed. There are three different zones which can be considered. Those two regions coloured by orange represent a transition mode, where the electrons have higher energy than a certain barrier value that allows tunnelling through it. The middle grey region with suppressed current flow clearly demonstrates the Coulomb blockade effect. In this regime, the applied back gate voltage is too low. Thus, the energy of the electrons does not exceed the barrier value making impossible tunnelling processes. As a result, the conductance reaches its minimum. This effect can be visualised by plotting the differential conductance dI/dV_{SD}. The observed blue rhombuses are known as 'Coulomb diamonds' (Fig. 5(b)). Figure 5(c) presents the cross-section of the current flow as a function of applied bias voltage V_{SD} [71]. The Coulomb-blockade effect in nanoribbons is directly attributed to the roughness at the ribbon edges of the dot-neck structure as presented in Fig. 5(d). This roughness occurs naturally and leads to the charge localisation at the edges. Therefore, the formation of necks causes an abrupt reduction of the conducting channels and a significant increase in the impedance along the sheet. Due to this the conductance drastically drops to zero while approaching the charge-neutrality point even in the absence of a true bandgap. It ends up in the isolation of nanoscale size regions-dots. Inside this dot regions, the electrons are temporarily confined and Coulomb-blockade results from the electron transport in dot-to-dot through graphene necks.

The edge dominated carbon nanostructures can, therefore, possess a zero or non-zero bandgap, exhibiting metallic or semiconducting behaviour. Altering of a bandgap width allows creating new low dimensional materials with diverse electronic properties.

4 Tailoring of conductivity of two-dimensional materials

The demand for better electrical properties and simplification of nano-based devices requires the development of advanced 2D materials [72]. Tailoring these type of structures started by combining the building blocks and turning them into complex architectures [73]. To achieve the desired electrical, structural, optical and chemical properties, different approaches were used, like micromechanical exfoliation [21]. Most of these adjustments were successful in graphene and other 2D materials like MoS_2 [21,25]. The conductivity and transport properties are associated with the material bandgap, which should be introduced without compromising other properties. Various strategies of a bandgap opening in 2D materials like graphene are discussed below.

4.1 Quantum confinement in graphene nanoribbons

Graphene is a very suitable material for future nanoelectronics, which could replace even silicon and conductive interconnects. However, it is only useful after the bandgap is induced in its electronic structure. This bandgap can, for example, be effectively achieved by nanoribbon formation and quantum confinement of electrons. Unlike in a large area graphene, the electrons in quasi-one-dimensional nanoribbons (formed from 2D graphene sheets) are confined in a single dimension and make a finite bandgap semiconductor similar to carbon nanotubes. The theoretical model of nanoribbons was initially developed by Nakada et al. in their study of the edge effect. They proposed a possibility that the π electrons can exhibit a special electronic state near to the Fermi level, which would affect the electrical properties. They also demonstrated mathematically that carrier mobility and charge scattering are only expected at the edges [74]. In another work, Wakabayashi studied the electronic transport properties through nanographite ribbon junctions connecting two zigzag ribbons with same or different width by the Landauer-Buttiker approach using a tight-binding model. They found the conductivity is associated with a quasi-bound state in the scattering regions of the junctions, yielding the formation of standing waves [75]. They extended there work in the electronic states of graphite ribbons with edges of two typical shapes; armchair (Fig. 6) and zigzag, by performing tight binding band calculations. They found that the graphite ribbons exhibit the striking contrast in the electronic states depending on the edge shape [76]. Later, it was found that the graphene nanoribbons (GNRs) with a width greater than 10 nm have a finite bandgap as well as notable carrier mobility and thus high switching ratios [77]. Berger et al. demonstrated the nanoribbon geometry and electronic confinement along with coherence and Dirac nature of the carriers [78]. Ponomarenko et al. [69] also described the nanoribbons in quantum dot geometry. However, the semiconducting properties of GNRs below 10 nm would reduce the limitations of the SWCNTs due to their chirality dependence. Moreover, metallic GNRs have high current carrying capacity, and better conductive interconnects than CNTs.

4.2 Chemical substitution doping

Chemical substitution doping is a popular method in semiconductor engineering. Many theoretical and several experimental studies for opening up a bandgap were performed in graphene by substitution of a carbon atom by nitrogen [79–86], boron [80,87–89] and combination of them [90,91]. It was found that semimetallic graphene behaviour has been changed to semiconducting one under substitution of carbon by Al or B atoms in a lattice [92].

Nitrogen doping in graphene converts the material into a *p*-type semiconductor. Nitrogen doping has also been established in ZGNRs by CVD process, where it was noticed that at the ribbon edge the dopant atoms prefer to be as far from each other as possible [79]. However, the carrier mobility was significantly lower than expected because of some defects created by the doping.

Doping of a boron atom as a substitution for a graphitic carbon atom is also possible. The presence of a boron atom in the lattice could improve the oxidation resistance of the graphitic carbon, because of the change in the density distribution of the high energy charge carriers [87]. The enhancement of the oxidation resistance is due to the reduction in electron density, which reduces the number of activation sites [87]. In Fig. 6(a), the typical honeycomb alignment of the graphene layer is presented, where one atom of carbon in a matrix is replaced by boron one. Taking into consideration that boron atoms are less electronegative, this doping results in a downward shift of the Fermi level of graphene Fig. 6(b). The boron graphene structure reveals *p*-type semiconducting features with charge particle mobility found to be about 800 $cm^2 \cdot V^{-1} \cdot s^{-1}$. As well as the dopant type (nitrogen or boron), the concentration of dopants and the number of layers of graphene are also major factors which affect the bandgap opening. These changes in bandgap energy (E_g) concerning the concentrations of different dopant atoms are observed from Fig. 6(c).

4.3 Substrate-induced bandgap opening

The scanning tunnel microscope (STM) and scanning tunnel spectroscopy report on bandgap opening in graphene was published in [95]. Epitaxial graphene and *h*-BN also have an experimentally reported bandgap. Experiments using Ni substrate induced a bandgap of 0.5 eV into graphene/*h*-BN hybrid. DFT simulations approach predicted that graphene on bulk *h*-BN and epitaxial grown graphene on copper could induce small changes of bandgap [96]. Moreover, the graphene deposited on SiO_2 developed a bandgap of 0.52 eV [97]. More recently, bandgap opening in epitaxial graphene by SiC was reported [98]. The viability of the growth process of the 2D material and the interaction between the substrate is also interesting. However, the graphene on SiC substrate exhibited *n*-type doping, and the Fermi level shifted above the bandgap. In order to make it a semiconductor, the Fermi level has to move inside the bandgap either by hole doping or by applying a gate voltage [98].

Figure 7 presents the data obtained from angle-resolved

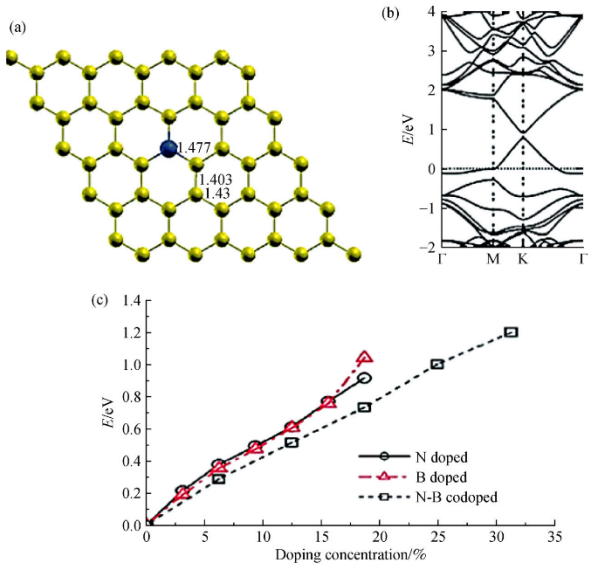

Fig. 6 The effect of the lattice atoms replacement in graphene. (a) Substitution of boron B (blue ball) in graphene; (b) Band structure of a single B-substituted graphene sheet (reproduced with permission from [93]); (c) Variation of the energy gap E_g under N and B atoms substitution, and N–B pair doping concentrations (reproduced with permission from [94])

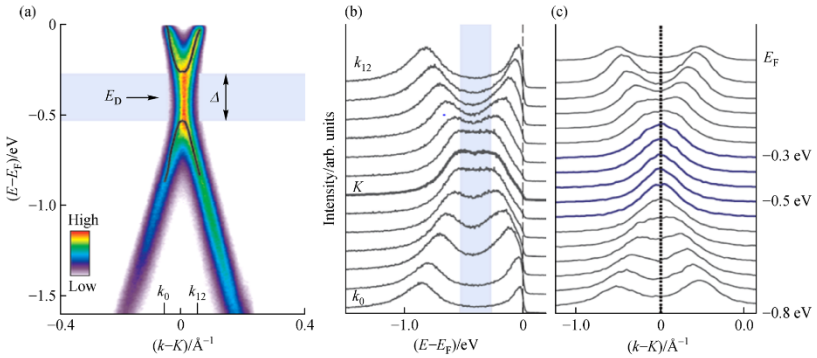

Fig. 7 ARPES intensity maps showing substrate-induced bandgap opening in graphene on SiC. (a) Photoelectron intensity as a function of energy and momentum, for a line through one of the K points; (b) EDC curves showing the dispersion of energy at the K point; (c) MDC showing the no-dispersive peaks at the gap region (Reprinted with permission from the reference [98])

photoemission spectroscopy (ARPES) taken for a line through one of the Dirac points E_D of a single layer graphene on SiC substrate [98]. The photoelectron intensity as a function of energy and the momentum, shown in (Fig. 7(a)), exhibits a dispersion at E_D, that is a characteristic feature of electron-doped graphene. As a result, the valence band and the conduction band are separated by specific energy at the K point. The energy distribution curves (EDCs) demonstrate two peaks at the K point with a minimum energy separation (Fig. 7(b)). In the same energy window, in momentum distribution curves (MDCs) peaks are appearing as non-dispersive (Fig. 7(c)). This supports the existence of a finite bandgap with a conical dispersion. It indicates that the SiC substrate induces the bandgap in epitaxial graphene. Thus, the interaction between the substrate and the graphene layer breaks the sublattice symmetry, leading to a bandgap opening.

4.4 Hybrids

As discussed above, a lot of theoretical studies were carried out for the doping of graphene-like 2D materials with boron and nitrogen to form hybrid structures like BCN (graphene-like boron-carbon-nitrogen monolayers) [99, 100]. Some experimental works reported successful synthesis of BCN materials. BCN atomic hybrids layers with B, C and N contaminants, obtained with the assistance of CVD can exhibit semiconducting behaviour [101]. Quantum molecular dynamics and density functional theory were employed to investigate the structural and electronic properties of carbon and boron nitride sandwich-type hybrid nanoribbons [102]. Structurally stable hybrid systems that behave as semimetals were formed by stacking two zigzag graphene nanoribbons, two zigzag boron nitride nanoribbons [103]. The ZGNRs, which are sandwiched between *h*-BNs, remain in the interfaces of boron nitride sheets and exhibit promising electronic and magnetic properties. The GNRs embedded in boron nitride sheets are potential low-dimensional materials for electronic-spintronic nanodevices [104,105]. The possible applications are further discussed in the next section. The synthesis of large area 2–3 atomic layered graphene films and *h*-BN domains on Cu substrates by chemical vapour deposition also provide a small bandgap opening. Further theoretical investigations predict the increase in a bandgap width with *h*-BN domain size reduction [90]. Hybrid films with tunable and optical properties are therefore prospective candidates for field emission devices [106]. Although the above-discussed methods sound promising, the control over the shape and the domain size is still an unsolved issue. This is essential for the tuning of the bandgap and electronic properties. Thus, a novel method should be introduced for the synthesis and modification of the low-dimensional materials.

5 Plasma tailoring for edge electronics and device fabrication

Plasma-assisted techniques are a perspective method which enables property-tuning with the reaction parameters. In particular, they can assist in synthesising nanostructures and tailoring their physical properties. Moreover, large-scale growth of edge dominated carbon nanostructures (like carbon nanowalls) at low temperature and pressure is possible using plasma-assisted techniques. Beside this, a simple plasma modification of materials, frequently used in microelectronics, offers new possibilities for tailoring 2D material properties, which can lead to

the rise of edge electronics. The possibilities of tailoring material vacancies, adatoms like gold, and the exchange of single atoms and the modifications of grain boundaries will induce a reasonable change in electrical conductivity and transport behaviours [107,108]. Some of these remarkable modifications with plasma generated in different gases, which are used to enhance the electrical properties of 2D nanomaterials are discussed here and summarised in Table 2.

Plasma-assisted nitrogen functionalisation enhances the electrical properties by lowering the work function of electrons in nanomaterial. Apart from this, modifications can also be done to the structures like nanowalls or nanoribbons, in order to implement those into nanodevices like field effect transistors [77]. In 2008, Stampfer et al. fabricated a fully tunable graphene single electron transistor based on an etched-width-modulated graphene nanostructure [123]. In this case, N_2 plasma was used to reduce the work function of material from 4.91 to 4.37 eV [124]. Similarly, a controlled edge nitrogen functionalisation can also be done with NH_3 plasma. A result of such nitrogen incorporation process increases the nanomaterial specific capacitance (280 F/g), which can enable the preparation of electrodes for novel ultra-supercapacitors [125].

Furthermore, the processing with O_2 plasma causes the bandgap opening and thereby increased material responses towards electrochemical activities, which can be used in optoelectronic devices, actuators and patterning of flexible transparent electrodes [126–128]. Simultaneous reduction and defect restoration of graphene oxide nanoribbon (GONR) via plasma-assisted chemistry was demonstrated by Chiang et al. [129]. When H_2 and CH_4 gases are used, the atomic hydrogen or/and carbon-containing ions and radicals are generated by molecule dissociation and ionisation in plasma. Such plasmas are convenient for removal of oxygen atoms or oxygen functional groups like in the case of GONR films. The synergistic effect of simultaneous reduction and defect restoration on GONR was achieved with the plasma gas mixture H_2/CH_4 treatment [130,131]. The results of this study indicate that the optical energy gap of the treated reduced-GONR (r-GONR) can be engineered by controlling the plasma exposure time. Furthermore, the conductivity of the GONR can be enhanced as well. This unique plasma reduction is characterised by short processing times, high purity of obtained nanomaterial and low temperature compared with conventional thermal and chemical reductions. Therefore such non-equilibrium chemical processing approach can be used more widely beyond the mere reduction of GONR and graphene oxide (GO).

Similarly to graphene, numerous investigations were performed in 2D heterostructured MoS_2, one of the most promising candidates for field effect transistors (FET), where the influence of point defects, dislocations, grain boundaries are considered [132–134]. Liu et al. [135] investigated the defects and the electronic band structure in MoS_2 and showed that the sulphur vacancies lead to the pinning of Fermi level near the conduction band. The defect formed by the sulphur vacancies induced an *n*-type behaviour in MoS_2. Later, Qiu et al. [136] confirmed this effect by introducing localised electron donor states inside the bandgap. Hong et al. reported a low-temperature doping method [137] for reparation of the sulphur vacancies in MoS_2 layers. Islam et al. described tuning of electrical properties via defect engineering using oxygen

Table 2 Plasma-assisted tailoring of 2D materials for electrical properties and their applications

Carrier gas	Change in material	Applications
NH_3	Yielding graphene quantum nanosheets [109]	Gas sensors
N_2/H_2	Incorporation of nitrogen preferably at the edges [110]	FETs
N_2/O_3	Defect generation	Supercapacitors
O_2	Control of thermal boundary conductance [111] Narrowing the bandgap from 6.0 eV to 4.3 eV (in *h*-BN) [112] Sulphur vacancy engineering in MoS_2 [113]	Lithium batteries
Ar/O_2	Wettability and surface energy [114]	
Ar/H_2	Conversion of sp^2 to sp^3 hybridisation (opening a bandgap of 3.5 eV) [115], defects and disorder generation	
C_3H_9B	*p*-Type conductivity with an on-off ratio of 10^2 [116], tunable bandgap ranging from 0 to ~0.54 eV	Rectifying diodes
CF_4 SF_6 Ar/SF_6 CHF_3	*p*-Type doping for gas sensing (e.g., NH_3) [117]	Back-gated FETs Multi-bit memory transistors Photodiodes Hydrogen production
Cl_2	*p*-Type doping increases carrier mobility [118]	Sensors
H_2	*p*-Type doping in MoS_2 [119], reverse fluorination in WS_2 [117]	Photovoltaic devices
CH_4	The transition of insulating to semiconducting [120]	
PH_3/He	Minimised etching and low damage [121]	
N_2	Substitution of sulphur with nitrogen in MoS_2 [122]	

plasma [138]. Further experiments [127,139,140] revealed that plasma could play an important role in surface functionalisation, exchange of atoms and bandgap opening, as described before. The current state-of-the-art in plasma surface tailoring is presented in Table 2. The table summarises potential plasmas generated from proposed gas or gas mixtures for modification of 2D materials and their applications in functionalised nanoelectronics devices.

Doping with boron is done with boron-containing plasma typically generated in gases or vapours. An example of such process is doping of the zigzag edged graphene nanoribbons [141]. The obtained nanoribbons exhibit a half-metallicity beyond the particular electric field, which can lead to potential applications in spintronics and semiconductor devices [88]. The armchair nanoribbons, which are substitutionally doped, can be metalised by 7 boron atom clusters (B7). However, this doping achieved merely in small quantities is significant only for very thin 2D structures. Theoretical studies on the doping and transport properties for large area graphene predict that their transport properties are not significantly affected even at 4% doping levels. The quantum interference would be minimised, and thus the carrier mobilities would become more asymmetric only at higher doping values [83]. The experimental investigations of boron and nitrogen doped graphene, which were synthesised in arc discharge of diborane/hydrogen gas mixture [80] confirmed that they exhibit *p*-type and *n*-type semiconducting properties. This behaviour could be systematically tuned by varying the concentrations of boron and nitrogen in the gas mixture. However, the doping of boron creates defects and disorders in graphene layers. This was observed with STM and Raman analyses by Endo et al. [142]. In this context, plasma-assisted techniques are more suitable for the synthesis and defect engineering in graphene sheets as well as in narrow structures like nanoribbons.

When the edge of 2D nanostructures is considered, one can expect different behaviours depending on external influence as well. Taking graphene as a model example, the current flow throughout the two-dimensional plane, as in a regular conductor. This behaviour could be changed with plasma assistance or by applying a magnetic field. Under a magnetic field perpendicular to the graphene plane, the current flows only along the edges in a direction depending on the orientation of the magnetic field [143]. This common phenomenon is often referred to as quantum Hall effect [144]. However, Young et al. came up with an unexpected phenomenon beyond Hall effect [145]. The researchers applied a second powerful magnetic field in the same direction of the graphene flake. The experiment ended up in the electron motion around the edge in any direction (either in clockwise or anticlockwise). In particular, the electrons with one kind of spin move in a clockwise direction and at the same time the electrons with the opposite spins move counter clockwise. That literarily means a conductive edge or a circuit. This also indicates a possibility that 2D nanostructures like graphene can be topological insulators. Unlike in conventional topological insulators, the above-mentioned circuit in graphene can be controlled by varying the magnetic field. Another benefit of this is the inhibition of backscattering, which would interrupt the motion of the electrons. As a result, the imperfections in the material do not affect electron motion, since the electrons can travel along the edges irrespectively. However, the spin-dependent behaviour at the newly developed edge states can be modified with plasma, e.g., doping of gold atoms to the edges. Plasma itself as a tool can selectively dope the material with atoms like gold or nitrogen. In the case of gold, it is expected the conductivity of the material will increase. However, in this case, the inserted atoms would decrease the conductance. The gold atoms added into the graphene edges, namely allow the electrons to backscatter into the oppositely travelling states, and thereby the mixing of the electron spins [145,146]. Moreover, there is also a possibility to control the conductivity along the edges with the concentrations of the gold atoms. The idea for further research is to create the circuit based on edge dominating 2D material, which are, in turn, doped with a noble metal. This can be done by using suitable plasma (Ar or N) in order to incorporate gold atoms into the edges of graphene nanoribbons (see Fig. (8)). And more, under the influence of high magnetic fields with different orientations, a spin depended current flow is expected to be obtained along the edges in the closed electrical circuit designed with Au modified nanoribbons.

However, the device fabrication is another challenge, because the scalable deposition of high-quality Ohmic contacts is a problem that needs to be further improved. Successful strategies *in situ* involve the deposition of pure metal contacts, such as Au and Pd, under ultra-high vacuum or patterning/surface treatment of the area under the contact. It facilitates to create stronger interaction between 2D surface and the metal. Etching of 2D materials is also an issue, but mild plasma-assisted methods would help to solve this problem. Controlled etching of 2D materials is critical to achieving sophisticated device structures such as LEDs, tunnel transistors and for side contacts. The relatively mature technologies, such as plasma, can therefore easily be tuned to etch stacks of 2D layers with profiles for device architecture. The emerging field of Atomic Layer Etching (ALE) of both conventional and 2D materials could contribute to further advances in atomic scale devices. However, all these device fabrication processes are beyond the review of this paper.

6 Conclusions

The mini-review summarises existing efforts on tailoring electrical properties of 2D structured nanomaterials with

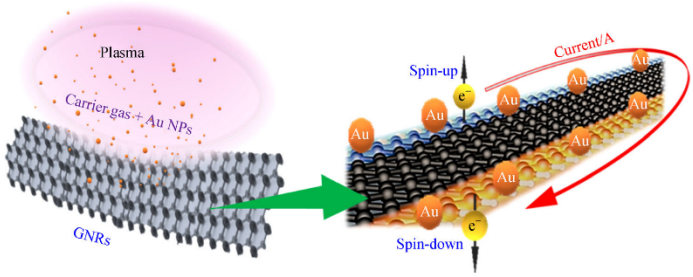

Fig. 8 Schematic representation of graphene NRs edge tailoring with the assistance of plasma for 2D functionalisation electronics. Electrons on the two zigzag edges exhibit opposite directions of rotation (spin)-'spin-down' on the bottom edge or 'spin-up' on the top edge that generates a current flow

plasma chemistry, which are aimed at possible applications of these materials for electrical and optoelectronic devices. Many different plasma techniques have been used for enhancing their conductivity and other electrical properties. In this context, the significance of the surface, as well as the edges of the 2D structures, were studied. Namely, the edges are becoming of utmost significance for designing nanoelectronics. One can tailor these 2D materials and structures like nanoribbons, nanowalls and nanosheets by selective doping of adatoms (metallic or non-metallic) like gold and nitrogen, defect engineering or by applying external magnetic or electric field. Plasma-based methods enable controlled, and selective functionalisation of the selected materials and various plasma species like N_2, O_2, B, etc. Further enhancement of material properties can be achieved by controlling the morphology like the width of nanostructures including nanoribbons and nanowalls. Moreover, plasma can support the growth or synthesis as well as modifications of new 2D hybrid structures. With these processes, we can create new emerging functionalised 2D materials for nanoelectronics, which are featured by quantum conductivity. This will lead to miniaturisation of electrical circuits, which will contribute to engineer high-performance next-generation 2D electronic functional devices with significantly reduced energy consumption. The biggest breakthrough in this, we believe will occur due on edge-dominated 2D nanostructures.

References

1. Tiwari J N, Tiwari R N, Kim K S. Zero-dimensional, one-dimensional, two-dimensional and three-dimensional nanostructured materials for advanced electrochemical energy devices. Progress in Materials Science, 2012, 57(4): 724–803
2. Novoselov K S, Geim A K, Morozov S V, Jiang D, Katsnelson M, Grigorieva I, Dubonos S V, Firsov A A. Two-dimensional gas of massless Dirac fermions in graphene. Nature, 2005, 438(7065): 197–200
3. Dutta S, Pati S K. Novel properties of graphene nanoribbons: A review. Journal of Materials Chemistry, 2010, 20(38): 8207–8223
4. Li Y, Jiang X, Liu Z, Liu Z. Strain effects in graphene and graphene nanoribbons: The underlying mechanism. Nano Research, 2010, 3(8): 545–556
5. Pereira V M, Neto A C. Strain engineering of graphene's electronic structure. Physical Review Letters, 2009, 103(4): 046801
6. Bhimanapati G R, Lin Z, Meunier V, Jung Y, Cha J, Das S, Xiao D, Son Y, Strano M S, Cooper V R, et al. Recent advances in two-dimensional materials beyond graphene. ACS Nano, 2015, 9(12): 11509–11539
7. Mas-Balleste R, Gomez-Navarro C, Gomez-Herrero J, Zamora F. 2D Materials: To graphene and beyond. Nanoscale, 2011, 3(1): 20–30
8. Mak K F, Lee C, Hone J, Shan J, Heinz T F. Atomically thin MoS_2: A new direct-gap semiconductor. Physical Review Letters, 2010, 105(13): 136805
9. Lukowski M A, Daniel A S, English C R, Meng F, Forticaux A, Hamers R J, Jin S. Highly active hydrogen evolution catalysis from metallic WS_2 nanosheets. Energy & Environmental Science, 2014, 7(8): 2608–2613
10. Andriotis A N, Menon M. Tunable magnetic properties of transition metal doped MoS_2. Physical Review B, 2014, 90(12): 125304
11. He J, Hummer K, Franchini C. Stacking effects on the electronic and optical properties of bilayer transition metal dichalcogenides MoS_2, $MoSe_2$, WS_2, and WSe_2. Physical Review B, 2014, 89(7): 075409
12. Wang Q H, Kalantar-Zadeh K, Kis A, Coleman J N, Strano M S. Electronics and optoelectronics of two-dimensional transition metal dichalcogenides. Nature Nanotechnology, 2012, 7(11): 699–712
13. Cao L, Yang S, Gao W, Liu Z, Gong Y, Ma L, Shi G, Lei S, Zhang Y, Zhang S, Vajtai R, Ajayan P M. Direct laser-patterned micro-supercapacitors from paintable MoS_2 films. Small, 2013, 9(17): 2905–2910
14. Huang Y H, Peng C C, Chen R S, Huang Y S, Ho C H. Transport

properties in semiconducting NbS_2 nanoflakes. Applied Physics Letters, 2014, 105(9): 093106

15. Moore D B, Beekman M, Disch S, Zschack P, Häusler I, Neumann W, Johnson D C. Synthesis, structure, and properties of turbostratically disordered $(PbSe)1.18(TiSe_2)_2$. Chemistry of Materials, 2013, 25(12): 2404 2409
16. Jeong S, Yoo D, Jang J T, Kim M, Cheon J. Well-defined colloidal 2-D layered transition-metal chalcogenide nanocrystals via generalized synthetic protocols. Journal of the American Chemical Society, 2012, 134(44): 18233 18236
17. Yu Z, Tetard L, Zhai L, Thomas J. Supercapacitor electrode materials: Nanostructures from 0 to 3 dimensions. Energy & Environmental Science, 2015, 8(3): 702 730
18. Hsu Y K, Chen Y C, Lin Y G, Chen L C, Chen K H. Birnessite-type manganese oxides nanosheets with hole acceptor assisted photoelectrochemical activity in response to visible light. Journal of Materials Chemistry, 2012, 22(6): 2733 2739
19. Geim A K, Grigorieva I V. Van der Waals heterostructures. Nature, 2013, 499(7459): 419 425
20. Eda G, Fujita T, Yamaguchi H, Voiry D, Chen M, Chhowalla M. Coherent atomic and electronic heterostructures of single-layer MoS_2. ACS Nano, 2012, 6(8): 7311 7317
21. Li H, Lu G, Wang Y, Yin Z, Cong C, He Q, Wang L, Ding F, Yu T, Zhang H. Mechanical exfoliation and characterization of single- and few- layer nanosheets of WSe_2, TaS_2, and $TaSe_2$. Small, 2013, 9(11): 1974 1981
22. Li H, Lu G, Yin Z, He Q, Li H, Zhang Q, Zhang H. Optical identification of single- and few- layer MoS_2 sheets. Small, 2012, 8 (5): 682 686
23. Tongay S, Zhou J, Ataca C, Lo K, Matthews T S, Li J, Grossman J C, Wu J. Thermally driven crossover from indirect toward direct bandgap in 2D semiconductors: $MoSe_2$ versus MoS_2. Nano Letters, 2012, 12(11): 5576 5580
24. Wang F, Wang Z, Wang Q, Wang F, Yin L, Xu K, Huang Y, He J. Synthesis, properties and applications of 2D non-graphene materials. Nanotechnology, 2015, 26(29): 292001 1 7
25. Xu Y, Liu Z, Zhang X, Wang Y, Tian J, Huang Y, Ma Y, Zhang X, Chen Y. A graphene hybrid material covalently functionalized with porphyrin: Synthesis and optical limiting property. Advanced Materials, 2009, 21(12): 1275 1279
26. Avouris P. Graphene: Electronic and photonic properties and devices. Nano Letters, 2010, 10(11): 4285 4294
27. Xu C, Xu B, Gu Y, Xiong Z, Sun J, Zhao X S. Graphene-based electrodes for electrochemical energy storage. Energy & Environmental Science, 2013, 6(5): 1388 1414
28. Huang Y, Liang J, Chen Y. An overview of the applications of graphene-based materials in supercapacitors. Small, 2012, 8(12): 1805 1834
29. Lv W, Li Z, Deng Y, Yang Q H, Kang F. Graphene-based materials for electrochemical energy storage devices: Opportunities and challenges. Energy Storage Materials, 2016, 2(1): 107 138
30. Fratini S, Guinea F. Substrate-limited electron dynamics in graphene. Physical Review B, 2008, 77(19): 195415
31. Prezzi D, Eom D, Rim K T, Zhou H, Lefenfeld M, Xiao S, Nuckolls C, Heinz T F, Flynn G W, Hybertsen M S. Edge structures for nanoscale graphene islands on Co (0001) surfaces. ACS Nano, 2014, 8(6): 5765 5773
32. Liu H, Zhang X, Zhai T, Sander T, Chen L, Klar P J. Centimeter-scale-homogeneous SERS substrates with seven-order global enhancement through thermally controlled plasmonic nanostructures. Nanoscale, 2014, 6(10): 5099 5105
33. Israr-Qadir M, Jamil-Rana S, Nur O, Willander M, Larsson L A, Holtz P O. Fabrication of ZnO nanodisks from structural transformation of ZnO nanorods through natural oxidation and their emission characteristics. Ceramics International, 2014, 40(1): 2435 2439
34. Wang H, Guo Z, Wang S, Liu W. One-dimensional titania nanostructures: Synthesis and applications in dye-sensitized solar cells. Thin Solid Films, 2014, 558: 1 19
35. Yu X Y, Feng Y, Guan B, Lou X W D, Paik U. Carbon coated porous nickel phosphides nanoplates for highly efficient oxygen evolution reaction. Energy & Environmental Science, 2016, 9(4): 1246 1250
36. Peng L, Feng Y, Bai Y, Qiu H J, Wang Y. Designed synthesis of hollow Co_3O_4 nanoparticles encapsulated in a thin carbon nanosheet array for high and reversible lithium storage. Journal of Materials Chemistry. A, Materials for Energy and Sustainability, 2015, 3(16): 8825 8831
37. Karakouz T, Holder D, Goomanovsky M, Vaskevich A, Rubinstein I. Morphology and refractive index sensitivity of gold island films. Chemistry of Materials, 2009, 21(24): 5875 5885
38. Hiramatsu M, Shiji K, Amano H, Hori M. Fabrication of vertically aligned carbon nanowalls using capacitively coupled plasma-enhanced chemical vapor deposition assisted by hydrogen radical injection. Applied Physics Letters, 2004, 84(23): 4708 4710
39. Kargar A, Jing Y, Kim S J, Riley C T, Pan X, Wang D. ZnO/CuO heterojunction branched nanowires for photoelectrochemical hydrogen generation. ACS Nano, 2013, 7(12): 11112 11120
40. Terrones H, Lv R, Terrones M, Dresselhaus M S. The role of defects and doping in 2D graphene sheets and 1D nanoribbons. Reports on Progress in Physics, 2012, 75(6): 062501
41. Zhang X, Wang X B, Wang L W, Wang W K, Long L L, Li W W, Yu H Q. Synthesis of a highly efficient BiOCl single-crystal nanodisk photocatalyst with exposing {001} facets. ACS Applied Materials & Interfaces, 2014, 6(10): 7766 7772
42. Gao R, Yin L, Wang C, Qi Y, Lun N, Zhang L, Liu Y, Kang L, Wang X. High-yield synthesis of boron nitride nanosheets with strong ultraviolet cathodoluminescence emission. Journal of Physical Chemistry C, 2009, 113(34): 15160 15165
43. Inamdar A I, Kim J, Jo Y, Woo H, Cho S, Pawar S M, Lee S, Gunjakar J, Cho Y, Hou B, et al. Highly efficient electro-optically tunable smart-supercapacitors using an oxygen-excess nanograin tungsten oxide thin film. Solar Energy Materials and Solar Cells, 2017, 166: 78 85
44. Qu Y, Shao M, Shao Y, Yang M, Xu J, Kwok C T, Shi X, Lu Z, Pan H. Ultra-high electrocatalytic activity of VS_2 nanoflowers for efficient hydrogen evolution reaction. Journal of Materials Chemistry. A, Materials for Energy and Sustainability, 2017, 5 (29): 15080 15086
45. Tao J, Guan L. Tailoring the electronic and magnetic properties of monolayer SnO by B, C, N, O and F adatoms. Scientific Reports, 2017, 7: 44568

46. Terrones M, Botello-Méndez A R, Campos-Delgado J, López-Urías F, Vega-Cantú Y I, Rodríguez-Macías F J, Elías Arriaga A L, Muñoz-Sandoval E, Cano-Márquez A G, Charlier J C, et al. Graphene and graphite nanoribbons: Morphology, properties, synthesis, defects and applications. Nano Today, 2010, 5(4): 351 372
47. Kosynkin D V, Higginbotham A L, Sinitskii A, Lomeda J R, Dimiev A, Price B K, Tour J M. Longitudinal unzipping of carbon nanotubes to form graphene nanoribbons. Nature, 2009, 458 (7240): 872 876
48. Li L. Epitaxial Graphene on SiC(0001): More Than Just Honeycombs, Physics and Applications of Graphene-Experiments. Sergey M, ed. Rijeka: InTech Europe, 2011, 55 72
49. Lee Y H, Zhang X Q, Zhang W, Chang M T, Lin C T, Chang K D, Yu Y C, Wang J T, Chang C S, Li L J, et al. Synthesis of large-area MoS_2 atomic layers with chemical vapor deposition. Advanced Materials, 2012, 24(17): 2320 2325
50. Zhao J, Pei S, Ren W, Gao L, Cheng H M. Efficient preparation of large-area graphene oxide sheets for transparent conductive films. ACS Nano, 2010, 4(9): 5245 5252
51. Sols F, Guinea F, Neto A C. Coulomb blockade in graphene nanoribbons. Physical Review Letters, 2007, 99(16): 166803
52. Jiao L, Zhang L, Wang X, Diankov G, Dai H. Narrow graphene nanoribbons from carbon nanotubes. Nature, 2009, 458(7240): 877 880
53. Bai J, Huang Y. Fabrication and electrical properties of graphene nanoribbons. Materials Science and Engineering R Reports, 2010, 70(3-6): 341 353
54. Li Z, Qian H, Wu J, Gu B L, Duan W. Role of symmetry in the transport properties of graphene nanoribbons under bias. Physical Review Letters, 2008, 100(20): 206802
55. Boutahir M, El Majdoub S, Rahmani A H, Fakrach B, Chadli H, Rahmani A. Electronic properties of phosphorene nanoribbons. Energy Procedia, 2017, 139: 207 210
56. Ning W, Kong F, Xi C, Graf D, Du H, Han Y, Yang J, Yang K, Tian M, Zhang Y. Evidence of topological two-dimensional metallic surface states in thin bismuth nanoribbons. ACS Nano, 2014, 8(7): 7506 7512
57. Liang G, Neophytou N, Nikonov D E, Lundstrom M S. Performance projections for ballistic graphene nanoribbon field-effect transistors. IEEE Transactions on Electron Devices, 2007, 54 (4): 677 682
58. Chen J H, Jang C, Adam S, Fuhrer M S, Williams E D, Ishigami M. Charged-impurity scattering in graphene. Nature Physics, 2008, 4 (5): 377 381
59. Obradovic B, Kotlyar R, Heinz F, Matagne P, Rakshit T, Giles M D, Nikonov D E. Analysis of graphene nanoribbons as a channel material for field-effect transistors. Applied Physics Letters, 2006, 88(14): 142102
60. Wang X, Ouyang Y, Li X, Wang H, Guo J, Dai H. Room-temperature all-semiconducting sub-10-nm graphene nanoribbon field-effect transistors. Physical Review Letters, 2008, 100(20): 206803
61. Liao L, Bai J, Lin Y C, Qu Y, Huang Y, Duan X. High-performance top-gated graphene-nanoribbon transistors using zirconium oxide nanowires as high-dielectric-constant gate dielectrics. Advanced Materials, 2010, 22(17): 1941 1945
62. Tapasztó L, Dobrik G, Lambin P, Biró L P. Tailoring the atomic structure of graphene nanoribbons by scanning tunnelling microscope lithography. Nature Nanotechnology, 2008, 3(7): 397 401
63. Özyilmaz B, Jarillo-Herrero P, Efetov D, Kim P. Electronic transport in locally gated graphene nanoconstrictions. Applied Physics Letters, 2007, 91(19): 192107
64. Yazdanpanah A, Pourfath M, Fathipour M, Kosina H, Selberherr S. A numerical study of line-edge roughness scattering in graphene nanoribbons. IEEE Transactions on Electron Devices, 2012, 59(2): 433 440
65. Gunlycke D, Areshkin D A, White C T. Semiconducting graphene nanostrips with edge disorder. Applied Physics Letters, 2007, 90 (14): 142104
66. Evaldsson M, Zozoulenko I V, Xu H, Heinzel T. Edge-disorder-induced Anderson localization and conduction gap in graphene nanoribbons. Physical Review. B, 2008, 78(16): 161407
67. Querlioz D, Apertet Y, Valentin A, Huet K, Bournel A, Galdin-Retailleau S, Dollfus P. Suppression of the orientation effects on bandgap in graphene nanoribbons in the presence of edge disorder. Applied Physics Letters, 2008, 92(4): 042108
68. Gutiérrez C, Brown L, Kim C J, Park J, Pasupathy A N. Klein tunnelling and electron trapping in nanometre-scale graphene quantum dots. Nature Physics, 2016, 12(11): 1069
69. Ponomarenko L A, Schedin F, Katsnelson M I, Yang R, Hill E W, Novoselov K S, Geim A K. Chaotic Dirac billiard in graphene quantum dots. Science, 2008, 320(5874): 356 358
70. Stampfer C, Güttinger J, Molitor F, Graf D, Ihn T, Ensslin K. Tunable Coulomb blockade in nanostructured graphene. Applied Physics Letters, 2008, 92(1): 012102
71. Bischoff D, Varlet A, Simonet P, Eich M, Overweg H C, Ihn T, Ensslin K. Localized charge carriers in graphene nanodevices. Applied Physics Reviews, 2015, 2(3): 031301
72. Novoselov K S, Geim A K, Morozov S V, Jiang D A, Zhang Y, Dubonos S V, Grigorieva I V, Firsov A A. Electric field effect in atomically thin carbon films. Science, 2004, 306(5696): 666 669
73. Novoselov K S, Neto A C. Two-dimensional crystals-based heterostructures: Materials with tailored properties. Physica Scripta, 2012, T146: 014006
74. Nakada K, Fujita M, Dresselhaus G, Dresselhaus M S. Edge state in graphene ribbons: Nanometer size effect and edge shape dependence. Physical Review. B, 1996, 54(24): 17954
75. Wakabayashi K. Electronic transport properties of nanographite ribbon junctions. Physical Review. B, 2001, 64(12): 125428
76. Fujita M, Wakabayashi K, Nakada K, Kusakabe K. Peculiar localized state at zigzag graphite edge. Journal of the Physical Society of Japan, 1996, 65(7): 1920 1923
77. Li X, Wang X, Zhang L, Lee S, Dai H. Chemically derived, ultrasmooth graphene nanoribbon semiconductors. Science, 2008, 319(5867): 1229 1232
78. Berger C, Song Z, Li X, Wu X, Brown N, Naud C, Mayou D, Li T, Hass J, Marchenkov A N, et al. Electronic confinement and coherence in patterned epitaxial graphene. Science, 2006, 312 (5777): 1191 1196
79. Wei D, Liu Y, Wang Y, Zhang H, Huang L, Yu G. Synthesis of *N*-

doped graphene by chemical vapor deposition and its electrical properties. Nano Letters, 2009, 9(5): 1752 1758

80. Panchakarla L S, Subrahmanyam K S, Saha S K, Govindaraj A, Krishnamurthy H R, Waghmare U V, Rao C N R. Synthesis, structure, and properties of boron- and nitrogen- doped graphene. Advanced Materials, 2009, 21(46): 4726 4730
81. Yu S S, Zheng W T, Wen Q B, Jiang Q. First principle calculations of the electronic properties of nitrogen-doped carbon nanoribbons with zigzag edges. Carbon, 2008, 46(3): 537 543
82. Li Y, Zhou Z, Shen P, Chen Z. Spin gapless semiconductor–metal–half-metal properties in nitrogen-doped zigzag graphene nanoribbons. ACS Nano, 2009, 3(7): 1952 1958
83. Lherbier A, Blase X, Niquet Y M, Triozon F, Roche S. Charge transport in chemically doped 2D graphene. Physical Review Letters, 2008, 101(3): 036808
84. Zheng X H, Rungger I, Zeng Z, Sanvito S. Effects induced by single and multiple dopants on the transport properties in zigzag-edged graphene nanoribbons. Physical Review. B, 2009, 80(23): 235426
85. Peköz R, Erkoç Ş. A theoretical study of chemical doping and width effect on zigzag graphene nanoribbons. Physica E, Low-Dimensional Systems and Nanostructures, 2009, 42(2): 110 115
86. Shao Y, Zhang S, Engelhard M H, Li G, Shao G, Wang Y, Liu J, Aksay I A, Lin Y. Nitrogen-doped graphene and its electrochemical applications. Journal of Materials Chemistry, 2010, 20 (35): 7491 7496
87. Ma X, Wang Q, Chen L Q, Cermignani W, Schobert H H, Pantano C G. Semi-empirical studies on electronic structures of a boron-doped graphene layer implications on the oxidation mechanism. Carbon, 1997, 35(10-11): 1517 1525
88. Dutta S, Pati S K. Half-metallicity in undoped and boron doped graphene nanoribbons in the presence of semilocal exchange-correlation interactions. Journal of Physical Chemistry B, 2008, 112(5): 1333 1335
89. Panchakarla L S, Govindaraj A, Rao C N R. Boron-and nitrogen-doped carbon nanotubes and graphene. Inorganica Chimica Acta, 2010, 363(15): 4163 4174
90. Ci L, Song L, Jin C, Jariwala D, Wu D, Li Y, Srivastava A, Wang Z F, Storr K, Balicas L, et al. Atomic layers of hybridized boron nitride and graphene domains. Nature Materials, 2010, 9(5): 430 435
91. Drost R, Uppstu A, Schulz F, Hämäläinen S K, Ervasti M, Harju A, Liljeroth P. Electronic states at the graphene-hexagonal boron nitride zigzag interface. Nano Letters, 2014, 14(9): 5128 5132
92. Nigar S, Zhou Z, Wang H, Imtiaz M. Modulating the electronic and magnetic properties of graphene. RSC Advances, 2017, 7(81): 51546 51580
93. Rani P, Jindal V K. Designing band gap of graphene by B and N dopant atoms. RSC Advances, 2013, 3(3): 802 812
94. Nath P, Chowdhury S, Sanyal D, Jana D. Ab-initio calculation of electronic and optical properties of nitrogen and boron doped graphene nanosheet. Carbon, 2014, 73: 275 282
95. Kawasaki T, Ichimura T, Kishimoto H, Akbar A A, Ogawa T, Oshima C. Double atomic layers of graphene/monolayer h-BN on Ni (111) studied by scanning tunneling microscopy and scanning tunneling spectroscopy. Surface Review and Letters, 2002, 9(3-4): 1459 1464
96. Giovannetti G, Khomyakov P A, Brocks G, Kelly P J, Van Den Brink J. Substrate-induced band gap in graphene on hexagonal boron nitride: Ab initio density functional calculations. Physical Review. B, 2007, 76(7): 073103
97. Shemella P, Nayak S K. Electronic structure and band-gap modulation of graphene via substrate surface chemistry. Applied Physics Letters, 2009, 94(3): 032101
98. Zhou S Y, Gweon G H, Fedorov A V, First P D, De Heer W A, Lee D H, Guinea F, Castro Neto A H, Lanzara A. Substrate-induced bandgap opening in epitaxial graphene. Nature Materials, 2007, 6 (10): 770 775
99. Liu A Y, Wentzcovitch R M, Cohen M L. Atomic arrangement and electronic structure of BC2N. Physical Review. B, 1989, 39(3): 1760
100. Miyamoto Y, Rubio A, Cohen M L, Louie S G. Chiral tubules of hexagonal BC2N. Physical Review. B, 1994, 50(7): 4976
101. Liang Y, Kawazoe Y. Half-metallicity modulation of hybrid BN-C nanotubes by external electric fields: A first-principles study. Journal of Chemical Physics, 2014, 140(23): 234702
102. Huang Y, Bando Y, Tang C, Zhi C, Terao T, Dierre B, Sekiguchi T, Golberg D. Thin-walled boron nitride microtubes exhibiting intense band-edge UV emission at room temperature. Nanotechnology, 2009, 20(8): 085705
103. Silva F W N, Cruz-Silva E, Terrones M, Terrones H, Barros E B. BNC nanoshells: A novel structure for atomic storage. Nanotechnology, 2017, 28(46): 465201
104. Ding Y, Wang Y, Ni J. Electronic properties of graphene nanoribbons embedded in boron nitride sheets. Applied Physics Letters, 2009, 95(12): 123105
105. Kim W Y, Choi Y C, Kim K S. Understanding structures and electronic/spintronic properties of single molecules, nanowires, nanotubes, and nanoribbons towards the design of nanodevices. Journal of Materials Chemistry, 2008, 18(38): 4510 4521
106. D'Innocenzo V, Srimath Kandada A R, De Bastiani M, Gandini M, Petrozza A. Tuning the light emission properties by band gap engineering in hybrid lead halide perovskite. Journal of the American Chemical Society, 2014, 136(51): 17730 17733
107. Seifert M, Vargas J E, Bobinger M, Sachsenhauser M, Cummings A W, Roche S, Garrido J A. Role of grain boundaries in tailoring electronic properties of polycrystalline graphene by chemical functionalization. 2D Materials, 2015, 2(2): 024008
108. Chow P K, Jacobs-Gedrim R B, Gao J, Lu T M, Yu B, Terrones H, Koratkar N. Defect-induced photoluminescence in monolayer semiconducting transition metal dichalcogenides. ACS Nano, 2015, 9(2): 1520 1527
109. Moon J, An J, Sim U, Cho S P, Kang J H, Chung C, Seo J H, Lee J, Nam K T, Hong B H. One-step synthesis of *N*-doped graphene quantum sheets from monolayer graphene by nitrogen plasma. Advanced Materials, 2014, 26(21): 3501 3505
110. Kato T, Jiao L, Wang X, Wang H, Li X, Zhang L, Hatakeyama R, Dai H. Room-temperature edge functionalization and doping of graphene by mild plasma. Small, 2011, 7(5): 574 577
111. Foley B M, Hernández S C, Duda J C, Robinson J T, Walton S G, Hopkins P E. Modifying surface energy of graphene via plasma-based chemical functionalization to tune thermal and electrical

transport at metal interfaces. Nano Letters, 2015, 15(8): 4876 4882
112. Singh R S. Influence of oxygen impurity on electronic properties of carbon and boron nitride nanotubes: A comparative study. AIP Advances, 2015, 5(11): 117150
113. Nan H, Wang Z, Wang W, Liang Z, Lu Y, Chen Q, He D, Tan P, Miao F, Wang X, et al. Strong photoluminescence enhancement of MoS_2 through defect engineering and oxygen bonding. ACS Nano, 2014, 8(6): 5738 5745
114. Shin Y J, Wang Y, Huang H, Kalon G, Wee A T S, Shen Z, Bhatia C S, Yang H. Surface-energy engineering of graphene. Langmuir, 2010, 26(6): 3798 3802
115. Elias D C, Nair R R, Mohiuddin T M G, Morozov S V, Blake P, Halsall M P, Ferrari A C, Boukhvalov D W, Katsnelson M I, Geim A K, et al. Control of graphene's properties by reversible hydrogenation: Evidence for graphane. Science, 2009, 323 (5914): 610 613
116. Tang Y B, Yin L C, Yang Y, Bo X H, Cao Y L, Wang H E, Zhang W J, Bello I, Lee S T, Cheng H M, et al. Tunable band gaps and *p*-type transport properties of boron-doped graphenes by controllable ion doping using reactive microwave plasma. ACS Nano, 2012, 6(3): 1970 1978
117. Jhon Y I, Kim Y, Park J, Kim J H, Lee T, Seo M, Jhon Y M. Significant exciton brightening in monolayer tungsten disulfides via fluorination: *n*-Type gas sensing semiconductors. Advanced Functional Materials, 2016, 26(42): 7551 7559
118. Zhang X, Hsu A, Wang H, Song Y, Kong J, Dresselhaus M S, Palacios T. Impact of chlorine functionalization on high-mobility chemical vapor deposition grown graphene. ACS Nano, 2013, 7 (8): 7262 7270
119. Kim Y, Jhon Y I, Park J, Kim C, Lee S, Jhon Y M. Plasma functionalization for cyclic transition between neutral and charged excitons in monolayer MoS_2. Scientific Reports, 2016, 6:21405
120. Sajjad M, Morell G, Feng P. Advance in novel boron nitride nanosheets to nanoelectronic device applications. ACS Applied Materials & Interfaces, 2013, 5(11): 5051 5056
121. Nipane A, Karmakar D, Kaushik N, Karande S, Lodha S. Few-layer MoS_2 *p*-type devices enabled by selective doping using low energy phosphorus implantation. ACS Nano, 2016, 10(2): 2128 2137
122. Azcatl A, Qin X, Prakash A, Zhang C, Cheng L, Wang Q, Lu N, Kim M J, Kim J, Cho K, et al. Covalent nitrogen doping and compressive strain in MoS_2 by remote N_2 plasma exposure. Nano Letters, 2016, 16(9): 5437 5443
123. Stampfer C, Schurtenberger E, Molitor F, Guttinger J, Ihn T, Ensslin K. Tunable graphene single electron transistor. Nano Letters, 2008, 8(8): 2378 2383
124. Wang H, Maiyalagan T, Wang X. Review on recent progress in nitrogen-doped graphene: Synthesis, characterization, and its potential applications. ACS Catalysis, 2012, 2(5): 781 794
125. Jeong H M, Lee J W, Shin W H, Choi Y J, Shin H J, Kang J K, Choi J W. Nitrogen-doped graphene for high-performance ultracapacitors and the importance of nitrogen-doped sites at basal planes. Nano Letters, 2011, 11(6): 2472 2477
126. Zhang W, Lin C T, Liu K K, Tite T, Su C Y, Chang C H, Li L J. Opening an electrical band gap of bilayer graphene with molecular doping. ACS Nano, 2011, 5(9): 7517 7524
127. Nourbakhsh A, Cantoro M, Vosch T, Pourtois G, Clemente F, van der Veen M H, Hofkens J, Heyns M M, De Gendt S, Sels B F. Bandgap opening in oxygen plasma-treated graphene. Nanotechnology, 2010, 21(43): 435203
128. Ionescu R, Espinosa E H, Sotter E, Llobet E, Vilanova X, Correig X, Felten A, Bittencourt C, Van Lier G, Charlier J, et al. Oxygen functionalisation of MWNT and their use as gas sensitive thick-film layers. Sensors and Actuators. B, Chemical, 2006, 113(1): 36 46
129. Chiang W H, Lin T C, Li Y S, Yang Y J, Pei Z. Toward bandgap tunable graphene oxide nanoribbons by plasma-assisted reduction and defect restoration at low temperature. RSC Advances, 2016, 6 (3): 2270 2278
130. Han Z J, Murdock A T, Seo D H, Bendavid A. Recent progress in plasma-assisted synthesis and modification of 2D materials. 2D Materials, 2018, 5(3): 032002
131. Wojtaszek M, Tombros N, Caretta A, Van Loosdrecht P H M, Van Wees B J. A road to hydrogenating graphene by a reactive ion etching plasma. Journal of Applied Physics, 2011, 110(6): 063715
132. Radisavljevic B, Radenovic A, Brivio J, Giacometti I V, Kis A. Single-layer MoS_2 transistors. Nature Nanotechnology, 2011, 6(3): 147 150
133. Zhou W, Zou X, Najmaei S, Liu Z, Shi Y, Kong J, Lou J, Ajayan P M, Yakobson B I, Idrobo J C. Intrinsic structural defects in monolayer molybdenum disulfide. Nano Letters, 2013, 13(6): 2615 2622
134. Su J, Li N, Zhang Y, Feng L, Liu Z. Role of vacancies in tuning the electronic properties of Au-MoS_2 contact. AIP Advances, 2015, 5 (7): 077182
135. Liu D, Guo Y, Fang L, Robertson J. Sulfur vacancies in monolayer MoS_2 and its electrical contacts. Applied Physics Letters, 2013, 103(18): 183113
136. Qiu H, Xu T, Wang Z, Ren W, Nan H, Ni Z, Chen Q, Yuan S, Miao F, Song F, et al. Hopping transport through defect-induced localized states in molybdenum disulphide. Nature Communications, 2013, 4: 2642
137. Hong J, Hu Z, Probert M, Li K, Lv D, Yang X, Gu L, Mao N, Feng Q, Xie L, et al. Exploring atomic defects in molybdenum disulphide monolayers. Nature Communications, 2015, 6: 6293
138. Islam M R, Kang N, Bhanu U, Paudel H P, Erementchouk M, Tetard L, Leuenberger M N, Khondaker S I. Tuning the electrical property via defect engineering of single layer MoS_2 by oxygen plasma. Nanoscale, 2014, 6(17): 10033 10039
139. Zhang L, Zhou Y, Guo L, Zhao W, Barnes A, Zhang H T, Craig E, Zheng Y, Brahlek M, Haneef H F, et al. Correlated metals as transparent conductors. Nature Materials, 2016, 15(2): 204 210
140. Castellanos-Gomez A, Wojtaszek M, Tombros N, van Wees B J. Reversible hydrogenation and bandgap opening of graphene and graphite surfaces probed by scanning tunneling spectroscopy. Small, 2012, 8(10): 1607 1613
141. Zheng X H, Wang X L, Abtew T A, Zeng Z. Building half-metallicity in graphene nanoribbons by direct control over edge states occupation. Journal of Physical Chemistry C, 2010, 114(9): 4190 4193
142. Endo M, Hayashi T, Hong S H, Enoki T, Dresselhaus M S. Scanning tunneling microscope study of boron-doped highly

oriented pyrolytic graphite. Journal of Applied Physics, 2001, 90 (11): 5670 5674

143. Neto A C, Guinea F, Peres N M, Novoselov K S, Geim A K. The electronic properties of graphene. Reviews of Modern Physics, 2009, 81(1): 109 162
144. Kane C L, Mele E J. Quantum spin Hall effect in graphene. Physical Review Letters, 2005, 95(22): 226801
145. Young A F, Sanchez-Yamagishi J D, Hunt B, Choi S H, Watanabe K, Taniguchi T, Ashoori R C, Jarillo-Herrero P. Tunable symmetry breaking and helical edge transport in a graphene quantum spin Hall state. Nature, 2014, 505(7484): 528 532
146. Saffarzadeh A, Farghadan R. A spin-filter device based on armchair graphene nanoribbons. Applied Physics Letters, 2011, 98(2): 023106

Chapter 6

Conclusions and Future Outlooks

The experimental results presented in this dissertation establish that the atmospheric pressure plasma jet is a supreme tool for the fabrication of nanomaterials and simultaneous synthesis and deposition. Atmospheric pressure plasma-vapor chemistry is simple, and the free electrons generated in the plasma take over the reactions, easily skipping complex chemical reactions. Exclusively for the fabrication of metal nanoparticles such as gold from respective metal salts, atmospheric pressure plasma jets could be an excellent choice. The non-toxic nature and efficiency in a short time, likely in 1-10 minutes, is very promising for future techniques for the green synthesis of nanoparticles. This PhD dissertation discusses the possible reaction mechanisms inside the plasma and the potential applications of plasma-generated nanoparticles in biomedical applications. The following objectives have been achieved by this dissertation.

Objective 1: Designing and assembling a plasma deposition system employing atmospheric pressure plasma jet as a tool.

The design of the atmospheric pressure plasma system comprised of a single electrode atmospheric pressure plasma jet, a high voltage power supply, a nebulizer for the stock solution (metal/metal oxide precursor), a desirable substrate for the deposition, gas flow controllers, and a moving substrate holder. The plasma system has been successfully assembled in the initial stage of the work. The initial idea was to use metal/metal oxide precursor vapors in plasma, followed by the reduction and deposition of the metals. In order to achieve a strong downward flow that can carry nanoparticles to the substrate, a single copper wire electrode atmospheric pressure plasma jet has been selected for the work rather than a DBD plasma jet. The next step is to form a reaction column that can integrate plasma with the feed. For that, we designed a 3 cm long reaction tube made of quartz, having a diameter of 8 mm. to introduce the feed to the plasma, an inlet of the length of 2 cm to the tube was created with the same diameter, at an angle of 60°. To establish the flow of precursor material to the tube, a nebulizer (atomizer/vaporizer) is used. Considering the physical and chemical properties of the precursor materials in use, some are corrosive to the metallic material. Thus, a nebulizer made of plastic is used for that. Plasma was successfully generated with He plasma, and the nebulization of the solution /suspension was done by Ar gas. The reduction and synthesis of nanoparticles were magnificently carried out using the new atmospheric pressure plasma jet. In order to

perform a uniform deposition on the silicon wafer substrate, a moving substrate holder was employed. A motor working with a software program (Windows for PC) is connected to the substrate holder to ensure the uniformity of the deposition.

Objective 1 is addressed in chapters 2 and 3.

Objective 2: Formulation of favorable atmospheric pressure plasma conditions such as gas flow, power, etc., which would influence the reduction/synthesis rate of metal or metal oxide nanoparticles.

Atmospheric pressure plasmas are easy to tune at the same time. It is hard to maintain the same conditions since several atmospheric conditions, such as humidity, can affect efficiency. However, it can be nearly stabilized by changing or fixing the physical plasma parameters like working gas flow, feed gas flow, or plasma power. From a series of trial-and-error methods on the parameters, we came to the point that the reduction of the precursor can only be affected by the applied plasma power. As the applied power increases, the efficiency of the reduction of the metal precursor also increases.

On the other hand, the deposition rate can also be controlled by the feed gas flow and the applied power. To authenticate the experimental conditions, we used a fixed flow rate for the working gas and feed gas flow to vary according to the requirement of nanoparticles on the sample. The maximum power tolerable for a fine deposition without destroying the substrate is measured and identified as 25 W for this particular deposition system.

Objective 2 is addressed in chapter 2.

Objective 3: Interpretation of possible plasma mechanisms for the formation of nanoparticles.

The interactions of atmospheric pressure plasma with vapors have been unclear for ages since complete quantitative studies are limited and cannot be explained completely. However, a possible mechanism for the reduction of metal salts inside the plasma involves high-energy electrons inside the plasma. The high-energy free electrons generated inside plasma are the initiators of all the reactions leading to the reduction and formation of nanoparticles in the plasma-vapor interface. OES spectroscopy has been recorded during the experiments to understand how the species formed during the interaction of plasma with the precursor. The abundant hydroxide species (OH) found in the spectra explains a dominant mechanism for the reduction of metal salts. The reaction initiated by the electrons leads to the formation of OH radicals, which combine with hydrogen peroxide (H_2O_2), which promotes reduction reactions. Several mechanisms have been reported from liquid plasma interactions involving hydrogen-hydroxyl radicles and nanoparticle formations. However, the reduction mechanism for plasma-vapor interactions can only be attributed to the in-house electrons inside the plasma capable of creating reducing agents like hydroxyl groups from water. Thus, these electrons in the plasma can be called initiators

of the reaction. To elaborate on the case, the studies with ethanol as a solvent for the precursor instead of water turn out the reduction inside the plasma remains the same. Still, the particles are much smaller than those formed from the water solution.

Objective 3 is addressed in chapter 2.

Objective 4: Analysis and scope of synthesized nanoparticles according to their size, shape, and physicochemical characteristics, for instance, plasmonic behavior of polyhedral nanocrystals of gold.

Nanoparticles of gold from its metal salt (Chloroauric acid, $HAuCl_4$) are successfully fabricated using atmospheric pressure plasma-vapor chemistry and effectively deposited onto a silicon wafer substrate. The nanoparticles formed in the deposited nanoparticles are analyzed using SEM, TEM, XPS, and SERS. The XPS showed a complete reduction of Au^{3+} to Au^0 from some particular samples (proportions of water and ethanol solvents). However, the chlorine content after reduction and deposition is remarkably low. The gold nanoparticles are found well developed and distorted spherical shapes from the SEM micrographs. The approximate size of the particles is around 100-150 nm. From the detailed study using TEM on the nanoparticles deposited from the ethanol solution of the precursor, some detailed morphologies of the particles were discovered. Some of the particles were irregularly shaped AuNPs. Still, the well-developed particles show forms of the irregular octahedron, triangular and hexagonal plates with single or multiple twinning boundaries, and decahedrons with 5-fold symmetry. The geometries of the nanoparticles synthesized by the atmospheric pressure plasma jet lead to an obvious possibility of plasmonic activity caused by the scattering and reflections from the nanoparticles. The particles on the substrate were experimented with as analytics for SERS and came out positive.

Objective 4 is addressed in chapters 2 and 4.

Objective 5: Investigation of the applications of plasma-generated nanoparticles in bio-sensing applications utilizing the molecular attributes of the nanoparticles; nanoelectronics devices, plasmonic sensors, etc.

Plasma-generated nanoparticles are in prime focus when it comes to purity and bio-compatibility as well as in terms of material processing. The highest probability is in biomedical applications and nanoelectronics devices. However, the investigation of the applications of the plasma-synthesized nanoparticles leads to the utilization of the nanoparticles (gold nanoparticles) as a tool in Surface-Enhanced Raman Spectroscopy. We could find that the application of plasma-processed nanomaterials is useful in descriptive DNA studies. The gold nanoparticles fabricated by atmospheric pressure plasma jet possess highly efficient plasmonic arrangements, which can be used as a tool in sensing applications in the biomedical field. Here, we present a DNA study using Surface-Enhanced Raman Spectroscopy using plasma-engineered nanoparticles as a tool. Apart from this, plasma jet imports nanoparticles to desirable substrates as it can also fabricate nanoparticles. This

can be exploited in surface modification/decoration of limelight materials like graphene and other two-dimensional materials.

Objective 5 is addressed in chapters 4 and 5.

6.1 Conclusion and Future Propositions

Atmospheric pressure plasma jets are promising tools for the fabrication of gold nanoparticles without any reducing or stabilizing agents. This could be a major breakthrough in the synthesis of noble metal nanoparticles from their common salts. Plasma-vapor interactions are unexplored or unexplained pathways in which wet plasma-generated electrons play as initiators of the chemical reactions that lead to the reduction of metal salts and thereby to the nucleation and the growth of metal nanoparticles. This dissertation could enlighten the research on plasma-vapor interactions and chemical reactions. Optical emission spectroscopy is a significant tool for monitoring the excited species during the process, and it supports the mechanism that we put forward. From further analysis of the nanoparticles deposited on the substrate, the particles possess different distorted geometries that can be used in a number of applications, which has been proven as a tool for SERS in DNA analysis.

Moreover, the simultaneous plasma synthesis and deposition of nanoparticles can be employed for nanoparticle printing on substrates. However, the solubility and dispersibility in the solvent are crucial for the dispersion of the precursor inside the plasma reaction column. The main advantage of this plasma-assisted method is its biocompatibility and simple procedure, which can replace multi-step, long chemical and biological procedures. Followed by the investigations on noble metal salts, we foresee the possibility of deposition of metal oxide nanoparticles using atmospheric pressure plasma jets. Based on the primary evidence, we presume simple nanoparticle depositions of metal oxides like V_2O_5 from their commercially available powders can be accomplished by the same atmospheric pressure plasma setup.

Future propositions: The plasma-vapor chemistry, which has been well-established for gold nanoparticle synthesis, can also be manipulated further to other noble metals, such as silver, palladium, platinum, etc. When it comes to the reduction of heavy noble metals with APPJs, the reduction efficiency is highly dependable on the plasma power source's applied voltage (power), the dispersibility of the metal ions in the solvent, and the carrier gas. With complete management of the solvent-solute concentrations, complete reduction with APPJs is achievable. More promising depositions could be possible on silver nanoparticles from Silver (I) fluoride (AgF), wherein Ag^+ ions are very easy to be reducible with mere electron exchange inside the plasma. Same as in the case of palladium salt and platinum salts ($Na_2[PdCl_4]$ and H_2PtCl_6), but the oxidation states of the metals are higher. As the oxidation number increases, the reduction requires high energies or active species inside the plasma. This is barely achievable for the current plasma setup, but there are

some ongoing investigations in this direction. Thus, this dissertation is putting forward an idea of successive investigations to achieve a complete reduction of noble metals other than gold from their metal salts by using atmospheric pressure plasma jets.

Appendix A

European Patent Application

A.1 Method for in-situ synthesis and deposition of metal oxide nanoparticles with atmospheric pressure plasma

EP 3960703A1

Date of filing: 26.08.2020
Date of publication: 02.03.2022

Investigators:

Aswathy Vasudevan, Gregor Filipič, Janez Zavašnik, Uroš Cvelbar

Jožef Stefan Institute, Ljubljana 1000, Slovenia

(19) Europäisches Patentamt
European Patent Office
Office européen des brevets

(11) EP 3 960 703 A1

(12) EUROPEAN PATENT APPLICATION

(43) Date of publication:
02.03.2022 Bulletin 2022/09

(21) Application number: **20192874.4**

(22) Date of filing: **26.08.2020**

(51) International Patent Classification (IPC):
C01B 13/14 *(2006.01)* ***B29C 64/00*** *(2017.01)*
B82Y 30/00 *(2011.01)* ***C01G 31/02*** *(2006.01)*
H05H 1/00 *(2006.01)*

(52) Cooperative Patent Classification (CPC):
C01B 13/145; B82Y 40/00; C01G 31/02; H05H 1/2406; H05H 1/2443; H05H 1/245; C01P 2004/52; C01P 2004/64

(84) Designated Contracting States:
AL AT BE BG CH CY CZ DE DK EE ES FI FR GB GR HR HU IE IS IT LI LT LU LV MC MK MT NL NO PL PT RO RS SE SI SK SM TR
Designated Extension States:
BA ME
Designated Validation States:
KH MA MD TN

(71) Applicant: **Institute Jozef Stefan**
1000 Ljubljana (SI)

(72) Inventors:
- **Vasudevan, Aswathy**
  1000 Ljubljana (SI)
- **Filipic, Gregor**
  1000 Ljubljana (SI)
- **Zavasnik, Janez**
  1000 Ljubljana (SI)
- **Cvelbar, Uros**
  1000 Ljubljana (SI)

(74) Representative: **Nederlandsch Octrooibureau**
P.O. Box 29720
2502 LS The Hague (NL)

(54) **METHOD FOR IN-SITU SYNTHESIS AND DEPOSITION OF METAL OXIDE NANOPARTICLES WITH ATMOSPHERIC PRESSURE PLASMA**

(57) The present invention concerns a method for the in-situ synthesis of metal oxide nanoparticles, such as vanadium pentoxide nanoparticles, from metal oxide macropowder using atmospheric pressure plasma, followed by the direct deposition of said metal oxide nanoparticles onto the surface of materials of interest.

EP 3 960 703 A1

Printed by Jouve, 75001 PARIS (FR)

Description

FIELD OF THE INVENTION

[0001] The current invention concerns a method for the synthesis of metal oxide nanoparticles, particularly vanadium pentoxide nanoparticles, from metal oxide macropowder using an atmospheric pressure plasma.

BACKGROUND OF THE INVENTION

[0002] The scientific potential of nanomaterials currently attracts much attention for a diverse range of applications, such as catalysis, energy production, coatings and computers. This is also true for nanoparticles consisting of metal oxides. The currently available methods of synthesising metal oxide nanoparticles typically include one or more of chemical synthesis, mechanical grinding, colloidal precipitation and gas-phase nucleation and growth (aerosol process). Among the existing techniques, gas-phase synthesis has benefits because of the purity of the resulting product, but the control of the distribution of particles and the rate of aggregation and agglomeration are challenging.

[0003] Considering transition metal oxides, particularly vanadium pentoxide nanoparticles attract attention due to their unique properties. High-purity particles of vanadium pentoxide are highly desired in certain field of industry, such as in energy materials, medicine and aerospace. According to the statistics of recent years, domestic demand of high-purity vanadium pentoxide is expected to increase in the European Union, United States and Japan over the coming years. Reduction of the particle size to the nano-range and maximising of the surface area of vanadium pentoxide (V_2O_5), will further expand the range of applications because of the change in electrical resistance on response to various stimuli such as the applied electrical field [1], thermal treatment [2] or ultraviolet light irradiation [3].

[0004] Several methods have been disclosed in the prior art for the synthesis of metal oxide nanoparticles on an industrial scale. The various methods disclosed try to control the particle size of the nanoparticles and thereby the particle size distribution in different ways. For example, in US2017/0298516A1 and US2017/0259501A1, an atmospheric plasma jet is used for printing nanoparticles. The nanoparticles are dispersed in a liquid and used as an ink. The dispersion is delivered to a substrate's surface through a plasma jet. The final product is a film. This is not a synthesis method for nanoparticles since the initial particles in the ink are already nano-sized. Accordingly, if the particles are in the micro-sized range, they remain the same during the process, and are not reduced in size. In addition, the particles get printed/melted on the surface of the substrate.

[0005] US8,282,906B2 discloses another plasma-associated method for nanoparticle synthesis, specifically titanium oxide nanoparticles. The method comprises generating plasma from oxygen in a chamber and contacting the oxygen plasma via a connection part with an organic precursor of titanium oxide in a remote chamber. The plasma oxidises the organic titanium oxide precursor, and the titanium oxide particles deposit. The resulting particles have a size distribution that mainly falls between 8 and 12 nm. Their crystal structure can, however, not be controlled (anatase or rutale phase, single- or polycrystal structure) and the impurities pose a problem.

[0006] US8,029,595B2 discloses the use of an RF plasma torch to synthesise nanoparticles from a solution or suspension comprising dissolved or suspended precursors of the intended particle material. Using a nebulising technique, an aerosol is created from the solution or suspension which is lead to the plasma torch where it converted to the intended material in the form of nanoparticles. The nanoparticles are subsequently deposited onto the surface of a substrate. This method does not enable the deposition of individual nanoparticles.

[0007] The method described in US7,169,375B2 produces nanoparticles from a sol method involving complicated chemistry with mixtures of metal alkoxides and organosilanes. The procedures are lengthy, involving many heating and drying steps lasting five or more hours. The final products are nanoparticles coated with an organic material to prevent agglomeration. The pure crystalline metal-oxide nanoparticles are not achievable without an additional cleaning step.

[0008] US2015/0162596A1 and US2015/162583A1 disclose plasma spraying (painting) of electrodes with lithium and silicon precursor nanoparticles. The precursors are admixed in a liquid carrier which serves for transport and cooling of the precursors in the plasma. The mixture of the precursors in the liquid carrier is injected into the plasma under pressure. The result is a thick layer of a silicon and lithium, mostly melted, nanoparticle coating on top of a conductive material. This method is not suitable to deposit separated, non-deformed nanoparticles.

[0009] US8,318,128 discloses a method for the preparation of VO_2 nanoparticles by a reaction of a vanadyl ester - $VO(OR)_3$, wherein R is an alkyl group - with a carboxylic acid in an aqueous medium, followed by precipitation of VO_2 nanoparticles.

[0010] US5,935,293, US5,749,937, US5,788,738, US5,851,507 and US5,935,293 all disclose methods for rapid expansion or quenching of a gaseous phase during synthesis.

[0011] US5,935,293 and US5,749,937 disclose methods that uses metal halides as a precursor for creating metal powder. These methods use a plasma torch as a means for high-temperature thermal conversion.

[0012] US5,851,507 and US5,788,738 disclose a method for producing nanoscale powder from a precursor material by evaporating the precursor material in a gaseous atmosphere by means of a thermal reactor with the help of a radiofrequency plasma.

[0013] US5,935,293 discloses a method for thermally

converting gaseous precursors in a plasma arc between the electrodes of a plasma torch resulting in ultrafine solid particles.

[0014] It is an objective of the present invention to provide an improved and/or simplified method for the production of metal oxide nanoparticles, particularly vanadium pentoxide nanoparticles.

[0015] It is a further objective of the present invention to provide an improved and/or simplified method for the production of metal oxide nanoparticles, particularly vanadium pentoxide nanoparticles, wherein the formed metal oxide nanoparticles can be directly deposited onto temperature-sensitive substrates.

[0016] It is a further objective of the present invention to provide a method for the production of metal oxide nanoparticles, particularly vanadium pentoxide nanoparticles, with improved control of the purity and/or the crystallinity and/or the particle size distribution of the metal oxide nanoparticles.

SUMMARY OF THE INVENTION

[0017] The inventors have unexpectedly found that the above objectives can be met by a method wherein a metal oxide macropowder dispersed in a liquid is converted to an aerosol and wherein the aerosol is subsequently contacted with an atmospheric pressure plasma. The resulting metal oxide nanoparticles can be directly deposited onto temperature-sensitive substrates, like plastics.

[0018] The method can be applied with any atmospheric pressure plasma (jet) with an inlet feed of gas and a metal oxide macropowder dispersed in a liquid. Nanoparticles of any metal oxide which is dispersible in water or any other simple liquid, can be synthesised using this method.

[0019] The metal oxide nanoparticles are of the same chemical composition and crystal structure as the selected macrosized metal oxide powder. Accordingly, with a proper selection of the purity and/or the crystal structure of the metal oxide macropowder, the purity and/or the crystal structure of the metal oxide nanoparticles can be controlled.

[0020] The plasma from inert gases converts the metal oxide macropowder to nanoparticles. Because no chemical reactions are involved in the size reduction of the particles, no further purification is needed, and the synthesised nanoparticles can therefore be deposited directly on a substrate of interest.

[0021] The method results in unimodal particle size distributions. The plasma prevents or reduces nanoparticle agglomeration before adhering to the substrate.

[0022] The method is beneficial for precise applications, such as in electronics and sensors.

[0023] Accordingly, in an aspect, the invention concerns a method for the in-situ synthesis of metal oxide nanoparticles with atmospheric pressure plasma, the method including the steps of:

a) preparing a dispersion (15) from a metal oxide macropowder in a liquid;
b) nebulising the dispersion (15) obtained in step (a) in a nebuliser (3) by injection of an inert carrier gas (1) to form an aerosol (4);
c) providing a tubular system (22) having a dielectric tubular mixing section (10) and a tubular plasma generating section (24),
wherein said tubular system (22) has a side wall (16, 16a, 16b), a bottom (11) in the dielectric tubular mixing section (10) and a top (17) in the tubular plasma generating section (24), wherein the central axis of tubular system (22) is positioned substantially vertical,
wherein the dielectric tubular mixing section (10) comprises a dielectric inlet tube (14) having a first end connected to an opening (18) in the side wall (16b) of the dielectric tubular mixing section (10) and a second end (19) connected to the nebuliser (3),
wherein the plasma generating section (24) comprises a dielectric tube (23) extending into the dielectric tubular mixing section (10) up to the opening (18) in the side wall (16b) of the dielectric tubular mixing section (10), and
wherein the tubular plasma generating section (24) has an opening (20) in its side wall (16a) connected to dielectric tube (23), wherein the opening (20) is positioned above, in the direction of the central axis of tubular system (22), opening (18) in the side wall (16b) of the dielectric tubular mixing section (10);
d) supplying an inert working gas (7) to dielectric tube (23) of the tubular plasma generating section (24) via opening (20) in the side wall (16a) and creating an atmospheric pressure plasma from this inert working gas (7) at the outer end of dielectric tube (23) extending into the dielectric tubular mixing section (10);
e) supplying the aerosol (4) obtained in step (b) to the dielectric tubular mixing section (10) via dielectric inlet tube (14) and opening (18) in the side wall (16b);
f) allowing interaction of the aerosol (4) and the plasma in the dielectric tubular mixing section (10) to generate metal oxide nanoparticles characterized by a particle size distribution with a Dv99 of less than 100 nm, preferably with a Dv90 below 10 nm; and
g) deposition of said metal oxide nanoparticles through an orifice (21) in the bottom (11) of the dielectric tubular mixing section (10) onto a solid or semi-solid substrate (13).

BRIEF DESCRIPTION OF FIGURES

[0024] Figure 1 depicts a simplified schematic flow diagram of the method of the present invention. Figure 2 is a close up of the schematic flow diagram of Figure 1. Figure 3 is a microscopic picture of the vanadium oxide metal oxide nanoparticles, produced by the method of the invention. Figure 4 is a representation of the distri-

bution of vanadium oxide nanoparticles produced by the method of the invention on a silicon wafer substrate.

DEFINITIONS

[0025] The term *'sccm'* as used in the context of the present invention is an abbreviation of *'standard cubic centimetre per minute'* and concerns a volumetric unit of flow measurement defined at the following standard conditions: a temperature of 273.15 K and a pressure of 100000 Pa.

[0026] The wording *'substantially vertical'* in the context of the invention means substantially vertical with respect to the floor or bottom as the horizontal plane. In other words, it means substantially perpendicular to the floor or bottom. The wording *'substantially vertical'* concerns the (central axis of) the tubular system (22) as well as its individual sections (10) and (24).

[0027] The term *'substantially'* in *'substantially vertical'* is to be construed as vertical or close to vertical. Within the context of the invention, *'substantially vertical'* includes angles of between 80 and 90° with the floor or bottom as the horizontal plane.

[0028] The feature Dv50 as used herein and as used in the art concerns a median particle diameter, as measured with laser diffraction, based on a volume distribution. This median particle diameter is the diameter where half of the population of the particles lies below. The diameter Dv90 is the diameter where 90% of the population of the particles lies below, as measured with laser diffraction, based on a volume distribution. Likewise, the diameter Dv99 is the diameter where 99% of the population of the particles lies below, as measured with laser diffraction, based on a volume distribution.

[0029] The term *'nanoparticles'* as used herein concerns particles having a particle size of about 1 to about 100 nm.

[0030] The term *'macropowder'* as used herein refers to particles having a median particle diameter Dv50 of between 0.1 and 1 mm.

[0031] The term *'plasma'* as used herein means at least partially ionized gas.

[0032] The term *'semi-solid substrate'* in the context of the present invention relates to substrates having sufficient mechanical integrity to not interfere with a gas stream, such as for example a gel.

DETAILED DESCRIPTION OF THE INVENTION

[0033] In an aspect, the invention concerns a method for the in-situ synthesis of metal oxide nanoparticles with atmospheric pressure plasma, the method including the steps of:

a) preparing a dispersion (15) from a metal oxide macropowder in a liquid;
b) nebulising the dispersion (15) obtained in step (a) in a nebuliser (3) by injection of an inert carrier gas (1) to form an aerosol (4);
c) providing a tubular system (22) having a dielectric tubular mixing section (10) and a tubular plasma generating section (24),
wherein said tubular system (22) has a side wall (16, 16a, 16b), a bottom (11) in the dielectric tubular mixing section (10) and a top (17) in the tubular plasma generating section (24), wherein the central axis of tubular system (22) is positioned substantially vertical,
wherein the dielectric tubular mixing section (10) comprises an dielectric inlet tube (14) having a first end connected to an opening (18) in the side wall (16b) of the dielectric tubular mixing section (10) and a second end (19) connected to the nebuliser (3),
wherein the plasma generating section (24) comprises a dielectric tube (23) extending into the dielectric tubular mixing section (10) up to the opening (18) in the side wall (16b) of the dielectric tubular mixing section (10), and
wherein the tubular plasma generating section (24) has an opening (20) in its side wall (16a) connected to dielectric tube (23), wherein the opening (20) is positioned above, in the direction of the central axis of tubular system (22), opening (18) in the side wall (16b) of the dielectric tubular mixing section (10);
d) supplying an inert working gas (7) to dielectric tube (23) of the tubular plasma generating section (24) via opening (20) in the side wall (16a) and creating an atmospheric pressure plasma from this inert working gas (7) at the outer end of dielectric tube (23) extending into the dielectric tubular mixing section (10);
e) supplying the aerosol (4) obtained in step (b) to the dielectric tubular mixing section (10) via dielectric inlet tube (14) and opening (18) in the side wall (16b);
f) allowing interaction of the aerosol (4) and the plasma in the dielectric tubular mixing section (10) to generate metal oxide nanoparticles characterized by a particle size distribution with a Dv99 of less than 100 nm, preferably with a Dv90 below 10 nm; and
g) deposition of said metal oxide nanoparticles through an orifice (21) in the bottom (11) of the dielectric tubular mixing section (10) onto a solid or semi-solid substrate (13).

[0034] The numbers between brackets (..) correspond to the numbers in Figures 1 and 2, wherein (22) represents a tubular system, (24) a tubular plasma generating section, such as a plasma jet generator, (1) an inert carrier gas, (2) a mass flow controller, (3) a nebuliser, (4) an aerosol, (5) an AC power generator, (6) a copper wire electrode, (7) an inert working gas, (8) a mass flow controller, (9) a dielectric cover, such as a teflon cover, (10) a dielectric tubular mixing section, (11) a bottom of tubular system (22), (12) a substrate holder, such as a movable substrate holder, (13) a substrate, such as a silicon wafer, (14) a dielectric inlet tube to dielectric tubular mixing sec-

tion (10), (15) a dispersion, (16) a side or outer wall of tubular system (22), (16a) a side or outer wall of tubular plasma generating section (24), (16b) a side or outer wall of dielectric tubular mixing section (10), (17) a top of tubular system (22), (18) an opening in side wall (16b) of the dielectric tubular mixing section (10), (19) a second end of dielectric inlet tube (14), (20) an opening in side wall (16a) of tubular plasma generating section (24), (21) an orifice in the bottom (11) of dielectric tubular mixing section (10), and (23) a dielectric tube, such as a glass tube.

[0035] In a preferred embodiment, the tubular plasma generating section (24) comprises a dielectric tubular cover (9) surrounding dielectric tube (23). As will be appreciated by the skilled person, if dielectric tubular cover (9) is present, the side wall (16a) of the tubular plasma generating section (24) is the outer wall of the dielectric tubular cover (9) and the opening (20) is provided in the dielectric tubular cover (9) and in the dielectric tube (23). If dielectric tubular cover (9) is not present, the side wall (16a) of the tubular plasma generating section (24) is the outer wall of dielectric tube (23) and the opening (20) is provided in dielectric tube (23). Preferably, the dielectric tubular cover (9) is thick enough to prevent electric sparks from the electrode to reach the surface of cover (9). Such a cover is for example advantageous if the tubular system is designed as a hand-held system or if the system is to be connected to parts that are not dielectric. Dielectric tubular cover (9) is preferably a teflon cover. Dielectric tube (23) is preferably made of a dielectric material, more preferably of glass.

[0036] In a preferred embodiment, the nebuliser (3) is connected to the inert carrier gas source (1) via a mass flow controller (2) to regulate the gas flow. The flow of the inert carrier gas (1) should be sufficiently high to nebulise the dispersion (15). In a preferred embodiment, the flow of the inert carrier gas (1) applied in step (b) is more than 1000 sccm, more preferably between 1000-3000 sccm, even more preferably between 2000 and 2500 sccm, most preferably about 2300 sccm.

[0037] The inert carrier gas (1) preferably is a heavy inert gas, such that it can nebulise the dispersion (15) effectively and can carry the aerosol (4) effectively into the plasma.

[0038] In a preferred embodiment, the inert carrier gas (1) applied in step (b) is a noble gas, more preferably argon.

[0039] The aerosol (4) formed is introduced into the plasma in dielectric tubular mixing section (10) via dielectric inlet tube (14) and opening (18). Dielectric tubular mixing section (10) and dielectric inlet tube (14) are preferably made from glass.

[0040] In a preferred embodiment, dielectric inlet tube (14) is positioned at an angle of inclination θ with the central axis of tubular system (22), such that the second end (19) connected to the nebuliser (3) is positioned above the first end connected to the opening (18) in the direction of the central axis of tubular system (22), wherein the angle of inclination θ preferably is between 50 and 89°, more preferably between 60 and 70°. The angle of inclination θ of dielectric inlet tube (14) ensures effective flow of the aerosol (4) to the plasma.

[0041] Plasma is generated from an inert working gas. Preferably, the inert working gas is a noble gas, most preferably helium. In a preferred embodiment, the flow of the inert working gas is controlled by a mass flow controller (8).

[0042] In a preferred embodiment, the inert working gas (7) in step (f) represents from 6 vol.% to 10 vol.%, based on the carrier gas (6-10 volume units of inert working gas per 100 volume units of carrier gas) .

[0043] The inert working gas (7) is converted to a plasma, such as a plasma jet, in the tubular plasma generating section (24) of tubular system (22). The plasma jet can be generated by any suitable device, such as a dielectric barrier discharge (DBD). Preferably, the plasma jet generating device is a single electrode atmospheric pressure plasma device. The single electrode (6) preferably is a metallic wire electrode, more preferably a metallic wire copper electrode (6).

[0044] Atmospheric plasma can for example be generated from the inert working gas (7) in the tubular plasma generating section (24) of tubular system (22) using an AC power generator (5), having a frequency in the range of 20-60 kHz, connected to an (copper wire) electrode (6) inside the tubular plasma generating section (24), more particularly inside dielectric tube (23). Plasma is generated at the tip of the wire electrode (6). The inert working gas (7) is ionised, and plasma is generated in the dielectric tubular mixing section (10).

[0045] The geometry of dielectric tubular mixing section (10) is designed in a manner to ensure maximum interaction of the aerosols (4) with the plasma coming from the tubular plasma generating section (24). The part of dielectric tubular mixing section (10) where plasma and aerosol meet is rich in high-energy reactive species such as free electrons and radicals, which mediate the reduction of the size of the metal oxide particles.

[0046] In order to collect the metal oxide nanoparticles, a substrate of interest (13) is placed on a substrate holder (12) under orifice (21). In an embodiment, the substrate holder (12) is a movable substrate holder (12) to allow uniform deposition and distribution of the particles onto the substrate (13). The movable substrate holder (12) can be connected to a motor, which enables a programmable movement of the substrate holder (12).

[0047] Figure 2 represent a close up of part of the scheme of Figure 1. Figure depicts different zones (A) - (C) in and outside the tubular system (22). Moreover, Figure 2 shows the angle of inclination θ of dielectric inlet tube (14) with the central axis of tubular system (22).

[0048] In a preferred embodiment, the tubular system (22) itself comprises two adjacent zones (A) and (B) in a direction of the central axis of tubular system (22) from the top (17) to the bottom (11):

- zone (A) is part of the dielectric tubular mixing section (10), comprising the opening (18) for supplying the aerosol (4), wherein plasma is generated at the outer end of dielectric tube (23) extending into the dielectric tubular mixing section (10), and wherein the plasma interacts with the aerosol (4) resulting in high energy particles and ion bombardment; and
- zone (B) below zone (A) is an afterglow zone which is also part of the dielectric tubular mixing section (10) and which comprises the orifice (21) wherein both reactive and neutral particles are present and wherein particles may aggregate by recombination.

[0049] Although recombination of the particles takes place in zone (B), a major portion of the alteration of the particle size occurs in zone (A), wherein the rate of ion bombardment and the temperature are higher as compared to the afterglow zone (B).

[0050] Figure 2 also depicts a zone (C) outside tubular system (22) and in between the orifice (21) and the substrate (13). In deposition zone (C), the metal oxide nanoparticles and the remaining plasma come into contact with the atmosphere and also with the substrate (13). The substrate (13) can be any solid or semi-solid material, dielectric or conductive, such as glass, silicon or nickel. Preferably, the substrate (13) is a metal/metallic substrate. More preferably the substrate (13) is a silicon wafer.

[0051] In a preferred embodiment, the substrate (13) is placed at a distance between 1 and 15 mm, preferably between 4 and 10 mm, from the orifice (21) in the direction of the central axis of tubular system (22).

[0052] In a preferred embodiment, steps (b) -(g), preferably steps (a) - (g), are performed as a continuous process.

[0053] In a preferred embodiment, the metal oxides in the macropowder used in step (a) and in the nanoparticles obtained in step (g) are oxides of transition metals, more preferably selected from the groups consisting of oxides of vanadium (V), niobium (Nb), ruthenium (Ru), manganese (Mn), cobalt (Co) and nickel (Ni), even more preferably oxides of vanadium, very preferably vanadium pentoxide.

[0054] In a very preferred embodiment, the liquid used in the dispersion (15) of step (a) is water.

[0055] The number density of the synthesised nanoparticles per unit of surface area of the substrate (13) is determined by the amount of accumulative time of the deposition: either absolute time when deposition on the same spot, or by the speed of the substrate (13) movement through the depositing section underneath mixing tube orifice (21).

[0056] Thus, the invention has been described by reference to certain embodiments discussed above. It will be recognized that these embodiments are susceptible to various modifications and alternative forms well known to those of skill in the art.

[0057] Furthermore, for a proper understanding of this document and its claims, it is to be understood that the verb *'to comprise'* and its conjugations are used in its non-limiting sense to mean that items following the word are included, but items not specifically mentioned are not excluded. In addition, reference to an element by the indefinite article *'a'* or *'an'* does not exclude the possibility that more than one of the element is present, unless the context clearly requires that there be one and only one of the elements. The indefinite article *'a'* or *'an'* thus usually means *'at least one'*.

[0058] The following example serves to demonstrate the preferred embodiments of the present invention and should not be interpreted as limiting the scope of the invention.

EXAMPLE

[0059] The method of the invention was applied to synthesise vanadium pentoxide (V_2O_5) nanoparticles from a vanadium pentoxide macropowder. The synthesised vanadium pentoxide nanoparticles were directly deposited onto a silicon wafer substrate. The precursor for V_2O_5 nanoparticles was a commercially available macropowder of V_2O_5 having a particle size of 0.1 - 1 mm, obtained from Sigma-Aldrich, Inc. The experimental setup, more particularly the tubular system (22), used is schematically depicted in Figures 1 and 2.

[0060] In a first step, a dispersion (15) of the vanadium pentoxide macropowder (0.01 g) in distilled water (25 mL) was prepared. 4 mL of the dispersion was transferred to a nebuliser (3) and nebulised with argon as an inert carrier gas (1) using a flow rate of 2300 sccm to provide an aerosol (4).

[0061] Prior to the injection of the aerosol (4), a flow of helium as an inert working gas (7) was introduced into the tubular atmospheric pressure plasma jet generator (24), which was operated by an AC power generator (5) at a frequency of 25 kHz (a high voltage power supply with 20 kV peak-peak, 20-30 mA at 20-60 kHz). The AC power generator (5) was connected to a concentric copper wire electrode (6) inside a glass tube (23) surrounded by a teflon cover layer (9). The inert working gas (7) was helium. The inert working gas (7) was introduced via opening (20). Helium represented 8% by volume of the gas flow of argon. The flowrate of helium was 200 sccm, which was sufficient to produce plasma. The plasma was generated and contacted with the aerosol (4) containing V_2O_5 inside the dielectric tubular mixing section (10). The dielectric tubular mixing section (10) was a glass tube of 8 mm diameter and with a length of 5 cm. A side glass inlet (14) for the aerosol (4), of the same diameter, and with a length of 2 cm, was connected to the dielectric tubular mixing section (10) at an angle of 65° with the central axis of the tubular system (22). The reduction of the particle size of the V_2O_5 macropowder to nanoparticles happened inside the plasma in the dielectric tubular mixing section (10) and was followed by deposition of the V_2O_5 nanoparticles on a silicon wafer substrate (13)

of dimension 1 cm×1 cm, placed at 5 mm distance from the orifice (21) of the dielectric tubular mixing section (10). The silicon wafer substrate (13) was placed on a moving stage substrate holder (12). The stage was connected to a software-controlled motor, which had a displacement in xy-direction, in a zigzag pattern, ensuring the uniform deposition of the V_2O_5 nanoparticles. It took 1.5 minutes to complete the zigzag movement on 1 cm^2 of the substrate. The deposition process was done in several cycles of the same movement for 15 minutes.

[0062] A scanning electron microscope was used to image the resulting product on the silicon wafer substrate (Figure 3). The V_2O_5 nanoparticles were distributed all over the substrate (13), as seen in Figure 3. Statistical analysis was performed to determine the particle size distribution. The V_2O_5 nanoparticles had a particle diameter between 2-10 nm and the majority of the particles has a diameter of about 6 nm (Figure 4).

REFERENCES

[0063]

1.) Ng, S. H.; Patey, T. J.; Büchel, R.; Krumeich, F.; Wang, J. Z.; Liu, H. K.; Pratsinis, S. E.; Novak, P., Flame Spray-Pyrolyzed Vanadium Oxide Nanoparticles for Lithium Battery Cathodes., Phys. Chem. Chem. Phys., 2009, 11, 3748-3755.

2.) Cui, H. N.; Teixeira, V.; Meng, L. J.; Wang, R.; Gao, J. Y.; Fortunato, E., Thermochromic Properties of Vanadium Oxide Films Prepared by Dc Reactive Magnetron Sputtering., Thin Solid Films, 2008, 516, 1484-1488.

3.) Cheremisin, A.; Putrolaynen, V.; Velichko, A.; Pergament, A.; Kuldin, N.; Grishin, A., UV Laser Modification and Selective Ion-Beam Etching of Amorphous Vanadium Pentoxide Thin Films., Phys. Status Solidi Appl. Mater. Sci., 2009, 206, 1484-1487.

Claims

1. A method for the in-situ synthesis of metal oxide nanoparticles with atmospheric pressure plasma, the method including the steps of:

   a) preparing a dispersion (15) from a metal oxide macropowder in a liquid;
   b) nebulising the dispersion (15) obtained in step (a) in a nebuliser (3) by injection of an inert carrier gas (1) to form an aerosol (4);
   c) providing a tubular system (22) having a dielectric tubular mixing section (10) and a tubular plasma generating section (24),
   wherein said tubular system (22) has a side wall (16, 16a, 16b), a bottom (11) in the dielectric tubular mixing section (10) and a top (17) in the tubular plasma generating section (24), wherein the central axis of tubular system (22) is positioned substantially vertical,
   wherein the dielectric tubular mixing section (10) comprises a dielectric inlet tube (14) having a first end connected to an opening (18) in the side wall (16b) of the dielectric tubular mixing section (10) and a second end (19) connected to the nebuliser (3),
   wherein the plasma generating section (24) comprises a dielectric tube (23) extending into the dielectric tubular mixing section (10) up to the opening (18) in the side wall (16b) of the dielectric tubular mixing section (10), and
   wherein the tubular plasma generating section (24) has an opening (20) in its side wall (16a) connected to dielectric tube (23), wherein the opening (20) is positioned above, in the direction of the central axis of tubular system (22), opening (18) in the side wall (16b) of the dielectric tubular mixing section (10);
   d) supplying an inert working gas (7) to dielectric tube (23) of the tubular plasma generating section (24) via opening (20) in the side wall (16a) and creating an atmospheric pressure plasma from this inert working gas (7) at the outer end of dielectric tube (23) extending into the dielectric tubular mixing section (10);
   e) supplying the aerosol (4) obtained in step (b) to the dielectric tubular mixing section (10) via dielectric inlet tube (14) and opening (18) in the side wall (16b);
   f) allowing interaction of the aerosol (4) and the plasma in the dielectric tubular mixing section (10) to generate metal oxide nanoparticles **characterized by** a particle size distribution with a Dv99 of less than 100 nm, preferably with a Dv90 below 10 nm; and
   g) deposition of said metal oxide nanoparticles through an orifice (21) in the bottom (11) of the dielectric tubular mixing section (10) onto a solid or semi-solid substrate (13).

2. Method according to claim 1, wherein the dielectric inlet tube (14) is positioned at an angle of inclination θ with the central axis of tubular system (22), such that the second end (19) connected to the nebuliser (3) is positioned above the first end connected to the opening (18) in the direction of the central axis of tubular system (22), wherein the angle of inclination θ is preferably between 50 and 89°, more preferably between 60 and 70°.

3. Method according to claim 1 or 2, wherein tubular system (22) comprises two adjacent zones (A) and (B) in a direction of the central axis of tubular system (22) from the top (17) to the bottom (11):

- zone (A) is part of the dielectric tubular mixing section (10), comprising the opening (18) for supplying the aerosol (4), wherein plasma is generated at the outer end of dielectric tube (23) extending into the dielectric tubular mixing section (10), and wherein the plasma interacts with the aerosol (4) resulting in high energy particles and ion bombardment; and
- zone (B) below zone (A) is an afterglow zone which is also part of the dielectric tubular mixing section (10) and which comprises the orifice (21) wherein both reactive and neutral particles are present and wherein particles may aggregate by recombination.

4. Method according to any one of claims 1 - 3, wherein steps (b) -(g), preferably steps (a) - (g), are performed as a continuous process.

5. Method according to any one of claims 1 - 4, wherein the metal oxides in the macropowder used in step (a) and in the nanoparticles obtained in step (g) are oxides of transition metals, preferably selected from the groups consisting of oxides of vanadium (V), niobium (Nb), ruthenium (Ru), manganese (Mn), cobalt (Co) and nickel (Ni), more preferably oxides of vanadium, very preferably vanadium pentoxide.

6. Method according to any one of claims 1 - 5, wherein the liquid used in the dispersion (15) of step (a) is water.

7. Method according to any one of claims 1 - 6, wherein the inert carrier gas (1) applied in step (b) is a noble gas, preferably argon.

8. Method according to any one of claims 1 - 7, wherein the flow of the inert carrier gas (1) applied in step (b) is more than 1000 sccm, preferably between 1000-3000 sccm, more preferably between 2000 and 2500 sccm, most preferably about 2300 sccm.

9. Method according to any one of claims 1 - 8, wherein the inert working gas (7) is a noble gas, preferably helium.

10. Method according to any one of claims 1-9, wherein in step (f) the inert working gas (7) represents from 6 vol% to 10 vol%, based on the carrier gas.

11. Method according to any one of claims 1 - 10, wherein the atmospheric pressure plasma is an atmospheric pressure plasma jet.

12. Method according to any one of claims 1 - 11, wherein the tubular plasma generating section (24) comprises a dielectric tubular cover (9) surrounding dielectric tube (23).

13. Method according to any one of claims 1 - 12, wherein the substrate (13) is placed at a distance between 1 and 15 mm, preferably between 4 and 10 mm, from the orifice (21) in the direction of the central axis of tubular system (22).

14. Method according to any one of claims 1 - 13, wherein the substrate (13) is a silicon wafer.

EP 3 960 703 A1

Fig. 1

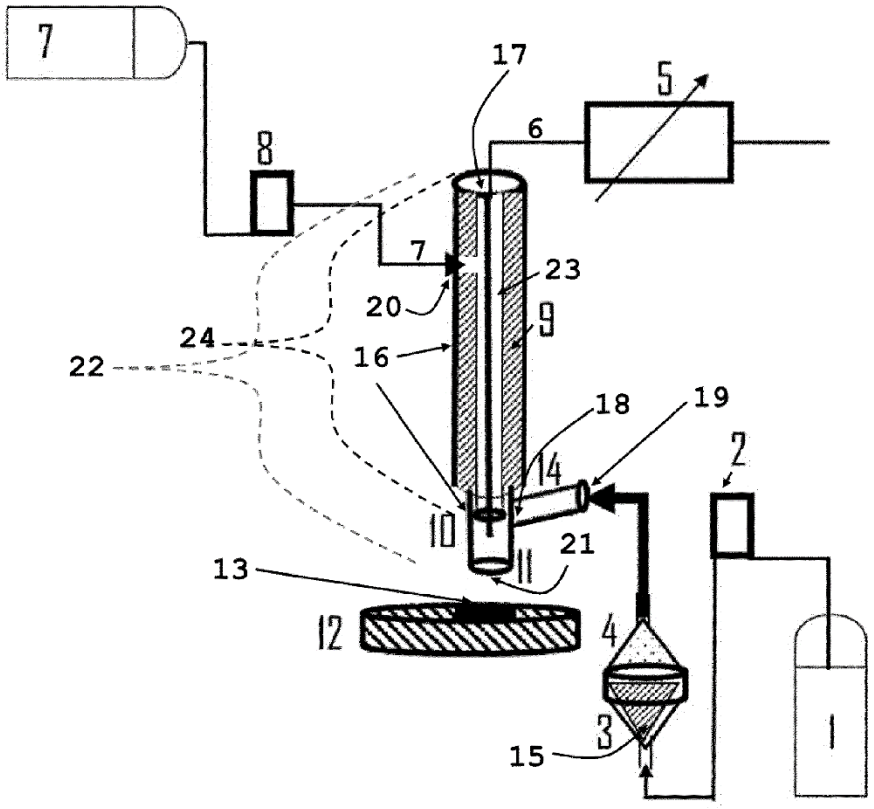

Fig. 2

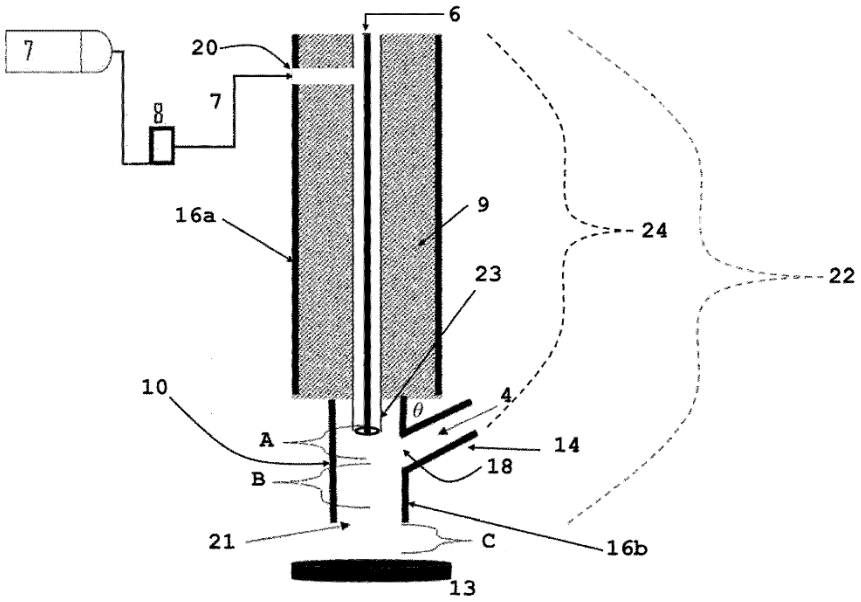

Fig. 3

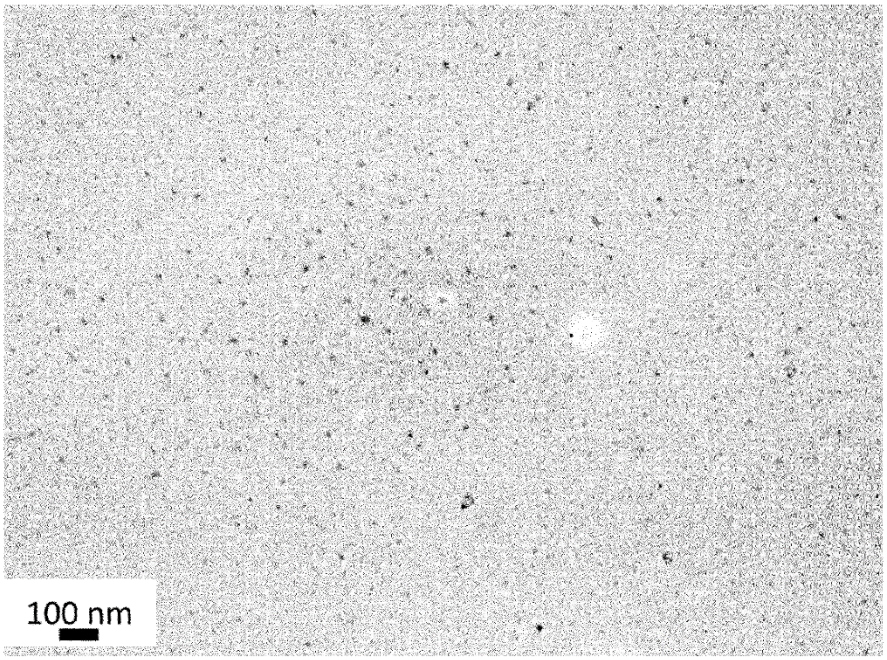

Fig. 4

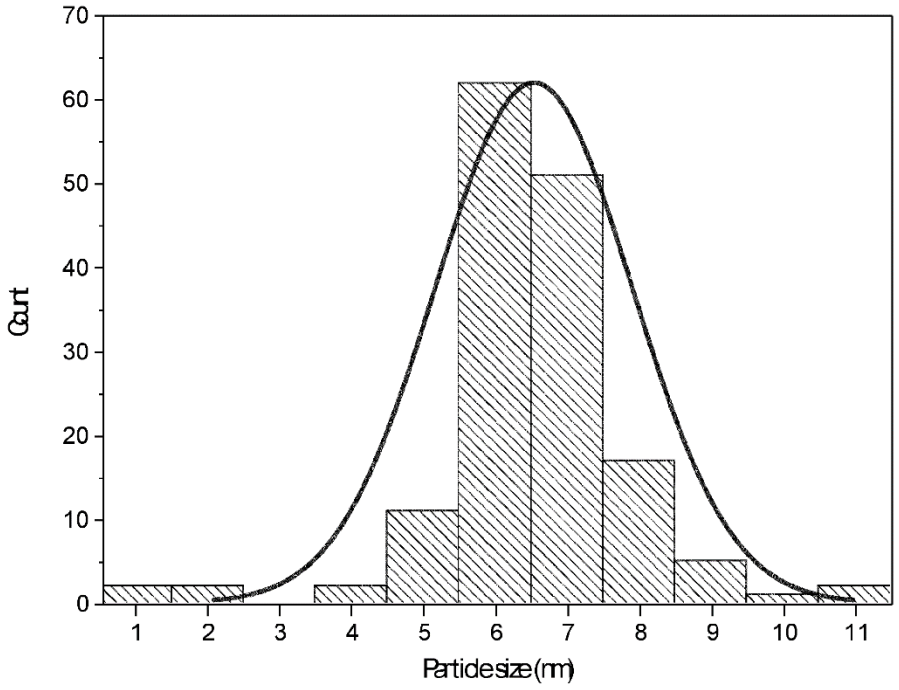

EP 3 960 703 A1

Europäisches Patentamt
European Patent Office
Office européen des brevets

EUROPEAN SEARCH REPORT

Application Number
EP 20 19 2874

DOCUMENTS CONSIDERED TO BE RELEVANT

Category	Citation of document with indication, where appropriate, of relevant passages	Relevant to claim	CLASSIFICATION OF THE APPLICATION (IPC)
A	EP 1 896 215 B1 (TOYOTA MOTOR CO LTD [JP]; STC UNM [US]) 15 July 2015 (2015-07-15) * claims 1,3-8,12,13 * * paragraphs [0006], [0012] * -----	1-14	INV. C01B13/14 B29C64/00 B82Y30/00 C01G31/02
A	SHIN D H ET AL: "Preparation of vanadium pentoxide powders by microwave plasma-torch at atmospheric pressure", MATERIALS CHEMISTRY AND PHYSICS, ELSEVIER SA, SWITZERLAND, TAIWAN, REPUBLIC OF CHINA, vol. 99, no. 2-3, 10 October 2006 (2006-10-10), pages 269-275, XP024994773, ISSN: 0254-0584, DOI: 10.1016/J.MATCHEMPHYS.2005.10.026 [retrieved on 2006-10-10] * experimental section (2) * * figure 1 * -----	1-14	H05H1/00
A	EP 2 093 305 A1 (UNIV BRUXELLES [BE]) 26 August 2009 (2009-08-26) * claims 1-16 * -----	1-14	TECHNICAL FIELDS SEARCHED (IPC) C01B H05H B29C B82Y C01G

The present search report has been drawn up for all claims

Place of search	Date of completion of the search	Examiner
The Hague	18 January 2021	Gerwann, Jochen

CATEGORY OF CITED DOCUMENTS

X : particularly relevant if taken alone
Y : particularly relevant if combined with another document of the same category
A : technological background
O : non-written disclosure
P : intermediate document

T : theory or principle underlying the invention
E : earlier patent document, but published on, or after the filing date
D : document cited in the application
L : document cited for other reasons

& : member of the same patent family, corresponding document

EPO FORM 1503 03.82 (P04C01)

ANNEX TO THE EUROPEAN SEARCH REPORT ON EUROPEAN PATENT APPLICATION NO. EP 20 19 2874

This annex lists the patent family members relating to the patent documents cited in the above-mentioned European search report. The members are as contained in the European Patent Office EDP file on
The European Patent Office is in no way liable for these particulars which are merely given for the purpose of information.

18-01-2021

Patent document cited in search report	Publication date	Patent family member(s)	Publication date
EP 1896215 B1	15-07-2015	CN 101426610 A	06-05-2009
		CN 104973577 A	14-10-2015
		EP 1896215 A2	12-03-2008
		JP 5620059 B2	05-11-2014
		JP 2009509897 A	12-03-2009
		US 2007075052 A1	05-04-2007
		WO 2006133347 A2	14-12-2006
EP 2093305 A1	26-08-2009	NONE	

REFERENCES CITED IN THE DESCRIPTION

This list of references cited by the applicant is for the reader's convenience only. It does not form part of the European patent document. Even though great care has been taken in compiling the references, errors or omissions cannot be excluded and the EPO disclaims all liability in this regard.

Patent documents cited in the description

- US 20170298516 A1 **[0004]**
- US 20170259501 A1 **[0004]**
- US 8282906 B2 **[0005]**
- US 8029595 B2 **[0006]**
- US 7169375 B2 **[0007]**
- US 20150162596 A1 **[0008]**
- US 2015162583 A1 **[0008]**
- US 8318128 B **[0009]**
- US 5935293 A **[0010] [0011] [0013]**
- US 5749937 A **[0010] [0011]**
- US 5788738 A **[0010] [0012]**
- US 5851507 A **[0010] [0012]**

Non-patent literature cited in the description

- **NG, S. H. ; PATEY, T. J. ; BÜCHEL, R. ; KRUMEICH, F. ; WANG, J. Z. ; LIU, H. K. ; PRATSINIS, S.E. ; NOVAK, P.** Flame Spray-Pyrolyzed Vanadium Oxide Nanoparticles for Lithium Battery Cathodes. *Phys. Chem. Chem. Phys.*, 2009, vol. 11, 3748-3755 **[0063]**
- **CUI, H. N. ; TEIXEIRA, V. ; MENG, L. J. ; WANG, R. ; GAO, J. Y. ; FORTUNATO, E.** Thermochromic Properties of Vanadium Oxide Films Prepared by Dc Reactive Magnetron Sputtering. *Thin Solid Films*, 2008, vol. 516, 1484-1488 **[0063]**
- **CHEREMISIN, A. ; PUTROLAYNEN, V. ; VELICHKO, A. ; PERGAMENT, A. ; KULDIN, N. ; GRISHIN, A.** UV Laser Modification and Selective Ion-Beam Etching of Amorphous Vanadium Pentoxide Thin Films. *Phys. Status Solidi Appl. Mater. Sci.*, 2009, vol. 206, 1484-1487 **[0063]**

References

[1] A. Schütze, J. Y. Jeong, S. E. Babayan, J. Park, G. S. Selwyn, and R. F. Hicks, "The atmospheric-pressure plasma jet: A review and comparison to other plasma sources," *IEEE Trans. Plasma Sci.*, vol. 26, no. 6, pp. 1685–1694, 1998.

[2] D. Mariotti and R. M. Sankaran, "Microplasmas for nanomaterials synthesis," *Journal of Physics D: Applied Physics*. 2010.

[3] I. Levchenko *et al.*, "Plasma treatment for next-generation nanobiointerfaces," *Biointerphases*, vol. 10, no. 2, p. 029405, 2015.

[4] R. M. Sankaran and K. P. Giapis, "Maskless etching of silicon using patterned microdischarges," *Appl. Phys. Lett.*, vol. 79, no. 5, pp. 593–595, 2001.

[5] H. Yoshiki, "Localized etching of an insulator film coated on a copper wire using an atmospheric-pressure microplasma jet," *Rev. Sci. Instrum.*, vol. 78, no. 4, 2007.

[6] H. Yoshiki and Y. Horiike, "Localized plasma processing of materials using atmospheric pressure microplasma jets," *2002 Int. Microprocess. Nanotechnol. Conf. MNC 2002*, vol. 19, pp. 236–237, 2002.

[7] T. Ito and K. Terashima, "Thermoelectron-enhanced micrometer-scale plasma generation," *Appl. Phys. Lett.*, vol. 80, no. 15, pp. 2648–2650, 2002.

[8] K. H. Becker, K. H. Schoenbach, and J. G. Eden, "Microplasmas and applications," *J. Phys. D. Appl. Phys.*, vol. 39, no. 3, 2006.

[9] K. Tachibana, "Current status of microplasma research," *IEEJ Trans. Electr. Electron. Eng.*, vol. 1, no. 2, pp. 145–155, 2006.

[10] P. I. Butyagin, Y. V. Khokhryakov, and A. I. Mamaev, "Microplasma systems for creating coatings on aluminium alloys," *Mater. Lett.*, vol. 57, no. 11, pp. 1748–1751, 2003.

[11] V. Karanassios, "Microplasmas for chemical analysis: Analytical tools or research toys?," *Spectrochim. Acta - Part B At. Spectrosc.*, vol. 59, no. 7, pp. 909–928, 2004.

[12] L. A. Dykman and N. G. Khlebtsov, "Gold Nanoparticles in Biology and Medicine: Recent Advances and Prospects," *Acta Naturae*, 2011.

[13] E. C. Dreaden, L. A. Austin, M. A. MacKey, and M. A. El-Sayed, "Size matters: Gold nanoparticles in targeted cancer drug delivery," *Therapeutic Delivery*. 2012.

[14] M. R. Bindhu and M. Umadevi, "Silver and gold nanoparticles for sensor and antibacterial applications," *Spectrochim. Acta - Part A Mol. Biomol. Spectrosc.*, 2014.

[15] H. Furusho, K. Kitano, S. Hamaguchi, and Y. Nagasaki, "Preparation of Stable Water-Dispersible PEGylated Gold Nanoparticles Assisted by Nonequilibrium

Atmospheric-Pressure Plasma Jets," *Chem. Mater.*, 2009.

[16] X. L. Hu, O. Takai, and N. Saito, "Synthesis of gold nanoparticles by solution plasma sputtering in various solvents," in *Journal of Physics: Conference Series*, 2013.

[17] H. Conrads and M. Schmidt, "Plasma generation and plasma sources," *Plasma Sources Sci. Technol.*, 2000.

[18] K. Ostrikov, "Reactive plasmas as a versatile nanofabrication tool," *Rev. Mod. Phys.*, 2005.

[19] A. Von Keudell and V. Schulz-Von Der Gathen, "Foundations of low-temperature plasma physics - An introduction," *Plasma Sources Science and Technology*. 2017.

[20] M. G. Kong, M. Keidar, and K. Ostrikov, "Plasmas meet nanoparticles-where synergies can advance the frontier of medicine," *J. Phys. D. Appl. Phys.*, 2011.

[21] X. Lu, M. Laroussi, and V. Puech, "On atmospheric-pressure non-equilibrium plasma jets and plasma bullets," *Plasma Sources Sci. Technol.*, 2012.

[22] B. Ghimire *et al.*, "An atmospheric pressure plasma jet operated by injecting natural air," *Appl. Phys. Lett.*, 2018.

[23] J. Winter, R. Brandenburg, and K. D. Weltmann, "Atmospheric pressure plasma jets: An overview of devices and new directions," *Plasma Sources Sci. Technol.*, 2015.

[24] A. Schütze, J. Y. Jeong, S. E. Babayan, J. Park, G. S. Selwyn, and R. F. Hicks, "The atmospheric-pressure plasma jet: A review and comparison to other plasma sources," *IEEE Trans. Plasma Sci.*, 1998.

[25] C. Tendero, C. Tixier, P. Tristant, J. Desmaison, and P. Leprince, "Atmospheric pressure plasmas: A review," *Spectrochimica Acta - Part B Atomic Spectroscopy*. 2006.

[26] P. Lukes, E. Dolezalova, I. Sisrova, and M. Clupek, "Aqueous-phase chemistry and bactericidal effects from an air discharge plasma in contact with water: Evidence for the formation of peroxynitrite through a pseudo-second-order post-discharge reaction of H2O 2 and HNO2," *Plasma Sources Sci. Technol.*, 2014.

[27] T. Takamatsu *et al.*, "Investigation of reactive species using various gas plasmas," *RSC Adv.*, 2014.

[28] I. G. Koo, M. S. Lee, J. H. Shim, J. H. Ahn, and W. M. Lee, "Platinum nanoparticles prepared by a plasma-chemical reduction method," *J. Mater. Chem.*, 2005.

[29] Y. Zhou, S. H. Yu, X. P. Cui, G. Y. Wang, and Z. Y. Chen, "Formation of silver nanowires by a novel solid-liquid phase arc discharge method," *Chem. Mater.*, 1999.

[30] C. Richmonds and R. M. Sankaran, "Plasma-liquid electrochemistry: Rapid synthesis of colloidal metal nanoparticles by microplasma reduction of aqueous cations," *Appl. Phys. Lett.*, 2008.

[31] W. H. Chiang, C. Richmonds, and R. M. Sankaran, "Continuous-flow, atmospheric-pressure microplasmas: A versatile source for metal nanoparticle synthesis in the gas or liquid phase," *Plasma Sources Sci. Technol.*, 2010.

[32] K. McNamara and S. A. M. Tofail, "Nanoparticles in biomedical applications,"

Advances in Physics: X. 2017.

[33] S. M. Dizaj, F. Lotfipour, M. Barzegar-Jalali, M. H. Zarrintan, and K. Adibkia, "Antimicrobial activity of the metals and metal oxide nanoparticles," *Materials Science and Engineering C*. 2014.

[34] B. Eliasson and U. Kogelschatz, "Nonequilibrium Volume Plasma Chemical Processing," *IEEE Trans. Plasma Sci.*, vol. 19, no. 6, pp. 1063–1077, 1991.

[35] B. Eliasson and U. Kogelschatz, "Modeling and Applications of Silent Discharge Plasmas," *IEEE Trans. Plasma Sci.*, vol. 19, no. 2, pp. 309–323, 1991.

[36] J. Salge, "Plasma-assisted deposition at atmospheric pressure," *Surf. Coatings Technol.*, vol. 80, no. 1–2, pp. 1–7, 1996.

[37] "Plasma Processes Polymers - 2020 - Milaniak - Atmospheric-pressure plasma-enhanced chemical vapor deposition of.pdf." .

[38] R. Severens, J. Bastiaanssen, and D. Schram, "High-quality a-Si:H grown at high rate using an expanding thermal plasma," *Surf. Coatings Technol.*, vol. 97, no. 1, pp. 719–722, 1997.

[39] X. Zhang, Y. Guo, and G. Han, "Fabrication of titanium dioxide thin films by DBD-CVD under atmosphere," *Plasma Sci. Technol.*, vol. 9, no. 6, pp. 674–677, 2007.

[40] A. Sarani, A. Y. Nikiforov, N. De Geyter, R. Morent, and C. Leys, "Surface modification of polypropylene with an atmospheric pressure plasma jet sustained in argon and an argon/water vapour mixture," *Appl. Surf. Sci.*, vol. 257, no. 20, pp. 8737–8741, 2011.

[41] S. Bornholdt, M. Wolter, and H. Kersten, "Characterization of an atmospheric pressure plasma jet for surface modification and thin film deposition," *Eur. Phys. J. D*, vol. 60, no. 3, pp. 653–660, 2010.

[42] W. H. Chiang, D. Mariotti, R. M. Sankaran, J. G. Eden, and K. Ostrikov, "Microplasmas for Advanced Materials and Devices," *Adv. Mater.*, vol. 32, no. 18, 2020.

[43] A. Stancampiano *et al.*, "Plasma and aerosols: Challenges, opportunities and perspectives," *Appl. Sci.*, vol. 9, no. 18, 2019.

[44] M. M. Benarie, "Aerosol measurement," *Sci. Total Environ.*, vol. 19, no. 2, pp. 199–202, 1981

Bibliography

Publications Related to the Thesis

Journal Articles

1. Aswathy Vasudevan, Vasyl Shvalya, Aleksander Zidanšek, Uroš Cvelbar. Tailoring electrical conductivity of two dimensional nanomaterials using plasma for edge electronics: A mini review. Frontiers of Chemical Science and Engineering, 2019

2. Aswathy Vasudevan, Vasyl Shvalya, Martin Kosicek, Janez Zavasnik, Andrea Jurov, Neelakandan M Santosh, Aleksander Zidanšek, Uroš Cvelbar. From Faceted Nanoparticles to Nanoporous Film by Plasma-Jet Redox Reaction of Ionic Gold. Journal of Alloys and Compounds (*article submitted*)

3. Vasyl Shvalya, Aswathy Vasudevan, Martina Modic, Mohammad Abutoama, Cene Skubic, Nejc Nadižar, Janez Zavašnik, Damjan Vengust, Aleksander Zidanšek, Ibrahim Abdulhalim, Damjana Rozman and Uroš Cvelbar. Bacterial DNA Recognition by SERS Active Plasma-Coupled Nanogold. NanoLetters (*article resubmitted*)

European Patent

Vasudevan, Aswathy, Filipič, Gregor, Zavašnik, Janez, Cvelbar, Uroš.
Method for in situ synthesis and deposition of metal oxide nanoparticles with atmospheric pressure plasma: patent application EP20192874.4. München: European Patent Office, 26. Aug. 2020.

Other Publications (optional)

1. Ana Oberlintner, Vasyl Shvalya, Aswathy Vasudevan, Damjan Vengust, Blaž Likozar, Uroš Cvelbar, Uroš Novak, Hydrophilic to hydrophobic: Ultrafast conversion of cellulose nanofibrils by cold plasma fluorination, 2021.

2. Neelakandan M. Santhosh, Aswathy Vasudevan, Andrea Jurov, Anja Korent, Petr Slobodian, Janez Zavašnik, Uroš Cvelbar, Improving sensing properties of entangled

carbon nanotube based gas sensors by atmospheric plasma surface treatment, Microelectronic Engineering 2020.

3. Santhosh, N.M.; Vasudevan, A. A.; Jurov, A.; Filipič, G.; Zavašnik, J.; Cvelbar, U.Oriented Carbon Nanostructures from Plasma Reformed Res orcinol Formaldehyde Polymer Gels for Gas Sensor Applications. Nanomaterials 2020.

4. Yadu Nath VK, Raghvendrakumar M, Aswathy V, Parvathy P, Sunija S, Neelakandan MS, Nitheesha Shaji and Vishnu KA. Chitosan as Promising Materials for Biomedical Application: Review, Research & Development in Material Science , Crimson publishers, 2017

Conferences Contributions

1. Spring meeting, European Materials Research Society (E-MRS), June 18 to 22, 2018, Strasbourg, France (Oral)
2. 54th International Conference on Microelectronics, Devices and Materials (MIDEM), 3-5 October 2018, Ljubljana, Slovenia (Oral)
3. International Workshop on Plasma-Tailored Nanostructures and Applications (WOPTAN), 14-17 January 2019, Rogla, Slovenia (Oral)
4. Gordon Research Conference (GRC) and PhD School, 16-21 June 2019, Hong Kong, China (Poster)

Published Conference Abstracts:

1. Single step synthesis and deposition of gold nanoparticles using atmospheric pressure plasma jets (ECS Meeting Abstracts, Volume MA2021-02, D06: Atmospheric Pressure Plasma Processing)
2. Metal oxide anchored graphene-gold nanoparticles hybrid electrodes for energy applications (E-MRS, Spring meeting 2018, Carbon- and/or nitrogen-containing thin films and nanomaterials)

Biography

The author of this dissertation completed her Bachelor's degree in Industrial Chemistry from Mahatma Gandhi University and her Master's degree in Nanoscience and Nanotechnology from the International and Inter University Centre for Nanoscience and Nanotechnology (IIUCNN), Mahatma Gandhi University, Kerala, India. She accomplished her Master's studies with a thesis entitled "Solid state NMR studies in Natural rubber-Nitrile Rubber blend Nanocomposites" under the supervision of Dr. Ulrich Scheler (Head of Department Polyelectrolytes and Dispersions, Leibniz-Institut für Polymerforschung, Dresden, Germany). In 2017, she started her doctoral studies at Jožef Stefan International Postgraduate School (IPS) at the department of Gaseous Electronics, Jožef Stefan Institute, Ljubljana, Slovenia. During her doctoral studies, she focused on the synthesis and modification of nanomaterials using atmospheric pressure plasma jets, with a special focus on noble metal nanoparticle synthesis. During her doctoral studies, she collaborated with many other works involving nanomaterials and low-pressure plasmas. She contributed to a number of international conferences held in Slovenia and abroad.